MASTER THESIS WITHIN BIOMEDICAL ENGINEERING,
Msc Progr - MPBME,
30.0 Credits

Development of a Triboelectrically Powered Intracranial Pressure Sensor and a Brain Phantom Test Rig

Master's thesis conducted at the
Department of Microtechnology and Nanoscience
August 9, 2023

Shabir Afshar

Department of Microtechnology and Nanoscience, MC2
CHALMERS UNIVERSITY OF TECHNOLOGY
Gothenburg, Sweden 2023

Author

S. Afshar (ashabir@student.chalmers.se)

Supervisor:	Maria Asplund, (maria.asplund@chalmers.se) Professor at the Department of Microtechnology and Nanoscience, Electronics Materials and Systems Laboratory.
Examiner:	Per Lundgren, (per.lundgren@chalmers.se) Professor at the Department of Microtechnology and Nanoscience, Electronics Materials and Systems Laboratory.

Master thesis MCCX04
Department of Microtechnology and Nanoscience, MC2
Chalmers University of Technology
SE-412 96 Gotheburg

"We've always defined ourselves by the ability to overcome the impossible. And we count these moments. These moments when we dare to aim higher, to break barriers, to reach for the stars, to make the unknown known. We count these moments as our proudest achievements."

- J. Cooper, *Interstellar*

Abstract

Intracranial pressure (ICP) monitoring is crucial for diagnosing and treating neurological disorders. This master thesis focuses on developing a self-powered pressure sensor for wireless pressure monitoring inside the skull. The sensor design is based on triboelectric technology, aiming to overcome the limitations of conventional ICP sensors such as power supply requirements, complex fabrication, and mechanical inflexibility.

The primary goal of this study is to explore the potential of triboelectric pressure sensors for monitoring ICP. A test rig and brain phantom are also constructed to simulate pressure variations of the actual brain *in vitro*.

Triboelectric sensors convert mechanical pressure into electrical signals through electrostatic induction. First, the literature is reviewed on ICP and conventional invasive pressure sensors. Then, simulations of the modelled sensor are conducted by COMSOL software. Achieved results provide valuable insights into the implementation and feasibility of triboelectric pressure sensors for ICP monitoring. Additionally, the project successfully achieved the construction of a simplified brain phantom with a pressure-tight ventricle void. This was accomplished by casting silicone rubber into a 3D-printed mould, serving as the project's secondary goal.

In conclusion, this thesis presents extensive research on developing and evaluating triboelectric sensing mechanisms for ICP monitoring. The findings contribute to the advancement of less invasive pressure sensors, holding potential significance in neurology and healthcare.

Keywords: Intracranial pressure, self-powered sensors, bio-compatible implantable sensors, triboelectrification, Brian phantom.

Acknowledgement

The author would like to convey his sincere gratitude and appreciation to all those who have contributed to the successful completion of this research.

I am extremely grateful to my supervisor Prof. Maria Asplund for her support, advice and invaluable insights throughout this voyage. Her expertise, insightful feedback, constructive criticism and encouragement have been influential in the shaping and quality of this thesis.

Furthermore, I would like to express my modest appreciation to the faculty members Prof. Per Lundgren, Neurosurgeon Dan Farahmand and PhD researcher Lukas Matter for their assistance, guidance in the lab and its instruments, valuable feedback and cooperation during the process of this thesis, which significantly enriched the quality of this work.

I would also acknowledge the assistance and support received from my colleague MSc. Charlie Erndin Dahlberg and Andrii Grytsan at the COMSOL support, who are willing to volunteer their time. Their aid has been invaluable in carrying out the simulation's results.

Last but not least, I want to express my heartfelt appreciation to my brothers and my girlfriend for their unwavering love, encouragement and understanding. Their constant support and belief in my abilities have been the cornerstone of this journey.

I am unable to name every individual who has contributed to this research, please accept my sincere appreciation. Your contributions have played a remarkable role in the success of this project.

Shabir Afshar, Gothenburg, May 2023

Contents

Acronyms

ADC analogue-digital-converter 7, 9

Ag silver 20

Al aluminium 20, 26, 29, 31, 33, 47–49, 53, 54, 56–59, 66, 67, 98, 99

Au gold 28, 29, 31–33, 46, 47, 50–58, 66–68, 98, 99

$BaTiO_3$ barium-titanate 17, 18

CNT carbon nanotube 14

CPP cerebral perfusion pressure 2

CS contact-separation 21–23, 97

CSF cerebrospinal fluid 1–3, 5, 9

Cu copper 20

EVA ethylene-vinyl acetate 29, 31, 33

ICC intracranial compliance 3–5, 97

ICP intracranial pressure iii, 1–6, 8, 9, 12–18, 20, 26, 28, 30, 33, 34, 41, 43–45, 48, 50, 53, 59, 65–67, 70–72, 97

IPS incline pressure sensor 35, 63, 64, 98, 99

MAP mean arterial pressure 2

PDMS polydimethylsiloxane 20, 27–29, 31–33, 44, 46–51, 53, 54, 56–59, 66, 67, 98, 99

PE polyethylene 20

PTFE polytetrafluoroethylene 20, 26, 61, 66

PVDF poly vinylidene fluoride 17–19

PZT lead zirconate titanate 17, 19

RF radio frequencies 7

TENG triboelectric nano-generator 14, 19–28, 41, 42, 44, 45, 49, 54, 65–68, 70–72, 97

ZnO zinc oxide 17, 18

Glossary

bio-compatible The ability of a material to perform with an appropriate host response in a specific application. 1, 8, 16–18, 27, 65, 66

electronegativity A measure of an atom's ability to attract shared electrons to itself. 19, 21

haemorrhage Intracranial bleeding. 1

hydrocephalus A neurological disorder caused by an abnormal buildup of cerebrospinal fluid in the ventricles (cavities) deep within the brain. The excess leads to elevated intracranial pressure and damage to brain tissue. 1

in vitro "In glass". The study takes place in a test tube, petri dishes or in a lab. iii, 8, 26, 28

in vivo "In living". The study takes place in a living organism. 10, 12, 13, 17, 27, 41, 44, 72

intracranial compliance The ability of the brain to accommodate changes in volume or pressure without a significant increase in intracranial pressure. 5

parenchyma A functional tissue in animals and plants. 5

permittivity The ability of a material to be electrically polarised under the effect of an electric field, shows as ε. 16, 17, 22, 27, 53

1

Introduction

Elevation or depression of pressures in the body organs (*e.g.* eye, brain, heart, or bladder) have a strong correlation with health status, critical conditions, and diseases in the body [1]. Intracranial pressure (ICP) monitoring was introduced already sixty years ago, and since then it is an essential procedure in the surveillance and diagnostics of neurological conditions and neurosurgical patients [2, 3]. The conventional solution to reduce the ICP is to drain out the cerebrospinal fluid (CSF) from the brain's ventricles via a catheter: so-called external ventricular drainage. The catheter is inserted inside the brain ventricles through a drilled hole in the skull bone to perform monitoring and drainage [4].

However, high costs associated with surgeries, invasiveness, infection hazard, and haemorrhage risks are primary challenges for monitoring ICP [2]. Additionally, surveillance of ICP on a daily basis for patients with neuropathological abnormalities requires expertise and complicated techniques [3]. These challenges prevent many patients from receiving necessary healthcare procedures.

Less invasive or non-invasive monitoring procedures present additional shortcomings in their measurement and functionality [2, 3, 5]. For instance, insufficient accuracy, longer response time, unreliability, impaired sensitivity, and insufficient robustness can be listed as measurement limitations. Meanwhile, the need for an external power source to operate, the sensor's bio-compatibility and the presence of signal drift in the long-term applications, classifies as their implantation obstacles [1, 6, 7]. Bio-compatibility of a material in an implant is defined as "the ability of a material to perform with an appropriate host response in a specific application." [8]. In simpler words, bio-compatible materials do not cause any adverse tissue reactions in the body.

Elevated ICP can be caused by many different neurological conditions for instance traumatic brain injuries, stroke, intracranial infections, haemorrhage, hydrocephalus, and brain tumours [3]. An elevated ICP is a life-threatening condition for the patients which is why frequent ICP monitoring is an important procedure, in order to avoid severe and irreversible consequences [2]. The need for developing a robust sensing mechanism to monitor ICP for the long term with low power consumption, mechanical flexibility and made of bio-compatible material is important. Such a sensing mechanism will be an essential tool to improve neurocritical care [3].

This study is divided into two main sections. The first section focuses on the design and simulation of a self-powered pressure-sensing mechanism based on the triboelectric effect. In this design, key factors of a pressure sensor are taken into consideration, while maintaining requirements such as self-powering ability, bio-compatibility, and mechanical flexibility. More detailed information is provided in Section 2.4.

The second section involves the construction of a test rig, which includes the manufacturing of a simplified brain phantom with a ventricle void. Additionally, a pressure generator is used to simulate pressure pulsations within the ventricle of the brain phantom. The test rig aims to accurately replicate the essential mechanical properties of the brain and the fluid-filled space inside the ventricle. For more information and specific details, please refer to Section 3.2.

1.1 Mechanism behind the ICP

Cerebral perfusion pressure (CPP) is the difference between mean arterial pressure (MAP) and the ICP (*i.e.*, $CPP = MAP - ICP$) [9]. CPP is the net pressure gradient that determines the oxygen delivery to the brain tissues and MAP is the average arterial pressure of blood, pumped by the heart in one cardiac cycle [10]. For patients with intracranial pathology, maintaining and managing CPP is a crucial key factor to prevent oxygen deficiency in the brain [9]. Elevated ICP has a greater effect on CPP decrement, compared to MAP. As a result, increased ICP leads to a decrease in CPP, which causes severe brain damage [5, 9]. This is because if the ICP increases, the pressure from the MAP cannot maintain the CPP at its required level, *i.e.*, to pump a sufficient amount of blood into the brain tissues.

Inside the rigid skull, the CSF, blood, and brain matter interact to maintain a state of volume equilibrium [5]. This means that the circulatory dynamics of the CSF and cerebral blood drive the ICP. The volumetric equilibrium triggers an auto-regulatory mechanism [11], known as spatial compensation, which involves a compensatory shift between the volume of CSF and intravascular blood. When abnormal volumes such as tumours or haemorrhages occupy space inside the skull, this mechanism is activated to regulate the ICP. However, there is a limited range for this spatial compensation, typically between $60 - 140\,\mathrm{mL}$ [12]. Consequently, the primary cause of elevated ICP is the volumetric enlargement of incompressible tissues such as blood accumulation or brain tissue swelling due to brain inflammation, tumour, infection or any injury [5]. Since these volumes cannot be compensated with the auto-regulatory system (blood or CSF), thus the ICP increases.

The pressure range for a normal ICP is a subject of discussion as it can vary depending on factors such as age, medical condition, clinical background, and body position [11]. For example, while standing, the ICP level can reach up to $-10\,\mathrm{mmHg}$. However, an average stable ICP range typically falls between $5 - 15\,\mathrm{mmHg}$. Generally, an ICP $\geq 20\,\mathrm{mmHg}$ is considered abnormal for adults, while this threshold can be equal to or greater than $15 - 18\,\mathrm{mmHg}$ for children [2, 13]. Heightened ICP $> 25\,\mathrm{mmHg}$ needs immediate neurointensive care and can cause severe and inevitable damage to the brain which can lead to the death of the patient [14].

It is worth mentioning that ICP variations over the mentioned threshold are normal if the body is under stressful physical activities *e.g.* running, rising or any sort of aerobic training [15]. However, it is important that the pressure regulates itself to the normal range and the ICP goes back to its normal status within the time interval. This time window has been reported different in a range between 10 minutes - a couple of hours, and it varies depending on the individual health status, age and symptoms intensity [11, 15].

Intracranial compliance (ICC) is a measure of the brain's ability to accommodate changes in the amount of CSF, blood, or other intracranial components without significant growth in ICP [16]. ICC is inversely proportional to the ICP. ICC can be defined as the ratio between the change in volume ΔV and the change in pressure ΔP inside the skull, expressed as $ICC = \Delta V/\Delta P$ [17]. In particular, an increase in ICP corresponds to a decrease in ICC.

The relationship between the spatial compensation, ICP and additional volume are defined by the curve in Figure 1.1. The flattened segment of the curve, **A**, symbolises a good ICC or higher compliance. This means that the changes in volume do not contribute to a dramatic change in ICP. Section **B** of the curve indicates that the ICC starts to decrease and the spatial compensation reserve is gradually depleted. The exponential section of the curve **C**, illustrates that the compensatory reserve is exhausted and ICC is small. Consequently, ICP rises dramatically if the volume increases slightly. This is a critical situation since it can cause cerebral ischaemia (blood-flow restriction) or herniation of the brain-stem [17]. Section **D** in the curve represents the deranged cerebrovascular reactivity; cerebral arterioles dilate and may collapse. This indicates that the pulse pressure from the arterial to the intracranial compartment decreases.

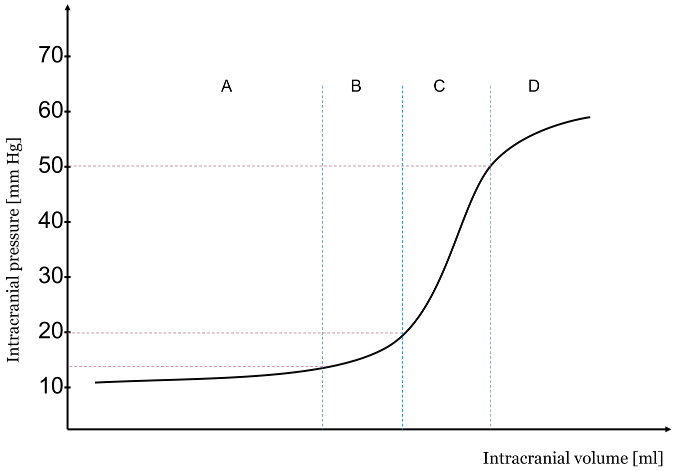

Figure 1.1: *Intracranial volume-pressure curve. A: Good compensatory reserve (High compliance), B: Compensatory reserve gradually depleted (Decreasing compliance), C: Exhausted compensatory reserve (Minimal compliance) and D: Collapse of the cerebral microvasculature. Regenerated from [5, 11, 18].*

Pressure variation inside the skull is illustrated as a blue curve in Figure 1.2. The curve is defined by its characteristic peaks and has a pulsating waveform which is influenced by the cardiac cycle [3, 16]. That is why an individual's pulsation affects their ICP waveform. Usually distinct peaks (*i.e.*, P_1, P_2 & P_3) are used as a basic verification of an ICP signal, where each peak defines as (P_1) percussion wave, (P_2) tidal wave and (P_3) dicrotic wave [16]. Despite several years of research in investigating the waveform of ICP, the origin of these peak components is still unclear. However, it is generally accepted that the relation between P_1 and

P_2 describes ICC. When P_1 exceed P_2 and in turn P_2 exceed P_3 this indicates a good intracranial compliance, as illustrated in Figure 1.2a. Meanwhile, the same relationship between P_1 and P_2 is not detectable when there is insufficient intracranial compliance (elevated ICP) according to Figure 1.2b.

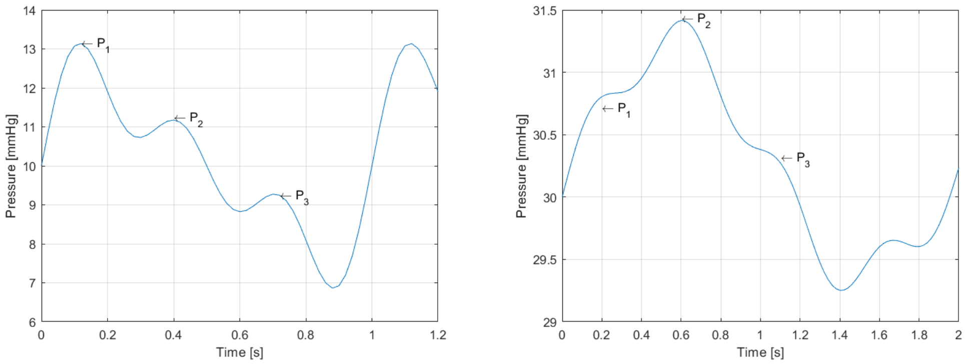

(a) *Normal ICP waveform with good compliance.*

(b) *Elevated ICP waveform with decreased compilance.*

Figure 1.2: *ICP waveforms with their characteristic peaks: P_1, P_2 & P_3 that behave different with different ICC. Regenerated from [3, 16].*

1.2 State-of-the-Art of ICP Measurement

Today, healthcare technology offers two possible strategies for performing ICP measurements: wired-based and wireless [11]. Transducers can measure ICP from three different segments of the intracranial space. Their method of measuring depends on the location of the sensor's tip [2, 11]. These methods are illustrated in Figure 1.3. The most common and accurate method of measuring ICP is performed through the CSF ventricular catheter [11]. The sensor's tip penetrates inside the cerebral ventricles (**V**) and this is the only method that enables external ventricular drainage to reduce ICP in critical situations [4, 14]. The second method to measure the ICP implements by implanting the sensors in the brain tissue *parenchyma* (**P**). These two methods can be classified as invasive implants [5]. In the third method, the sensor's tip is positioned on the epidural layer of the brain (**E**) which is a less invasive procedure [5].

Wireless transducers measure the ICP by the same three methods with the only difference that the transducers are implanted inside the skull and transmit the measurements through the head skin ”wirelessly” [7, 11].

To retrieve the data, a coil receiver must be positioned in proximity to the sensor's transmitter, which is located on the surface of the skull bone but underneath the head skin. The purpose of the receiver is to transmit or collect the measurements effectively.

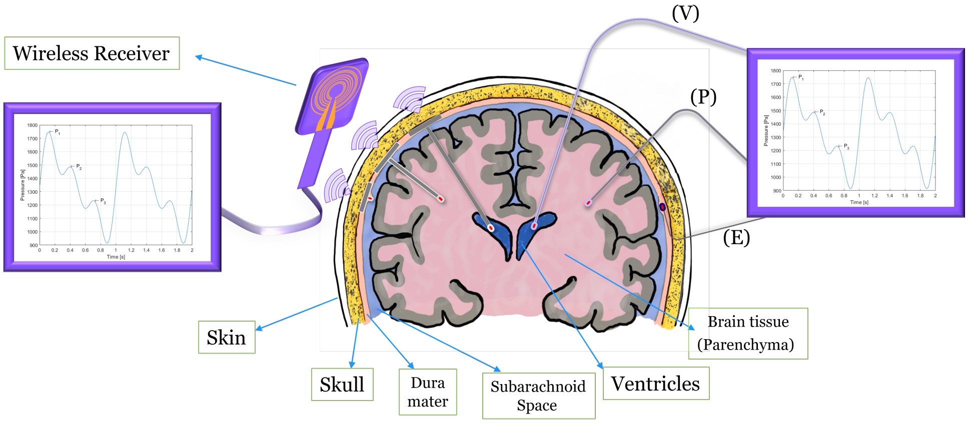

Figure 1.3: *The image depicts wireless and wire-based methods for measuring ICP. On the left side, three types of implantable ICP sensors are shown with their wireless receivers. In contrast, the right side illustrates three versions of wired-based ICP measuring methods. The text boxes at the bottom of the figure describe generally the different elements inside the skull. Adapted from [2].*

1.3 Components of a Sensor Node

Generally, a sensor node consists of five major units and each unit has its own area of responsibility for one or several specific tasks [19], as shown in the schematic block diagram; Figure 1.4.

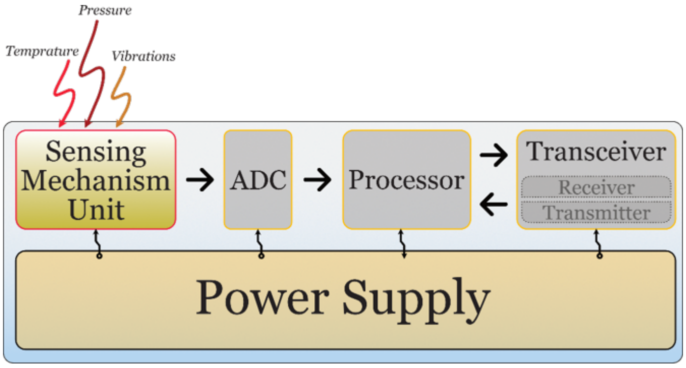

Figure 1.4: *Schematic diagram of a sensor node and its different units. Regenerated [19].*

The sensing mechanism unit detects variations in specific physical signals from its surrounding *e.g.* pressure, vibrations or thermal alterations [19, 20]. Additionally, the sensing unit is assigned to convert these analogue signals into an electrical voltage, current or frequency signal. This detection occurs either actively or passively [21]. An active sensing mechanism measures the signal variation in real time and provides an output signal as the variation occurs. In contrast, a passive sensing mechanism is usually independent of the external power source and it utilises passive components such as capacitors, inductors or diodes as a sensing mechanism. However, passive sensing mechanisms require outside stimuli such as radio frequencies (RF), external power supply or a light source within a specific frequency spectrum to actively perform measurements [7, 21].

The analogue-digital-converter (ADC) unit converts the analogue signal from the sensing mechanism into the digital (I/0) signal before it goes through the processing unit [22]. In some modern sensor nodes, the sensing mechanism unit and the ADC are often integrated together as an embedded unit, functioning as a single entity [19]. The processor unit is responsible for handling essential arithmetic operations, managing- communication, -power, -memory, and performing signal processing tasks like signal modulation or demodulation [19, 23]. The transceiver unit is composed of two functions: receiver and transmitter. It is a communication portal with external devices to transfer and receive signals [23]. Usually, transceivers are the most energy-consuming units in a sensor node [19]. Lastly, the power supply must provide the required energy for all other units in the sensor node to make them fully operational [19]. Relying on batteries or external power supplies as power sources can significantly restrict the lifetime and practicality of the sensor node as a long-term implant [13].

A micro-sized, sensitive, mechanically flexible, and accurate pressure sensing mechanism with minimum power consumption, or ideally even energy self-sufficiency, is described as the ultimate goal in neurocritical care for monitoring intracranial pressure (ICP) [2]. In general, mechanical flexible pressure sensors can be divided into four different technologies. *i.e.*, piezoresistive-, capacitive-, piezoelectric- and triboelectric-based pressure sensors [24]. Each one of these technologies has its strength and limitations. Further details about each mechanism will be provided in Section 2.

Innovative pressure sensors have been developed based on piezoresistive and capacitive sensing mechanisms [11, 25]. These sensors can fulfil the majority of requirements for the monitoring ICP [26, 27]. However, their practical application over a longer time scale is limited greatly due to their dependency on an external power supply. Pressure sensors developed based on the piezoelectric effect are promising to investigate since they have a self-powered capability [3, 11, 25]. Yet, the sensitivity, material's bio-compatibility and humidity intolerance of piezoelectric detectors are questionable aspects for an implantable ICP transducer.

The triboelectric-based pressure sensor is a promising candidate to investigate their for an ICP sensor [25]. Since these sensors can overcome the obstacles of self-power ability, long-term durability, bio-compatibility and mechanical flexibility [28].

1.4 Aim and Purpose

This project focused on exploring a micro-sensing mechanism for a wireless brain implant ICP sensor. The objective was to develop a sensing mechanism capable of detecting low-pressure magnitudes, providing mechanical flexibility, and being constructed from bio-compatible materials. Additionally, the sensor was intended to operate without relying on an external power supply, functioning as a self-powered pressure sensor. As such, the primary goal of this thesis is to assess the feasibility of a self-powered pressure sensor utilising the triboelectric effect for monitoring ICP. Furthermore, the suggested model is simulated using the COMSOL Multiphysics software. The simulation results will be evaluated to validate the viability of a triboelectric-based sensing mechanism for monitoring ICP.

The secondary aim of this study is to construct a test bench for simulating the ICP *in vitro*. The setup will include the manufacturing of a brain phantom and its ventricles. The phantom brain should be constructed using a material that closely mimics the mechanical properties of actual brain tissue. The design of the test rig should incorporate the essential features of the brain and ICP. For example, it should accurately model the dynamic pressure variations in the ventricles. Additionally, the phantom brain must replicate the mechanical elasticity of brain tissue and exhibit mechanical displacements in response to pulsating pressure pumps.

The latter aim of this thesis is a collaboration with another master thesis "Powering intracranial pressure sensor implants by harvesting energy from the human brain" done by Msc. student C. E. Dahlberg [29].

1.4.1 Technical requirements for an ICP sensor

The sensing mechanism should be able to detect a range of pressure intervals between −20 mmHg and 50 mmHg in reference to the atmosphere's pressure with a resolution of 1 mmHg [1, 13]. The size of the sensing mechanism should be small to fit on a small device since there is a narrow space in such a sensitive environment to implant a sensor [2]. A cylindrical shape with a maximum diameter of 10 mm and maximum height of 3 mm is acceptable according to the request from neurosurgeon D. Farahmand [13].

1.5 Scope and Limitations

This study is exclusively about the sensing mechanism unit of a pressure sensor node as a potential wireless ICP sensor brain implant. Other components such as the ADC, processor, transceiver and power supply unit are not included in the design process. Alternative pressure sensors based on piezoresistive, capacitive and piezoelectric effects have been briefly studied and evaluated to understand their advantages and disadvantages for this specific application. However, the focus is mainly on triboelectric-based pressure sensors and their potential for ICP monitoring. Thus, all the simulations and modelling are conducted only on the triboelectric-based pressure sensor. This study does not include the fabrication process for implementing the suggested sensing mechanism.

The phantom brain designed and constructed for the test bench setup will be a simplified version of a brain matter and its ventricular void, which will have cylindrical shapes. Additional physiological properties such as curvature, temperature and CSF properties of the brain have been neglected from the design, in order to reduce complexity. An *inline*-pressure sensor from *Fluigent* is used to analyse the performance of the test rig and assess the fundamental characteristics of the brain phantom. This includes investigating pressure variations before and after the ventricle of the phantom brain, the mechanical response of the brain phantom to normal and abnormal ICP intervals.

2

Background

This chapter offers a technical background on pressure sensors and provides an overview of the three general methods of pressure measurement (absolute, gauge and differential). It also discusses the key parameters of a pressure sensor and addresses the fundamental challenges faced by pressure-sensing mechanisms in *in vivo* applications. Additionally, the chapter explores the advantages and disadvantages of the four common pressure sensor technologies (piezoresistive, capacitive, piezoelectric and triboelectric)

2.1 Pressure Sensor

The sensing mechanism unit of a pressure sensor is assigned to convert the variation of outside pressure into an electrical signal (voltage, frequency or digital output signal) or any other readable signal (graphs or pressure amplitudes) [20, 30]. Pressure variations in a system can be measured using three different methods, each using a different baseline pressure as a reference point [1, 20, 31].

1. The absolute pressure measurement: In the absolute pressure measurement method, the baseline reference pressure or ”zero pressure” is defined as the vacuum.

2. The gauge pressure measurement: The device utilises atmospheric pressure as a baseline reference and provides the magnitude of the measured pressure relative to the atmospheric pressure.

3. The differential pressure measurements: In this method, pressure is measured at the two points of a system and the difference between them is calculated as a ”result pressure”. For instance, the differential pressure can be measured between the outside and inside of a urinary bladder [1].

Pressure sensors have gained significant attention in the research and development of biomedical applications [32, 33]. They are utilised for monitoring various pressures, including blood pressure, respiratory pressure, urinary bladder pressure, pressure inside the eyes, and surveillance of the pressure inside the skull [1]. The performance of a pressure sensor commonly is evaluated by the key parameters sensitivity, stability, linearity, the limit-of-detection, pressure range (measurement range), response time and environmental robustness [20, 34, 35].

The accuracy of a pressure sensor is determined by its sensitivity, stability, and linearity, which are key parameters to consider [30]. Accuracy refers to the difference between the actual applied pressure and the pressure magnitude recorded by the sensor [20].

In addition to the above mentioned key parameters, selectivity is a crucial requirement for pressure sensors [36]. The sensor must primarily measure the intended pressure while effectively rejecting any interference from unrelated factors that may introduce noise into the output signal. These factors can include vibrations, noise, temperature variations, or signals from other devices and even signals from the body [1]. To achieve selectivity various methods such as filtering, signal processing, encapsulation (shielding), and the use of specialised materials are employed to minimise cross-sensitivity to other variables [37].

- **The sensitivity** of a pressure sensor refers to the ability to detect small changes in pressure. It shows the ratio between the sensor's output signal and applied pressure. For instance, if the sensor's output signal would be voltage the sensitivity will be *i.e.*, $Senstivity = \frac{\Delta V}{\Delta mmHg}$. The higher the ratio the better the sensitivity [34].

- **The stability** of a pressure sensor defines the capability of the sensor to remain accurate over time.

- **Linearity** shows the correlation between the input pressure and output electrical signal. In the measurement range where a sensor is linear, it will provide a consistent change in its output signal for a given change in the applied pressure.

- **Limit-of-detection** is the minimum pressure that can be measured by the sensor with acceptable accuracy.

- **The measurement range** is defined as the detection capacity of a sensor.

i.e., the ability to detect a specific minimum and maximum pressure magnitude.

- **Response time** is the time delay that a sensor takes to detect the changes in pressure variations.
- **Environmental robustness** of a sensor relates to its tolerance for the harsh dynamics of its surrounding. *e.g.* tolerance to different temperatures, humidity and vibrations.

2.2 Challenges For Implantable Pressure Sensors

Key challenges faced by *in vivo* pressure sensors [1, 7, 11].

- The challenge of being dependent on an external power supply to operate.
- The challenge of calibrating the sensor implants for a long-term application and the drift in their measurements after a period of time.
- The integration of the sensor with the human body and its dynamic environment presents challenges, particularly in humid surroundings. The choice of material for the sensor becomes crucial in addressing these challenges, as it determines the sensor's compatibility and durability in harsh conditions. This requirement partially overlaps with the *Environmental Robustness* key parameter mentioned above.
- The challenge of being compact in size and mechanically flexible without compromising the essential key parameters mentioned in the previous section (Section 2.1).

2.2.1 Power Supply Dependency

Pressure sensors developed and applied for intracranial pressure (ICP) monitoring suffers from the need for a power supply unit [11]. However, using a battery or external power supply as a power source unit limits the lifetime of the sensor to implant inside the skull. A battery needs to be exchanged as its charge is exhausted which is not an ideal solution for ICP measuring in long-term implantation [11]. Likewise, an external power supply needs to be connected through a wire with the sensor which limits the mobility of the patient and ease of daily life.

Recently, there have been ongoing research efforts to develop piezoelectric and triboelectric energy harvesters to generate power from the body itself, aiming to reduce reliance on external power supplies [28, 38, 39].

2.2.2 Calibration and Drift

Calibration and drift are partially related to each other [1]. Calibration means ”zeroing” the sensor in order to avoid uncertainty or offset in the measurements. The majority of *in vivo* pressure sensors tend to measure based on the gauge method and their baseline is the atmosphere’s pressure [1]. To ensure accurate measurements, it is important to calibrate the sensor before implantation, as atmospheric pressure can vary based on factors such as time of day, location, and temperature.

Usually, there are two reasons that a drift arises in a pressure sensor: either changes in the environment where the sensor is implanted or changes in the sensor’s performance due to the material’s properties [1, 6]. *i.e.*, ageing or mechanic fatigue which is independent of the surrounding’s influences. The majority of studies show that signal drift over time is inevitable in pressure sensors since they age and this affects their sensitivity [1, 6, 14].

2.2.3 Choice of Material and Size of the Sensor

The choice of material used to construct the implantable pressure sensor is a crucial factor [1, 11]. The material should be capable to resist changes in its chemical composition over a period of time [40]. Ideally, the sensor surfaces that come into contact with body tissues should not chemically react with their surroundings. Minimising the probability of such risks is important to avoid immune reactions, tissue irritation, and potential leakage within the body. The material must be durable for long-term application and mechanically flexible to prevent damaging its surrounding tissues. Likewise, the pressure sensor designed for measuring ICP must be small in order to perform measurements inside the skull [7]. An oversized pressure sensor will press on the surrounding tissues which could lead to severe complications and a distorted ICP.

2.3 Sensing Mechanisms for Measuring ICP

This section will provide a brief description of the conventional three technologies used for monitoring ICP and Figure 2.1 illustrates a simple sketch of these three mechanisms.

Given that the main objective of this thesis is to investigate the potential of triboelectric-based pressure sensors for monitoring ICP, Section 2.3.4 will present a comprehensive theory of the triboelectric nano-generator (TENG) effect and its application as a pressure-sensing mechanism. It will cover the fundamental principles, and material selection, and provide both theoretical and technical knowledge in this area.

2.3.1 Piezoresistive Pressure Sensor

A piezoresistive sensor is based on the variation of the resistance in the device which is correlated to the applied pressure [24, 41]. A typical way to manufacture a piezoresistive sensor is to use a composite film (piezoresistive material) filled with conductive fillers (nano wire[41], carbon nanotube (CNT)s and graphene). Alternatively, using intrinsic conductive polymers, either as an electrode or sandwiched in between two conductive electrodes [42] (see Figure 2.1a).

The deformation of the composite film or the compression of the sandwich structure in response to applied pressure leads to a noticeable change in the resistance of the device [41, 42]. This resistance change is caused by variations in the contact path or contact points through nano-wires embedded in the material, resulting in the generation of a detectable signal. In Figure 2.1a, the red-colored nano-wires come into contact under the influence of an external force.

The structure depicted in Figure 2.1a illustrates that pressure compresses the distance between the electrodes, resulting in low resistance within the sensor due to the formation of contact paths in the nano-wires [24]. The current flowing from the external power supply through the sensing mechanism varies according to the changes in its resistance caused by external pressure. As a result, it produces a measurable change in the electrical signal that is directly correlated to the applied pressure [24, 41].

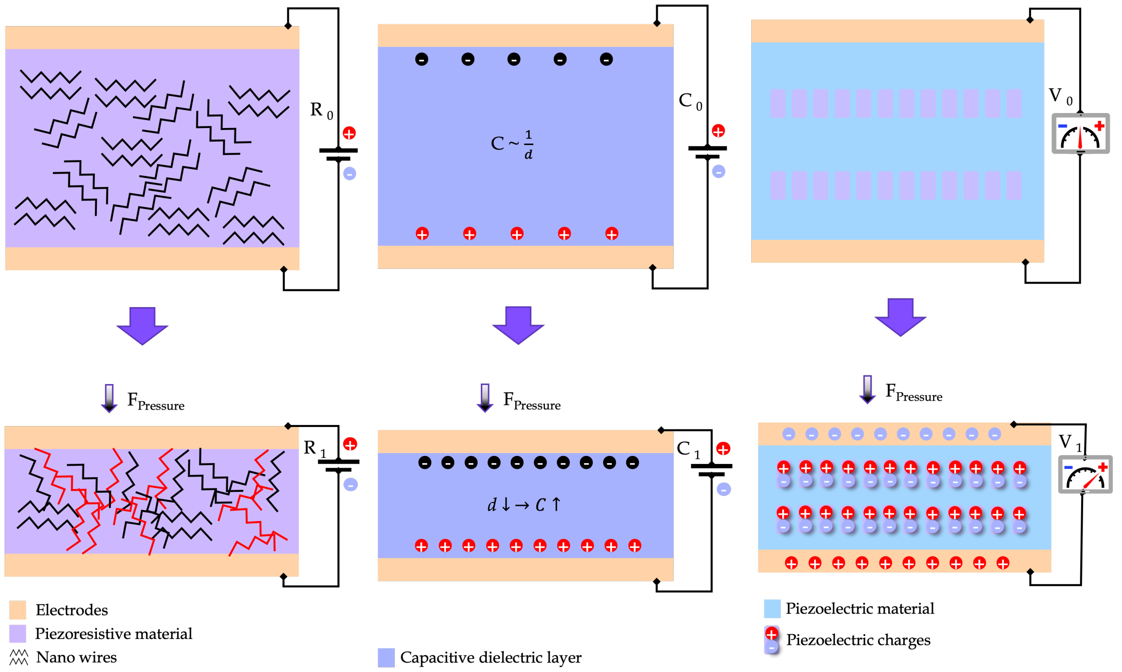

(a) *Piezoesistivity* (b) *Capacitance* (c) *Piezoelectricity*

Figure 2.1: *Mechanism behind the three conventional pressure sensors used for ICP measurements. Regenerated from [30, 32]*

2.3.1.1 Sensor's Key Parameters: Piezoresistive pressure sensors have shown a reasonable sensitivity for measuring ICP [34, 43, 44]. Furthermore, they have better linearity and shorter response time than capacitive pressure sensors. These sensors can measure a wide pressure range with a high resolution which is why they can detect small pressure variations. This attribute equips them with a low limit-of-detection ability [45]. In addition, they are more resistant to vibrations in comparison to piezoelectric sensors. Therefore, piezoresistive sensors provide more stable output signals in the short-term application (couple weeks) [7, 24, 42]. Piezoresistive sensors can withstand wet environments such as inside the body and that is why they are commonly used for monitoring ICP [11].

2.3.1.2 Required Capabilities: Piezoresistive pressure sensors have the advantage that they are easy to manufacture and calibrate [1, 11]. Manufactured pressure sensors conventionally used today are mechanically flexible and have a small size of $3-5\,\text{mm}$ which is preferable for measuring ICP. However, the need for an external power supply unit to operate limits their application as lifetime brain implants [11, 43]. Research has been invested into reducing their power consumption from several hundred micro-watts down to 62 µW but a trade-off has been made [46]. Either the manufactured material is not durable for a long-term application which *e.g.* silicon would be, or it is not bio-compatible for implantable sensor [47]. Moreover, these sensors suffer from inevitable drift for long-term applications [24].

2.3.2 Capacitive Sensor

Capacitive pressure sensors have the same mechanism as an electric capacitor. A layer of dielectric material has been sandwiched by two adjacent conductive electrode plates [26]. The device's capacitance is expressed by equation (1), where C represents the capacitance, ε is the dielectric material's permittivity, A represents the surface area of the conductive plates while d is the vertical distance between these two plates [7]. The applied pressure causes a variation in the distance d between the plates, resulting in changes in the capacitive value C. This variation in capacitance can be utilised to establish a correlation between the magnitude of pressure from the outside and the change in device's capacitance [7, 26] (refer to Figure 2.1b).

$$C = \frac{\varepsilon A}{d} \tag{1}$$

2.3.2.1 Sensor's Key Parameters: The capacitive sensing mechanisms are reliable for achieving some of the key parameters for an ICP sensor for instance sensitivity, stability and pressure range [7, 26, 34].

Typically, a large sensor area A improves the sensitivity and stability of a capacitive sensor [34]. However, the enlarged size goes against the optimum requirement for implantable ICP monitoring [1, 13]. A trade-off needs to be made between the size and its performance improvement.

Capacitive pressure sensors are widely known for their versatile sensing capabilities, allowing them to detect a broad range of pressure magnitudes, including low-pressure ranges ($0 - 145\,\text{kPa}$) and even negative pressures [48, 49]. Furthermore, capacitive sensors have the advantage of a low limit of detection. In contrast, capacitive sensors perform with poorer linearity and longer response time when subjected to dynamic pressures in comparison to piezoresistive ones which reduces their accuracy [34, 45]. In addition, their accuracy can be affected even by the temperature since permittivity ε can be influenced by thermal factors which is a weakness in their environmental robustness [1, 32].

2.3.2.2 Required Capabilities: Capacitive sensors exhibit lower power consumption compared to piezoresistive sensors. However, in order to enable real-time measurement, the presence of an external power supply is crucial for their operation [27, 47, 50]. Furthermore, capacitive pressure sensors are generally free from signal drift [34]. However, the accumulation of cells *in vivo* on the surface of the sensor after a period of time, can affect the sensor's sensitivity [1, 26].

Capacitive sensors made from elastic polymers have demonstrated excellent long-term durability. However, it should be noted that the sensitivity of such sensors decreases as the elasticity of the material increases [34]. Additionally, signals from capacitive pressure sensors are sensitive to a humid environment, *i.e.*, the dielectric constant varies due to the effect of moisture [34]. Although, studies have shown that by encapsulating the device with a bio-compatible material it is possible to overcome the latter obstacle which will be again a trade-off for its sensitivity [27].

2.3.3 Piezoelectric Sensor

In a piezoelectric material, the mechanical deformation in the material leads to a distortion of the material's internal dipole moment which generates an electrical voltage directly proportional to the applied pressure [51, 52] (see Figure 2.1c). These characteristics of the materials enable them to detect dynamic pressures and vibrations which can be converted into an electrical signal [32]. These sensors are mostly made of lead zirconate titanate (PZT),poly vinylidene fluoride (PVDF), Zinc oxide (ZnO), and Barium-titanate ($BaTiO_3$) (materials with piezoelectric ability) and can be manufactured very small in size [51–53].

2.3.3.1 Sensor's Key Parameters: Piezoelectric sensors have the majority of essential key parameters but in order to fulfil the requirements and overcome obstacles for measuring ICP some compromises need to be made. Piezoelectric-based pressure sensors are sensitive to dynamic pressure changes [54]. These sensors exhibit an ultra-fast response time as they generate real-time output signals *i.e.*, generally piezoelectric sensors do not need an external power supply to generate an electrical signal for the applied mechanical force [34]. The ultra-fast response time, allows them to have a lower limit-of-detection and better linearity than capacitive and piezoresistive sensors. Since the mechanical deformation of these sensors entails an electric output signal, piezoelectric sensors are not suitable for measuring static pressures [34, 45]. These sensors are sensitive to pressure vibrations as well, which are visible as noise in their output signal [25]. Thus, their sensitivity to detect low-pressure magnitudes can be unreliable, since a signal can be generated by the surrounding's vibration rather than an actual pressure change [55].

Piezoelectric pressure sensors have a compatible pressure range for monitoring ICP but they have a shorter pressure range in comparison to piezoresistive ones [11, 34]. Generally, inflexible piezoelectric crystals (*e.g.* ZnO or $BaTiO_3$) perform optimally and have stability in their output signals [53]. However, these crystals are soluble in humid environments which makes their environmental robustness vulnerable. Piezoelectric sensors made from a flexible material (*e.g.* PVDF) have poor durability, weak output signal and limited pressure range [34].

2.3.3.2 Required Capabilities: Piezoelectric sensing mechanisms are self-powered and have the lowest power consumption compared to capacitive and piezoresistive sensors [32, 34]. This attribute makes them independent from the external power supply but the scalability of the sensor's size has a direct correlation with the strength of its signal [47]. This is why piezoelectric sensors with smaller sizes generate weak and unreadable signals; such sensors need external circuitry to amplify their output signal [55, 56]. This is considered as a major weakness for implantable ICP sensors.

Piezoelectric pressure sensors are easy and inexpensive to fabricate but only from a limited selection of materials (piezoelectric materials) which typically are not bio-compatible [54, 55]. To retain essential capabilities (*i.e.*, sensitivity, stability and linearity) while fulfilling the requirements of (*i.e.*, mechanical flexibility, scalability and bio-compatibility) a trade-off needs to be made between these parameters [45]. Miniaturised and flexible pressure sensors based on the piezoelectric effect have been used for monitoring ICP [11]. However, in a clinical trial to evaluate the sensor, an average "off-set drift" $0-2\,\mathrm{mmHg}$ has been detected in its output signal after 60 days [56]. Generally, piezoelectric materials, such as PZT, are known for their durability [57]. However, piezoelectric materials with mechanical flexibility, such as PVDF, tend to experience a loss of sensitivity over time [45, 51, 54]. This sensitivity loss is attributed to the ageing of the material, which results in drift in the output signal.

2.3.4 Triboelectric Pressure Sensor

The triboelectric pressure sensor utilises a combination of the triboelectric- and electrostatic effects to measure pressure [58]. The triboelectric effect is the result of the electrostatic charges accumulated on the surface of a tribonegative dielectric material due to physical contact with another tribopositive material [59]. A material with larger electronegativity is categorised as a tribonegative material (acceptor) and in contrast, a tribopositive material or (donor) has lower electronegativity [60]. There must be a difference in the charge affinity between the two materials as tribo-pair in order to generate a triboelectric effect [59]. This is why the choice of materials for a tribo-pair is essential for the performance of triboelectric-based pressure sensors. Essential elements such as surface charge density, the size of the contact area between the triboelectric layers and the surface structure (surface energy/roughness) of the dielectric tribo-pair have a direct effect on the performance of the pressure sensor based on this technology [25, 61].

- Surface charge density: Refers to the number of electrical charges that can be accumulated on the surface area of the material [60, 62]. *i.e.*, the density of electrical charges per surface area. Surface charge density σ varies in each material and it depends on the material's electron affinity [60].
- Surface contact area: Is defined as the surface area of the two triboelectric materials which come into contact with each other [60]. As the pressure level is elevated the contact area between the layers increases as well [28]. In this study letter, A represents the contact surface area.
- The surface structure (surface roughness): Refers to the topography of the surface structure. For instance, micro pyramid shape structures or nano-scale roughness on the surface of the dielectric layer can enhance the output signal of the TENG-based pressure sensors [61, 63].

2.4 Background about Triboelectric Pressure Sensors

Briefly, when two tribo-materials that face each other, an external pressure compresses the tribo-pair and facilitates contact between the materials. This contact leads to the generation of the triboelectric effect, which is directly related to the applied pressure magnitude [60]. As the pressure increases, a larger surface area of the tribo-pair comes into contact, resulting in a greater accumulation of charge on their surfaces [25]. The conversion of mechanical pressure into an electrical signal demonstrates the self-powered nature of the triboelectric modality as a sensing mechanism. To date, there have been no studies conducted utilising TENG-based pressure sensors specifically for measuring ICP [11, 14]. However, TENG-based pressure sensors have been developed for e-skin and blood pressure measurements [25, 28, 64].

The abundance of materials found in nature allows for the generation of the triboelectric effect, resulting in a wide range of triboelectric materials suitable for various applications [58, 60]. These materials encompass diverse compositions of polymers (*e.g.* polytetrafluoroethylene (PTFE), polydimethylsiloxane (PDMS), polyethylene (PE). *etc.*) as well as numerous metallic elements (aluminium (Al), copper (Cu), silver (Ag). *etc.*). The selection of appropriate materials from the triboelectric series for the sensor design in this study will be extensively discussed in Section 2.4.3.

2.4.1 Physics and Mechanisms of the TENG

The fundamental physics behind the triboelectrification process at the quantum level and the relationship between the ”donor” and ”acceptor” of a tribo-pair can be described as follows: Originally two materials M_1 and M_2 with a distance in between d, have different occupied *Fermi* energy levels E_1 and E_2. Electrons of each material are trapped in the potential wells of the respective material (see Figure 2.2 i). As the distance d between materials decreases with pressure from the outside, and materials come in physical contact with each other, their electron clouds ”collide/overlap” (see Figure 2.2 ii). This overlap enables the electrons from the material with the lowest electron affinity *i.e.*, material M_1 to flow into the material with a greater electron affinity *i.e.*, M_2, donor respective acceptor. The majority of transferred electrons stay in material M_2 even after the separation which entails a negatively charged surplus in the material. In contrast, the material M_1 will be positively charged due to the loss of transferred electrons [58] (see Figure 2.2 iii).

On the macro scale, the surface charge dissimilarity of the two materials entails an electric field, meaning there is a voltage difference between the two materials [34, 59]. The voltage difference can generate an electric signal that can drive a current into an external circuitry or electrical load Z. The generated current can flow through the attached conductive electrodes [34].

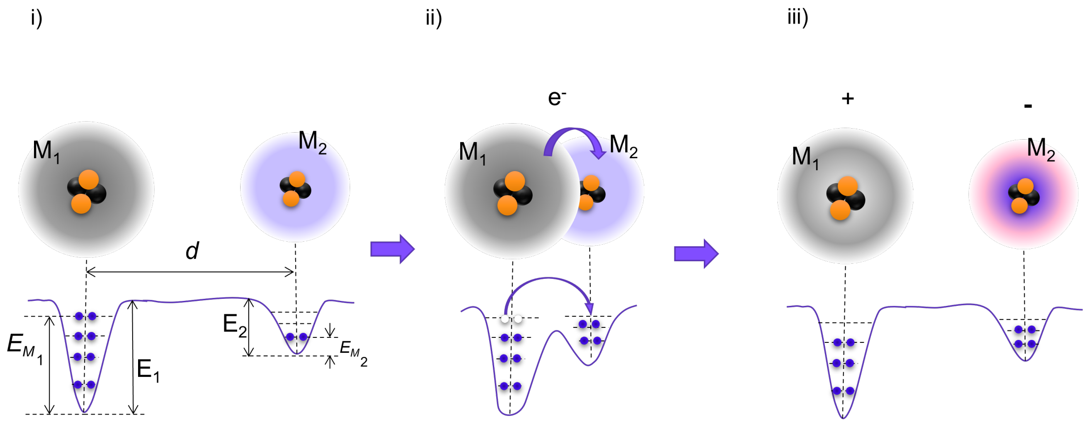

Figure 2.2: *The process of electron exchange between tribo-pair material after physical touch. Regenerated [65].*

Generally, TENG can perform under one of these four modes *i.e.*, 1) vertical contact-separation (CS) mode, 2) lateral sliding mode, 3) single electrode mode, and 4) free-standing mode [34, 58] (see Figure 2.3). Theoretically, each mode is built based on the same fundamental physics shown in Figure 2.2 but, their mathematical expressions can deviate slightly [66].

The vertical CS mode of TENG can be modelled and constructed in two different ways [64, 66] *e.g.* dielectric-to-dielectric or conductor-to-dielectric as illustrated in Figures 2.4a and 2.4b, respectively.

Dielectric-to-dielectric refers to two dielectric materials with opposite electronegativity and a minimal air-gap in between. These have been sandwiched between two parallel plates of conductive electrodes. In contrast, the **conductor-to-dielectric** model contains two layers of electrodes but only one layer of dielectric material. One of the electrodes is attached to the dielectric layer while the second

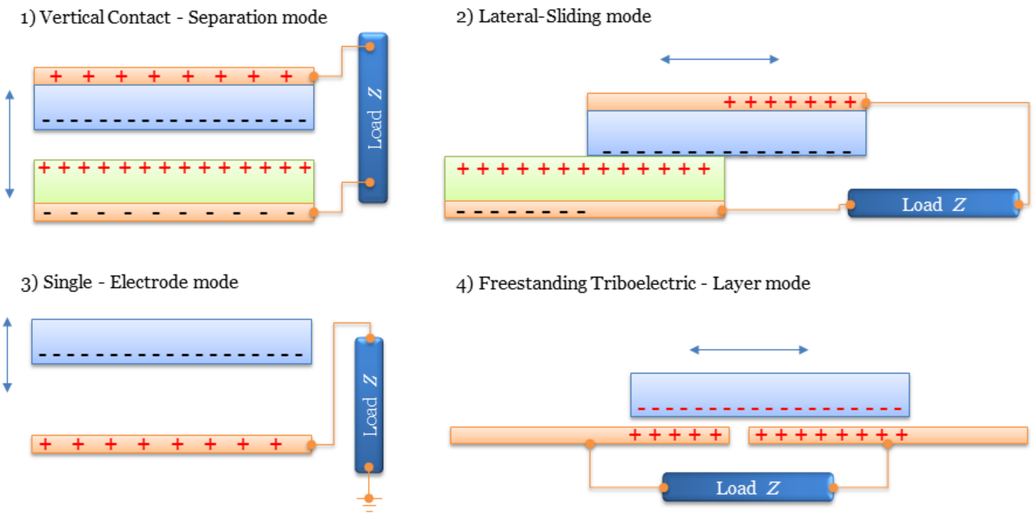

Figure 2.3: *Four general mode of constructing TENG. Regenerated [65].*

electrode has two functionalities. *i.e.*, the second electrode contributes both as an electrode and as a tribopositive layer. Figure 2.4b illustrates the so-called conductor-to-dielectric version of a triboelectric device.

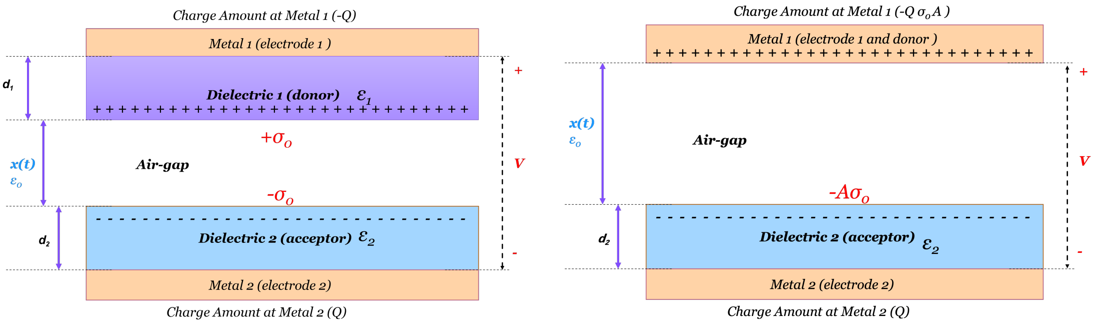

(a) *Dielectric-to-dielectric construction.* (b) *Conductor-to-dielectric construction.*

Figure 2.4: *Two different mode of CS-TENG. Regenerated from [66]*

Parameters in Figure 2.4 can be described as follows. d_1, d_2: show the thickness of the respective dielectric layers along with their permittivities $\varepsilon_1, \varepsilon_2$. A: represents the surface area, σ_0: represents the triboelectric charge density for the respective layer, V: defines the output voltage between electrodes; Q: refers to the number of charges being transferred after the physical contact; $x(t)$: is the air-gap distance that varies with respect to the mechanical force from outside; and ε_0 is the permittivity of air.

Studies conducted previously by researchers to construct TENG-based pressure sensors, have shown that surface treatment of the tirbo-pair can boost its performance [28, 67]. For instance, a ”corona discharge treatment” has improved the performance of pressure sensors up to six times [28]. This treatment polarises the surface of the dielectric material with the help of an ion gun connected to a battery. The needles of the gun spatter negative ions on the surface of the dielectric layer (see Figure 2.5a). However, obtaining extreme charge inequality on the surface of tribo-pair materials can cause the dielectric breakdown of air, which is not desirable at any cost [62]. That is why a breakdown strength threshold needs to be taken into account for corona discharge treatment, to avoid the dielectric breakdown [67]. A dielectric breakdown occurs when the air or any other insulating material, starts to behave as a conductive material due to the existence of high voltage difference or strong electric field [62].

Inductively coupling plasma etching is another method to improve the output electrical signal in a TENG-base pressure sensor [28]. *Inductively coupling plasma etching* treatment is performed on the surface of one of the triboelectric layers (usually on the surface of the dielectric) [63]. This procedure is performed in order to increase the surface roughness which results in an increased output signal voltage of the sensor.

2.4.2 Working mechanism of TENG-Pressure sensors

Pressure sensing mechanisms based on the triboelectric effect are usually modelled and constructed as CS mode TENG [28, 34, 68]. In comparison to other modes, CS-mode TENG provides more advantages, such as durability, less wear out [58], faster response/relaxation time and better sensitivity towards both dynamic and quasi-static pressures [25, 58, 69].

TENG based pressure sensors detect the pressure’s magnitude as the mechanical pressure from the outside compresses the layers vertically so that the two materials in the tribo-pair come into physical contact with each other. At this point, surface charge transfer at the contacted area occurs due to the contact electrification effect (triboelectric effect) [28, 70]. After the pressure is released, the layers return to their initial position due to the existence of a spacer in between them (see Figure 2.5b). At this state, the so-called open-circuit voltage is at its maximum in the sensor

[63]. When the pressure is released, and the layers are separated, the accumulated charges on the dielectric material are then transferred to the conductive electrodes, this charge transfer occurs due to the difference in electric potential between the charged dielectric material and the conductive electrodes [25]. The charges collected on the electrodes can be measured as an electrical signal (output voltage).

The *spacer* between the tribo-pair materials can be fabricated from various materials, depending on the application area and sensor size. Examples include elastic springs, sponges, or different types of polymers [58, 70]. It is important for the spacer to have insulating properties to prevent short circuits between the tribo-pairs and elastic spring spacers made of metal are often manufactured in the substrate layer. This is because metal spacers must not interact with the sensor's components, such as electrodes and tribo-pairs, due to their conductivity [58]. Additionally, the spacer should possess mechanical flexibility, yet resilient enough to restore a controlled distance between the tribo-pairs in the absence of pressure [28, 63].

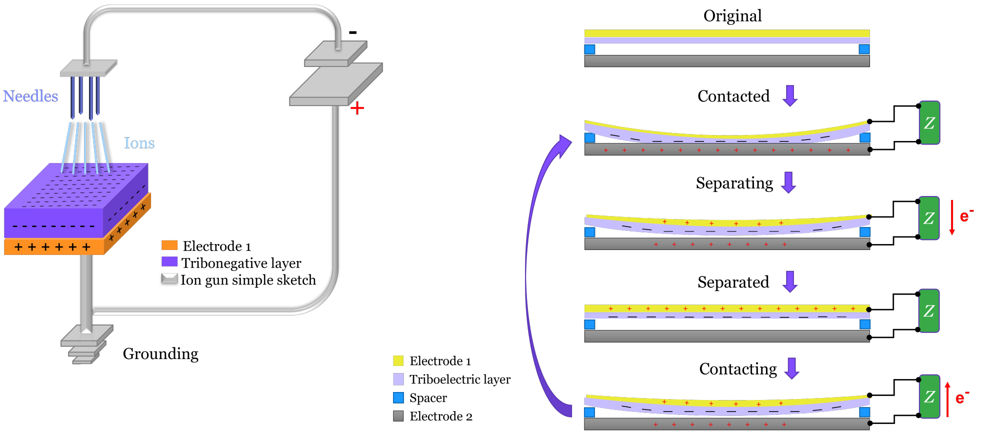

(a) *Corona discharging of the dielectric surface.* (b) *TENG-base pressure sensing mechanism signal generation cycle.*

Figure 2.5: *Corona discharge methodology with ion gun and one complete cycle of TENG-base electrical signal generation. Load Z can be a multimeter too, in order to measure the output voltage from the sensor. Recreated from [28, 62].*

The total output voltage can be calculated by equation (2). The equation demonstrates the relation between voltage V, amount of transferred charges Q and the varying distance between the tribo-layers $x(t)$. Likewise, the surface contact area A between the two layers alters depending on the pressure's magnitude [25]. Parameter x_0 represents the maximum distance between the layers (height of the spacer) and d_{die} is the dielectric constant. Theoretical calculations of this expression are available in detail in Appendix A.

$$V = -\frac{Q}{\varepsilon_0 \cdot A}\left(d_{die} + x(t)\right) + \frac{\sigma_0 x(t)}{\varepsilon_0} \tag{2}$$

Theoretical studies have shown that both TENG-based pressure sensors and capacitive pressure sensors share a similar mechanism for detecting external pressure [58, 66]. However, there are key differences between them. Capacitive sensors rely on variations in capacitance, which occur due to changes in the distance d between the sensor layers [26] (see Figure 2.1b). Additionally, capacitive sensors require an external power source to detect pressure variations. On the other hand, TENG-based pressure sensors exhibit changes in capacitance based on alterations in both the contacted surface area A and the distance $x(t)$ between the layers [66]. Moreover, the latter sensors operate without the need for an external power supply.

The open circuit voltage V_{OC} is linear to the applied pressure [25] (see equation (3)). In the open-circuit state of the sensor, the output electric voltage $V_{(p)}$ of TENG-based pressure sensor, under the pressure P is equal to the V_{OC}. The distance $x(t)$ in equation (2) varies depending on the outside pressure P. To obtain a pressure-related voltage V_{OC}, some mathematical simplifications and substitutions are needed (Appendix A). As a result, the relationship between $V_{(p)}$ and P can be governed by equation (3), where Y and x_0 represent Young's modulus and the initial distance of the air-gap respectively [25]. Subsequently σ_0 and ε_0 represent the triboelectric charge density and air permittivity. It is noticeable that Y, x_0, σ_0 and ε_0 are constants. This means there is a linear relationship between the open circuit voltage $V_{(p)}$ and the outside pressure, P.

$$V_{(p)} = \frac{\sigma_0}{\varepsilon_0}\left(x_0 - \frac{x_0}{Y}P\right) \tag{3}$$

The performance of a triboelectric TENG-based sensing mechanism is influenced by several key factors. These factors can be summarised as follows. Firstly, the physical characteristics and chemical composition of the tribo-pair's materials have a significant impact on the amount of accumulated charges on their surfaces [60–62, 71]. Materials with a greater difference in electron affinity tend to transfer higher amounts of charges upon physical contact [59]. Therefore, the selection of materials for constructing a TENG-based pressure sensor directly affects its sensitivity, durability, limit of detection, and pressure range detection capability [34]. In addition, there exists a strong relationship between the surface charge density (σ) of a tribo-pair and the output voltage (V). The open-circuit voltage (V_{OC}) is directly proportional to the surface charge density of the material [72].

Similarly, the contact surface area A, the initial distance between the layers x_0, and the topographical roughness of the surfaces play a major role in the performance of TENG-base pressure sensors [59, 69, 71]. Furthermore, the sensitivity of TENG-base pressure sensors can be tuned by the thickness of the dielectric layer d_1 [73]. However, when it comes to the thickness of layers it is important that the distance of the air gap between layers must be 5-10 times greater than the thickness of the tribo-pair itself ($x(t) > d_1 + d_2$) [69, 74].

2.4.2.1 Sensor's Key Parameters TENG-based pressure sensors possess key parameters that make them suitable for measuring ICP. These sensors can be designed to be highly sensitive with a low limit-of-detection, allowing for ICP pressure measurements [64, 68]. Sensitivity and limit-of-detection can be adjusted by selecting appropriate materials, optimising the distance between the tribo-layers, controlling the dielectric thickness, and considering the topographical geometry of the surface [58, 61, 68]. Moreover, TENG-based pressure sensors have demonstrated reliable long-term stability in their output signal [28, 34]. For example, a TENG-based pressure sensor made from PTFE and Al exhibited stable output signals even after 10^8 cycles in *in vitro* and wet environment.

Generally, the linearity of pressure sensors depends on the range of the pressure they measure and TENG-based pressure sensors are not an exception in this ability [28, 75]. In particular, sensors based on TENG have shown linearity in the pressure range between $0 - 2\,\text{kPa}$ but for pressure magnitudes greater than $2\,\text{kPa}$, the sensor performed with poorer linearity [68]. In contrast, other TENG-based pressure sensors have shown desirable linearity for pressure magnitudes over $70\,\text{mmHg}(9.3\,\text{kPa})$ but poor linearity for lower pressure magnitudes [28, 34].

It is important to mention that, the linearity of piezoresistive and piezoelectric pressure sensors for lower pressure ranges is better than for the TENG-based one [76]. The response time of TENG-based pressure sensors are slower than piezoelectric sensors but similar to piezoresistive and capacitive, depending on the manufactured material [34]. However, TENG-based pressure sensors are able to detect both dynamic and quasi-static pressure variations which the piezoelectric ones are lacking [65].

Output signals from TENG-based pressure sensors can be affected by humidity and wetness which makes their environmental robustness vulnerable [25, 45]. Likewise, the temperature variation can affect the permittivity of the PDMS layer [1], which can influence the output signal from the sensor. For instance, moisture surroundings can significantly influence the charges accumulated by triboelectricity [77]. Air conductivity increases in a humid environment which in turn leads to a leakage of charges from the surfaces [78]. That is why humidity and wetness cause an alteration in output signal magnitude and unreliability in the performance of the sensor. Furthermore, humidity can increase the chances of corrosion and it is hazardous to all body parts [79].

For these reasons, the encapsulation of TENG-base pressure sensors *in vivo* is a very important factor [25]. A proper encapsulation should be able to protect the sensor, against the intrusion of wetness and effect as little as possible or ideally not influence at all the performance factor of the sensor [28]. Recently researchers have overcome the obstacle of encapsulation, while the sensor has preserved its stability and bio-compatibility [28, 63]. For instance, research was done by Z. Liu *et al.*, at the Chinese Academy of Science, in which a nude TENG-based pressure sensor has been encapsulated with the 87.5 µm PDMS layer. However, the sensitivity and limit-of-detection for low-pressure magnitudes have declined as a result of the encapsulation [25, 28, 63].

2.4.2.2 Required Capabilities: The requirements and challenges that have been overcome by TENG-based pressure sensors, developed by former researchers, is explained as follows. Being self-powered is one of the major advantages of TENG-based sensors. In addition, the choice of material for fabricating a TENG-based sensing mechanism is broad [59]. This advantage enables the sensor to be manufactured from bio-compatible materials with mechanical flexibility. It is important to mention that the choice of material has a significant influence on the sensor's essential key factors such as sensitivity, pressure range, and limit-of-detection. Detailed information about the materials will be provided in Section 2.4.3.

There are some shortcomings to triboelectric-based pressure sensors as well. For instance, their size can not be manufactured arbitrarily small, since the strength of the output signal is strongly correlated to the contact surface area of the tribo-pairs [45]. The smaller the contact area the weaker the triboelectrification effect (fewer charges transferred) [70, 76]. The durability and mechanical flexibility of TENG-based pressure sensors have been evaluated in *in vitro* tests [28, 68]. Results have shown that the sensor is capable of withstanding high-pressure magnitudes and generating an output signal even at pressures greater than or equal to 200 mmHg.

2.4.3 Material

The choice of material for TENG is broad since every material is able to produce some sort of triboelectric effect [59]. However, to achieve the best performance and fulfil the uncompromising requirements for ICP sensor the choice of material is a crucial factor [34, 59, 69].

Theoretically, it is advantageous for tribo-pair materials to have significant differences in their charge affinities to facilitate the transfer of a larger amount of charges and obtain a stronger output signal [59]. However, in practical applications, for a pressure sensor to monitor ICP, the significant distinction in charge affinity is not the only property that needs to be considered. Alongside their chemical properties, the physical and mechanical characteristics, such as elasticity, stress tolerance, and bio-compatibility, are also important factors to be taken into account [59, 62].

Materials considered in this study for designing and simulating the TENG-based pressure sensor to monitor ICP is described in Table I. Figure 2.6 shows the geometrical shape of the designed sensor (Figure 2.6a). Figure 2.6b illustrates a zoomed version of the sensor's cross-section image, with its four main components. *i.e.*, gold (Au) electrode and PDMS (membrane), the air-gap in between and its spacer and the bottom electrode made from Al. However, the physical specifications and dimensions details for these materials will be provided in Section 3.1.1.1.

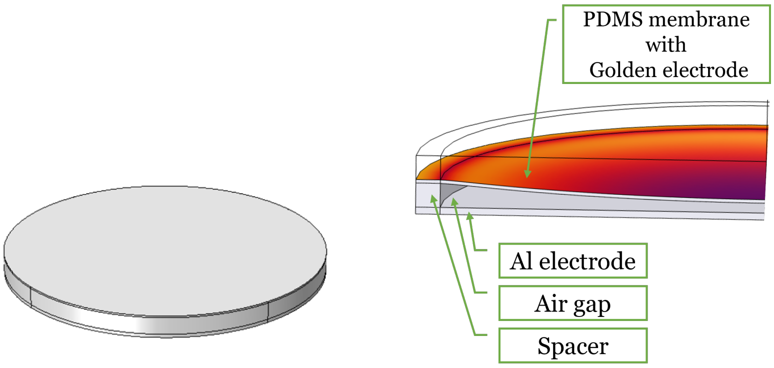

(a) *Complete geometry of the designed sensor.*

(b) *Zoomed illustration of the sensor.*

Figure 2.6: *The cylindrical shape of the sensor (on the left). A cross-section of the sensor and its different components (on the right).*

Table I: Materials and their purpose used for the modelled pressure sensor.

Material name	Objective
PDMS	Tribonegative dielectric layer
Au	Electrode 1
Aluminum (Al)	Tribopositive layer and Electrode 2
Ethylene-vinyl acetate (EVA)	Spacer between tribo-pairs

3

Method

This project commenced with a comprehensive literature review aimed at acquiring theoretical knowledge on brain physiology, intracranial pressure (ICP) mechanism and four major pressure sensor technologies (piezoresistive, capacitive, piezoelectric and triboelectric) as well as the state-of-the-art in ICP sensors. Research was conducted utilising the available databases at the Chalmers Library to gather relevant information for this thesis.

Since this thesis focuses on two main areas - the modelling of a self-powered pressure-sensing mechanism and the construction of a test bench for a brain phantom - it is logical to divide the methodology into these two subsections. A conventional pressure sensors will be used to verify the pressure variations from the test bench.

3.1 Modelling and Simulation Methodology

Based on technical knowledge gathered from the literature and following the specifications mentioned in Section 1.4, a design for the triboelectric sensing mechanism has been proposed. A simplified version of the designed pressure sensor was simulated using COMSOL Multiphysics 6.1 software. These simulations were conducted to assess the behaviour of the modelled sensing mechanism under different pressure levels of ICP. Furthermore, MATLAB R2021b software has been used to verify the linearity of data points collected from COMSOL simulations. For linearity verification, a ”linear regression algorithm” has been utilised. Built-in functions `polyfit` and `polyval` from the MATLAB have been used. The algorithm determines the smallest sum of squared residuals that is possible for the data set and produces a linear function which could fit the data points with the shortest possible distance between the line and the data points [80]. To evaluate how accurately the regression line fits the data set, the $R-squared$ value has been calculated too. $R-squared$ value varies between 0 and 1 ($0 < R^2 < 1$). Where $R^2 \approx 0$ indicates that the data points deviate significantly from a perfect linear fit, while $R^2 \approx 1$ indicates that the majority of the data points can be well-fit by a linear model [81]. In other words, it quantifies the statistical strength of the linear relationship between the two parameters. Graphical illustrations have been composed by Microsoft PowerPoint and Affinity Designer 2 software.

3.1.1 Methodology for COMSOL Simulations

The simulation has been done to develop a computational model in a 3D environment. However, the geometry of the modelled sensor is symmetrical around the x-axis. In order to save the simulation time and reduce computation complexity, simulations were performed in a 2D axis-symmetrical environment. In the simulation modules, a combination of `Structural mechanics (Solid mechanics)` and `Electrostatic` physics/interfaces have been exploited to obtain the results for the triboelectric interface. Additionally for the moving parts, such as the membrane, the top electrode and the air gap between the membrane and the bottom electrode, a `Moving Mesh` module has been declared. The following five steps generally describe the workflow process in the COMSOL software.

1. **Define geometry:** To define each geometry's shape, position and dimension. *e.g.* geometry for membrane, spacer and electrodes.
2. **Define Material:** Defining material for each geometry among their mechanical and electrostatic properties. *e.g.* Gold (Au), Polydimethylsiloxane (PDMS), Ethylene-vinyl acetate (EVA) and Aluminium (Al).
3. **Boundary conditions:** Defining the boundary condition for the `Solid Mechanics` and `Electrostatic` physics.
4. **Meshing:** COMSOL utilises meshing to divide the modelled structure into smaller finite elements, such as blocks and triangles, as it is based on the finite element method (FEM) simulation.
5. **Studying:** Stationary studies are used to extract the results from the derived values by the simulations.

3.1.1.1 Geometry: The sensor has a cylindrical shape with a height of 0.5 mm and diameter 10 mm. To satisfy the boundary conditions for the `Electrostatics` interface, the sensor needs to be surrounded by air (See Figure 3.1). A cylindrical geometry with identical properties to air is generated around the sensor. The air geometry has a volume of 2645.8 mm^3 and its surrounding boundaries are defined as `Ground`. Figure 3.2 presents a 2D cross-sectional view of the designed sensor, illustrating the dimensions and position of each geometry used for the simulation. It is worth to mention, that the Au layer is much thinner than the PDMS layer which is why no specific geometry for Au has been built in COMSOL. Consequently, the top `boundary line` of the PDMS has been assigned as Au. The goal of this simplification is to reduce the complexity of the model for COMSOL software and hence to reduce the time for meshing and calculations. However, the physical and chemical properties of the gold from the COMSOL material library as been assigned to this boundary line. This is done to reduce errors in the simulation results. Furthermore, under the `Solid Mechanics` interface `Thin Layer` module has been exploited for the Au layer to retain its mechanical attributes regarding pressure and stress.

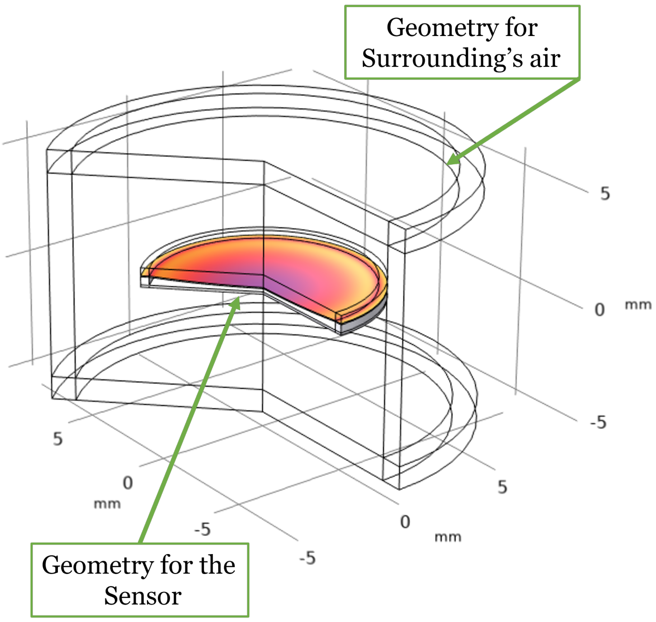

Figure 3.1: *Geometries of the sensor device surrounded by the air volume, in the COMSOL software.*

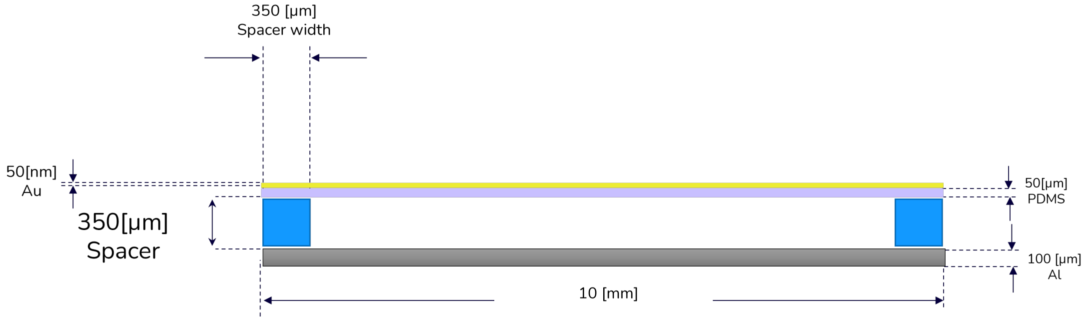

Figure 3.2: *Dimension and the geometry of the designed sensor.*

3.1.1.2 Material: After defining the geometries for each segment of the sensor, the material and their properties have been defined. Table II describes the material properties employed in the simulation along with their functional role in the sensor. The relative permittivity ε_{Au} for gold, varies between 1-4 depending on the frequency of the applied electric field [82]. However, for this study, it has been set to 1.

Table II: Parametric values used in `COMSOL` simulation.

Specifications		Au	PDMS	EVA	Al
Functional role		**Electrode 1**	**Dielectric layer**	**Spacer**	**Electrode 2**
Poisson's ratio	ν	0.44 [83]	0.49 [84]	0.48 [85]	0.33 [83]
Young's modulus	Y	70 GPa [86]	2 MPa [84]	80 MPa [87]	70 GPa [88]
Density	ρ	19300 kg/m^3 [89]	970 kg/m^3[90]	950 kg/m^3 [85]	2700 kg/m^3 [83]
Relative permittivity	ε_r	1	2.75 [91]	2.3 [87]	1
Surface charge density	σ	-	c [91],[92]	-	-

3.1.1.3 Multiphysics: To perform simulations, multi-physics interfaces were combined: `Solid Mechanics` and `Electrostatics`. The `Solid Mechanics` interface was used for the structural analysis of the sensor, including evaluating the stress, elasticity and displacement of the membrane in response to different pressure levels from ICP. Additionally, it was used to assess the relationship between the contact area, A, between the PDMS and Al layers and the applied pressure. The `Electrostatics` interface was employed to analyse the electrical potential between the layers and its variation based on the external pressure. Furthermore, declaring the surface charge density for the PDMS surface and assigning the Al layer as `Floating potential` have been accomplished under the `Electrostatics` interface. Similarly, for defining the `Ground` reference points in the simulation `Electrostatics` interface has been utilised.

3.1.1.4 Meshing and Study Since simulations are mostly performed in 2D an `extra fine` meshing size has been built. To prevent calculation errors and achieve results that are as near to real-world behaviour as possible. The pressure variable on both interfaces (`solid mechanics` and `electrostatics`) is not time-related. That is why for obtaining results a `stationary study` has been performed. A parametric sweep was conducted over a pressure range of $0 - 70\,\text{mmHg}$ with a step size of $1\,\text{mmHg}$. This particular pressure range and step size were selected to mimic the required pressure range and resolution of the sensor, as outlined in Section 1.4.1.

3.2 Test Rig Setup

A test rig, as shown in Figure 3.3, has been developed to simulate the pulsation of the phantom brain in response to pressure variations in its ventricle. This setup enables the real-world simulation of the phenomenon. It was constructed as a simplified version capable of emulating the fundamental behaviours and characteristics necessary for measuring ICP. Specifically, the model must exhibit realistic mechanical displacement and pulsation to effectively assess a pressure sensor intended for use in the targeted environment (within the skull).

The test rig has been constructed in collaboration with another master thesis done by C. E. Dahlberg [29]. Information about the instrument's specification is provided in Table V.

3.2.1 Brain Phantom

Silicone gel/rubber *SF00 - RTV2 silicone* has been used to construct the brain phantom which represents the brain matter. The silicone solution consists of two components (base and catalyst) which needed to be mixed in a ratio of 1:1 according to the datasheet before casting [93]. Once the solution was mixed it have been poured into the mould cavity for cross-linking (hardening) process. This specific silicone has been used to manufacture brain phantoms in the former study done by S. S. Basati and colleagues [94]. It was selected based on its mechanical properties, which bear some resemblance to brain tissue [93–96]. In Table III basic mechanical properties of the brain tissue are compared with the *SF00 - RTV2 silicone.* .

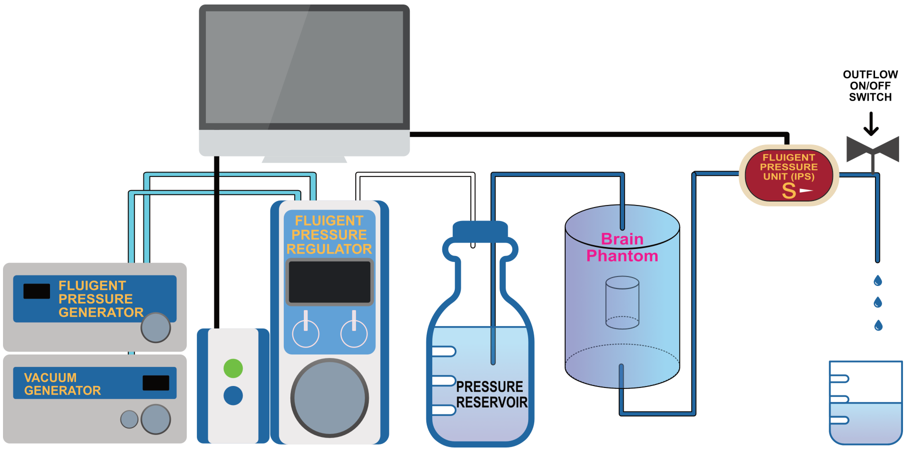

Figure 3.3: *Test rig setup, from left to the right. It starts from the pressure-, vacuum-generator, to the pressure regulator, into the reservoir, and from the reservoir into the brain phantom's ventricle void, further through the incline pressure sensor (IPS) pressure and ended up dropping in a beaker or blocked by ON/OFF switch.*

Table III: Mechanical properties of brain tissue and silicone gel.

Property	SF00 - RTV2 silicone	Brain Tissue (Grey-/White-matter)
Elastic modulus	4.6 kPa	2.9 kPa
Density	1.06 g/mL	1.05 g/mL

3.2.2 Modelling Phantom Brain

To streamline the geometry of the brain phantom, a cylindrical shape with a void representing the ventricle has been chosen. This simplification allows for a more straightforward representation of the phantom's structure. Figure 3.5a shows the 3D-printed mould for the one half of the cylindrical shape phantom brain. Likewise, Figure 3.5b shows the mould for the ventricle cavity placeholder.

For designing the moulds of the brain phantom, the 3D modelling software `AutoDesk Inventor 2023` was utilised. Additionally, the software `Prusa Slicer 2.5` was employed to map and prepare the constructed model for 3D printing. The 3D printing of the moulds was carried out using the `Original Prusa i3 MK3S` printer and *Polyethylene Terephthalate + Glykol* (PETG) filament.

The model was a composite shape formed by combining two halves of one cylinder, each with a curved side and an open flat side. These two halves represent the brain phantom which is shown in Figure 3.5c. After casting, the two half-cylinders were positioned in such a way that the flat side faced each other, creating a hollow space in the middle (ventricle cavity). The hollow space has a smaller cylindrical shape that is completely enclosed within the larger cylindrical shape.

The 3D design of the brain phantom mould underwent three iterations, as depicted in Figure 3.4. These upgrades were necessary to address the limitations and shortcomings observed in the earlier generations of the design. Further information regarding the specific limitations will be discussed in Section 5.3.

Figure 3.4 (a) displays the *1st-generation* mould designed for the brain phantom. The mould consisted of a half-cylinder shape, with a cross-shaped structure and a half-sphere bulge in the middle intended to be placed on top of the half-cylinder. The sphere served as a placeholder for the ventricle void. However, when casting the phantom brain in this mould, curvature was often observed on the flattened surface of the cylindrical half. This curvature was caused by the presence of the cross-shaped structure during the casting process. To address this issue, a second-generation mould was designed.

The *2nd-generation* of the mould is depicted in Figure 3.4 (b). The brain phantom's half cylinder is composed of two parts: the base and the shell. On top of the base, a flat-surfaced cover with a smaller half-cylindrical bulge at the bottom was incorporated to replicate the ventricle void. Figures 3.5 showcase the moulded brain phantom and a 3D-printed version of the *2nd-generation* mould. The casting process in this mould was susceptible to the formation of pinholes, which are caused by air bubbles on the surface. These pinholes could result in pressure leakage from the ventricle voids.

Lastly, the *3rd-generation* design, shown in Figure 3.4 (c), consists of two parts: a bottom cylinder shape with a built-in ventricle void, and a cork that can seal the ventricle void. The *3rd-generation* design was implemented to address the issue of pressure leakage. Dimensions for the mould are provided specifically for the 3rd generation in Table IV.

3.2.3 Constructing the Brain Phantom

For preliminary tests, several prototype brain phantoms have been manufactured. These prototypes were considered to have 3-4 times smaller dimensions than the actual brain phantom, which was planned to be manufactured for the final tests. These preliminary attempts were performed with the aim to save the manufacturing

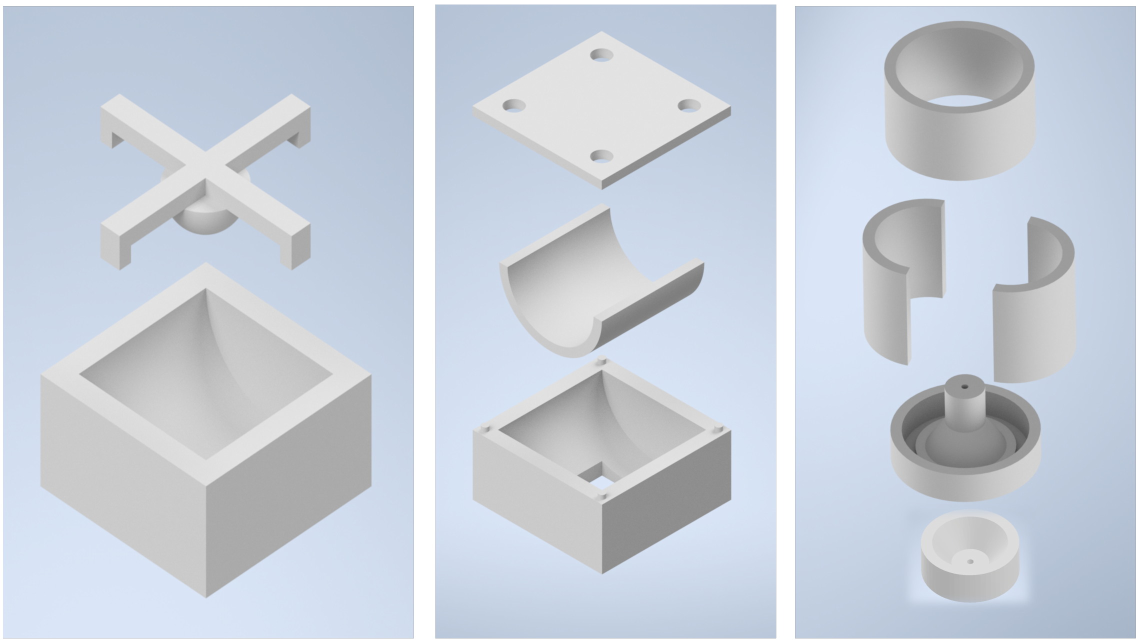

a) Gen.1 Spherical ventricle b) Gen.2 Cylindrical ventricle c) Gen.3 Entire Cylinder form

Figure 3.4: *Three different generations of the 3D designed mould for the brain phantom.*

Table IV: Dimensions for the *3rd-generation* mould.

Dimensions	Length [mm]
Cylinder Height	28 ± 0.5
Outer diameter	32 ± 0.5
Inner diameter	25 ± 0.5
Ventricle height	10 ± 0.5
Ventricle diameter	10 ± 0.5
Cork top diameter	20 ± 0.5
Cork bottom diameter	10 ± 0.5

material and identify the challenges, weaknesses and risks of the design. The results discussed in Section 5.3 are obtained only by experimenting on the prototype brain phantom. However, the findings from this study can be applied to future fabrication processes of larger, actual brain phantoms. Implementing these results can help avoid potential mistakes, reduce time waste, and ensure the overall effectiveness of the fabrication process.

3.2.3.1 Prototype Phantom Brain: Silicone *SF00 - RTV2 silicone* mixture was poured inside the printed mould as shown in Figure 3.5a. After the cross-linking (hardening) process, the two halves were assembled/glued together since the cavity needed to be pressure-tight. In order to pressurise the ventricle cavity, two capillary tubes were inserted from the top and the bottom of the cylinder shape ventricle.

To achieve the sealing of the two halves, a silicone mixture was applied to the flattened surfaces of the cylinder halves after their cross-linking process was completed, and then they were assembled together. This approach aimed to minimise the use of *Permabond POP Primer* and *Permabond 105 Adhesive cyanoacrylate* in the design.

The decision to minimise the use of *Permabond 105 Adhesive cyanoacrylate* was motivated by its negative impact on the elasticity of the silicone rubber. Its use resulted in increased brittleness in the applied areas, which posed a higher risk of breakage. Therefore, reducing reliance on these adhesive materials was necessary to maintain the desired flexibility and integrity of the brain phantom. Detailed differences will be discussed as a result in Section 5. Figure 3.5d shows the glued version of the brain phantom with its capillary tubes.

3.2.4 Instruments and Experimental Procedure

Instruments used in the test rig setup are described in Table V. A tubing kit from *Fluigent®* with 250 µm inner diameter tubes have been used to transfer the pressurised liquid.

Figure 3.3 shows the process starts from left to right. The liquid inside the enclosed reservoir made of *DURAN ®* is pressurised using the pressure generator

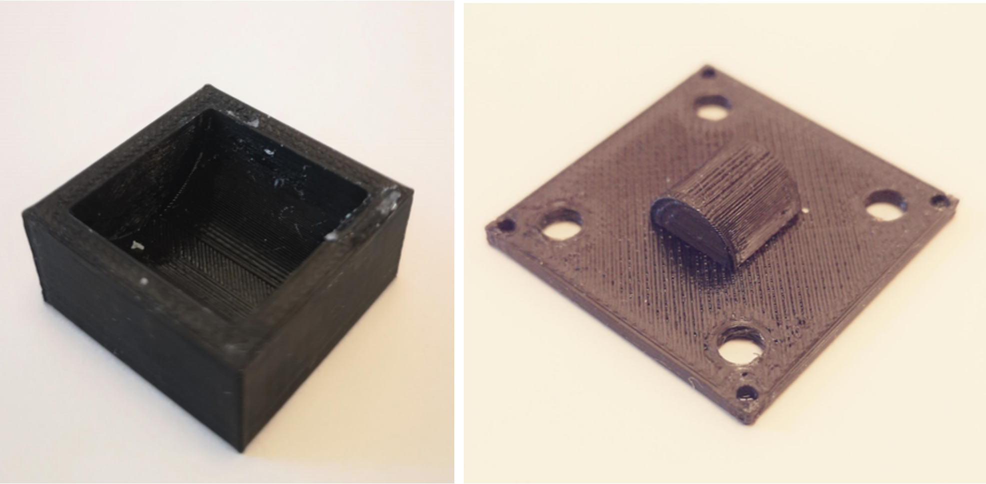

(a) *Half cylinder mould* (b) *Ventricle cavity mould.*

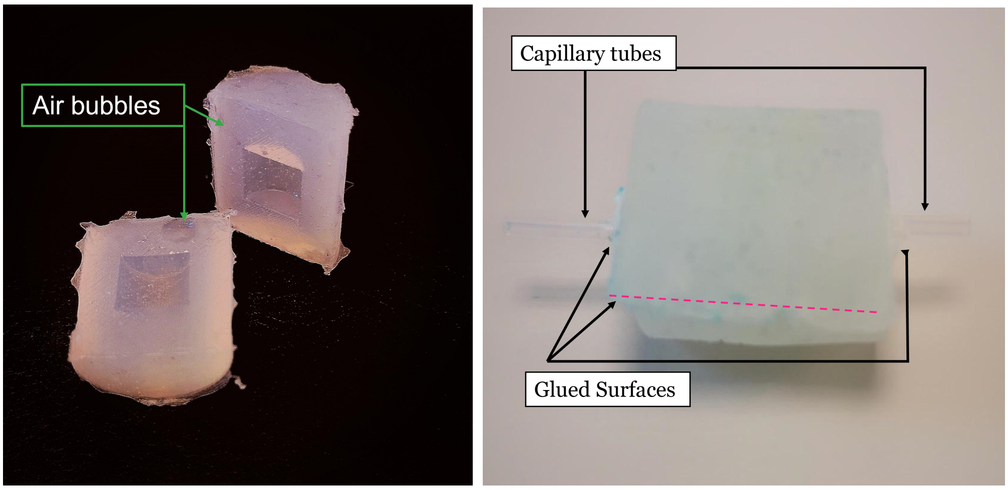

(c) *Phantom brain halves.* (d) *Glued phantom brain.*

Figure 3.5: *3D-Printed 2nd-generation moulds for the brain phantom and its ventricle cavity (top figures). Two Halves of brain phantom made from silicone and its glued version (bottom figures).*

Table V: List of instruments and their objective in the experiment.

Name	**(Specification)**	**Objective**
Fluigent	FLPG plus	Pressure generator
LabTech	VP18 plus	Vacuum generator
Fluigent	Push Pull	Vacuum Pressure-Based Controller
DURAN	Pressure plus	Pressure tight reservoir
Fluigent	Pressure unit (S)	Inline pressure sensor
Fluigent	Tubing Kit	Tubes for transferring pressure

from *Fluigent FLPG®*. This pressurisation is facilitated by the pressure regulator from *Fluigent PushPull®*. The pressure regulator is connected via a USB cable to a computer and allows the user to regulate the pressure variations with the help of its software OxyGEN 2.2. The regulated pressurised liquid flows through the brain phantom's ventricle cavity before it ends up in the inline-pressure sensor (*Fluigent Pressure unit (S)*). The latter pressure sensor served as a checkpoint to monitor the pressure variation after the brain phantom.

4

Ethics

Intracranial pressure (ICP) sensors have significant potential for monitoring and managing brain health conditions [11]. However, it is essential to carefully address and evaluate the ethical considerations associated with implantable sensors that measure changes in pressure within the skull and utilise their signals for diagnoses, just like any other biomedical device [97].

It is a must for the development of any medical device to take proper precautions and prioritise the safety of the patients [98]. An implantable triboelectric nano-generator (TENG)-based pressure sensor is no exception. As an engineer, it's obligatory to have proper precautions for the safety of the implant and eliminate the potential hazards which can threaten the health status of the patient [98].

Implanting a sensor inside the skull, which is a highly sensitive environment in the body, involves complex surgeries that can lead to post-surgery complications and pose life-threatening risks of infections [11]. Additionally, these procedures are time-consuming and have economic implications for the healthcare system [11, 98]. Therefore, it is ethically necessary to conduct long-term evaluations of the sensor for its *in vivo* application to identify potential risks. In addition, a proper assessment of the risks and probabilities of the device failure and the risk of infection or adverse tissue reactions have to be conducted. Furthermore, patients that receive an implant must be provided with transparently comprehensive information about the purpose, risks and benefits of the sensor.

The material used for the manufacturing of a sensor component will have an ecological impact [98]. That is why environmental sustainability and bio-compatibility must be a primary focus throughout the design process to make the design safe for clinical use.

Data from pressure measurements done by an implantable ICP sensor is sensitive information and it can put the patient's privacy in jeopardy. That is why such data must be protected from unauthorised access and breaches. Both engineers that design such sensors and healthcare providers must establish appropriate data protection protocols to guarantee that the confidentiality of the patients is maintained.

The development and manufacturing of a TENG-based pressure sensor can be expensive, and the implantation process may be limited by the requirement for specialised surgical expertise, as it is a relatively new technology [58]. However, ensuring ethical access to these sensors for all individuals in need is of paramount importance.

TENG-based pressure sensors have the potential to enhance patient care and improve the outcomes in the neurology field. However, ethical aspects such as patient safety, data privacy, ecological impact, and ease of access must be considered and managed carefully. It must promote safety, quality and reliability both for the patients and the healthcare.

5

Result

Results from the literature study, simulations and test rig setup will be discussed in separate subsections. The results from the literature study, include the evaluation of different sensing mechanisms' technology for an intracranial pressure (ICP) implant, in Section 5.1. The simulation results are presented in Section 5.2, where the mechanical and electrostatic properties of the designed sensor were evaluated. Finally, this chapter ends with the results from the test rig construction and experiment, in Section 5.3.

5.1 Result From the Literature Study

Based on the literature study, four conventional technologies for pressure sensors (piezoelectric, piezoresistive, capacitive, and triboelectric) were reviewed and evaluated. Table VI presents a general comparison of the key parameters and required capabilities for implantable ICP sensors.

The rows in Table VI are divided into two main sections for each sensor type. The first section of the table, located in the top half, displays the key parameters of the pressure sensors. The second section, in the bottom half, showcases the required capabilities of each sensor. Each sensor type is represented by its own column, which is further divided into two subdivisions. The first subdivision, denoted by the "(+), (-), and (+/-)" signs, indicates the corresponding score of each attribute. The second subdivision, adjacent to the first one, shows the number of other attribute(s) that need to be considered as a trade-off.

A positive score (+) is assigned to a specific requirement if the sensor fulfils that attributes sufficiently well to function as an ICP sensor. Conversely, a negative score (-) is given if the sensor cannot meet that requirement. Cells marked with a (+/-) sign indicate that a particular ability can be compromised and traded off with another ability, as indicated by the corresponding row number(s). For example, in order to reduce power consumption in a piezoresistive sensor, a trade-off must be made between sensitivity and durability [1, 34, 45, 76]. Attributes that are highlighted in yellow, are considered fundamental key parameters and requirements for a long-term implantable ICP sensor [1, 11]. That is why a sensor technology that lacks such an attribute will not be able to perform as a long-term implantable ICP sensor [1].

According to the results from Table VI summed up as (TOTAL SCORE), piezoresistive sensors have the highest positive score. However, they rely on an external power supply, which is a disqualification for implantable ICP sensors [11]. Triboelectric sensors, on the other hand, rank second in terms of positive scores and offer the flexibility to adjust (trade-off) several parameters to fulfil most of the required attributes.

Triboelectric sensors can exhibit linearity in their output signal, but this linearity is typically observed within a specific operating pressure range [25, 34]. They are also sensitive to wet environments [25], which is an important requirement considering their implantation inside the human skull [11]. However, this obstacle has been overcome by appropriately encapsulating the sensor [25, 63]. An experiment conducted by Zhuo Liu *et al.*, in 2018 evaluated a triboelectric pressure sensor *in vivo* to monitor heart pressure [28]. The sensor was encapsulated with 80 µm thickness of polydimethylsiloxane (PDMS) layer and the results demonstrated that the sensor signals remained undisturbed even after 10^8 cycles with a linearity $R^2 > 0.99$. Further, the encapsulation process showed enhancement in other attributes of environmental robustness as well. For instance, blood cells did not accumulate on the surface of the encapsulation. It should be noted that the encapsulation process had a slight impact on the sensitivity of the sensor [28]. However, the sensitivity of a triboelectric nano-generator (TENG)-based pressure sensor can be adjusted using alternative strategies [61, 68]. These strategies include implementing different surface treatments on the dielectric layer, such as the introduction of micro-structures (*e.g.* pyramids, cubes, or random structures created using sandpaper), as well as utilising surface treatments like corona charging and inductively coupled plasma treatments [28, 61]. These techniques offer flexibility in fine-tuning the sensor's sensitivity to meet specific requirements.

Triboelectric sensing mechanisms are typically not manufactured at the same small scale as piezoresistive sensors, specifically in micro-sized dimensions [56]. However, there is potential for designing TENG-based pressure sensors with small sizes that meet the specific requirements discussed earlier in Section 1.4.1. For instance, researchers such as Wang *et al.*, (2014) [99], Zhuo Liu *et al.*, (2018) [28], G. Cheng *et al.*, (2021) [68], and K. Venugopal (2022) [64] have successfully constructed and modeled TENG-based pressure sensors with surface areas ranging from 1 cm^2 to 5 cm^2. These studies demonstrate the feasibility of designing compact TENG-based pressure sensors that fulfil the desired size requirements.

Table VI: Evaluation scores for different pressure sensors based on literature study.

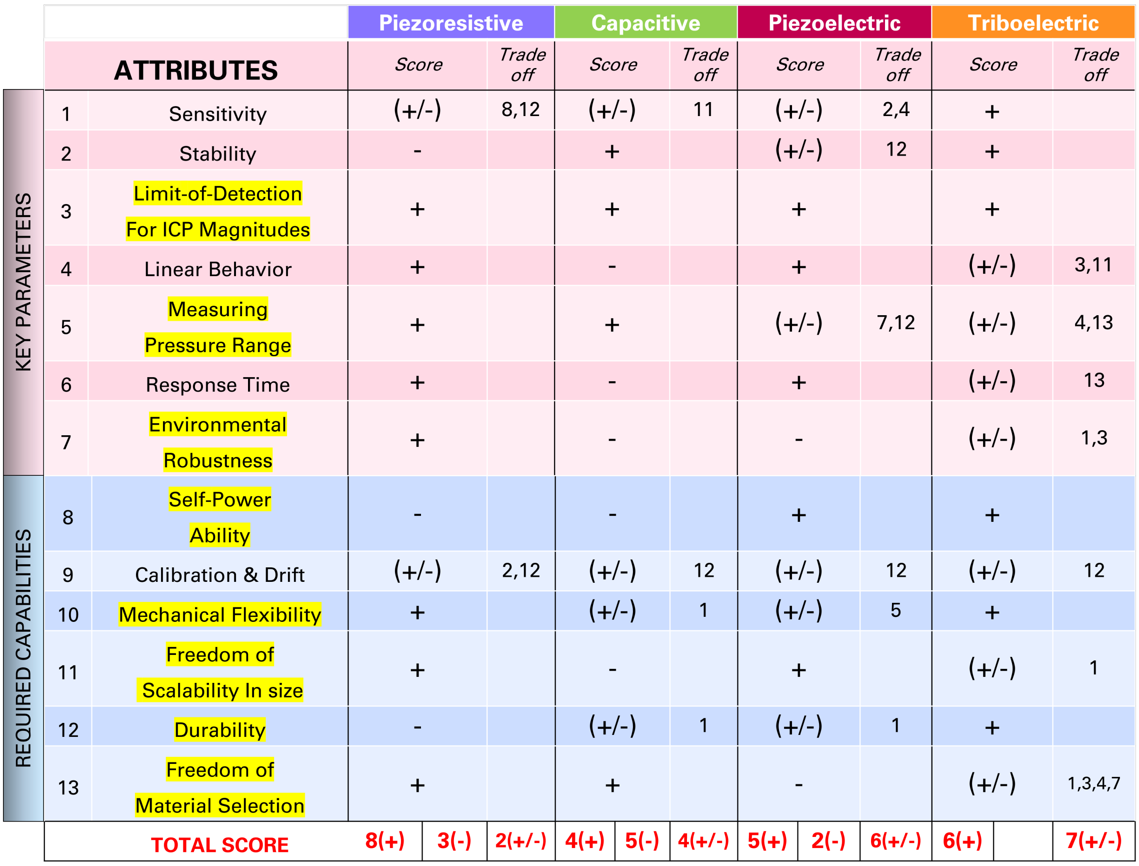

			Piezoresistive		Capacitive		Piezoelectric		Triboelectric	
		ATTRIBUTES	*Score*	*Trade off*	*Score*	*Trade off*	*Score*	*Trade off*	*Score*	*Trade off*
KEY PARAMETERS	1	Sensitivity	(+/-)	8,12	(+/-)	11	(+/-)	2,4	+	
	2	Stability	-		+		(+/-)	12	+	
	3	Limit-of-Detection For ICP Magnitudes	+		+		+		+	
	4	Linear Behavior	+		-		+		(+/-)	3,11
	5	Measuring Pressure Range	+		+		(+/-)	7,12	(+/-)	4,13
	6	Response Time	+		-		+		(+/-)	13
	7	Environmental Robustness	+		-		-		(+/-)	1,3
REQUIRED CAPABILITIES	8	Self-Power Ability	-		-		+		+	
	9	Calibration & Drift	(+/-)	2,12	(+/-)	12	(+/-)	12	(+/-)	12
	10	Mechanical Flexibility	+		(+/-)	1	(+/-)	5	+	
	11	Freedom of Scalability In size	+		-		+		(+/-)	1
	12	Durability	-		(+/-)	1	(+/-)	1	+	
	13	Freedom of Material Selection	+		+		-		(+/-)	1,3,4,7
		TOTAL SCORE	**8(+)** **3(-)**	**2(+/-)**	**4(+)** **5(-)**	**4(+/-)**	**5(+)** **2(-)**	**6(+/-)**	**6(+)**	**7(+/-)**

The triboelectric sensing mechanism developed in this study is designed to measure variations in ICP on the epidural membrane of the skull, taking advantage of its flattened geometry as shown in Figure 5.1. The zoomed-in portion of the image highlights the placement of the sensor inside the skull and the arrow is pointing to the sensor.

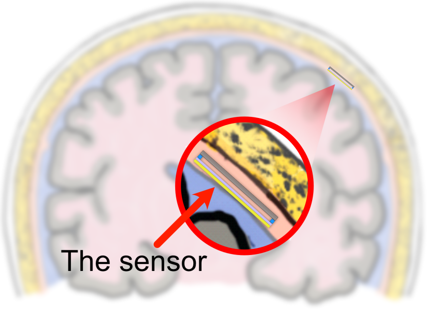

Figure 5.1: *Preliminary suggestion for the positioning of the designed sensor implant.*

5.2 Simulation's Results

In the COMSOL simulations a pressure range between $0-70\,\text{mmHg}$ has been applied to the sensor. The `Parametric sweep` function with 1 mmHg step setting has been utilised to apply these pressure levels. Results from the COMSOL simulations are divided into two parts. *i.e.*, `Solid Mechanics` and `Electrostatics` analysis. The `Solid Mechanics` section discusses the results from the PDMS and gold (Au) membrane displacement as well as the deformation and stress experienced by the membranes. Subsequently, the `Electrostatics` section evaluates the relationship between the different pressure levels and the potential variation between the layers. This section ends with the results obtained from a modified version of the sensor, designed specifically to investigate the impact of spacer size on the behaviour of the sensor.

5.2.1 `Solid Mechanics` Analysis

Simulation results show that the vertically applied pressure range between $0-70\,\text{mmHg}$ can displace the top layer of the sensor. The top layer of the sensor, serving as the sensing membrane, consists of a nano-electrode layer made of Au attached to the back of a PDMS layer. In Figure 5.2 a graphical visualisation of the membrane deformation is presented (on the left side in Figure 5.2a). Likewise, Figure 5.2b shows the analytical graph of the membrane displacement with respect to applied pressure levels. Using `Boundary Load` from the `Solid Mechanics` to apply different pressure magnitudes on the surface of the Au electrode which is attached to the back of PDMS membrane. The circumference of the membrane, spacer and aluminium (Al) layer has been fixed with the help of `Fixed Constrain`.

5.2.1.1 Membrane Displacement Analysis: When the pressure is applied, the membrane deforms, which displaces the tribo-negative layer of PDMS towards the bottom electrode made of tribo-positive Al. PDMS comes into contact with the Al surface, resulting in triboelectrification. During this process, the Al surface becomes positively charged, while the PDMS surface becomes negatively charged, acting as the donor and acceptor, respectively. As these layers separate, the charge separation generates a potential difference between the electrodes (Au and Al), which drives an external circuit. In practical implementation, positive charges from the Al layer transfer towards the negative charges through the external circuit, while negative charges from PDMS attract the positive charges via the Au electrode (see Figure 2.5b). However, in COMSOL, the `floating potential` module is assigned to the Au and Al electrodes to evaluate the potential between the layers.

The graph in Figure 5.2b illustrates the membrane displacement, which exhibits a non-linear behaviour that is considered undesirable for a pressure sensor. This non-linearity affects the electric potential between the electrodes and consequently impacts the charge transfer through the external circuitry, resulting in a non-linear output signal [58]. Therefore, non-linear membrane displacement is considered an undesirable property, since the membrane displacement is proportional to the output signal [64]. In this context, membrane displacement refers to the overall movement of the membrane in the vertical direction, encompassing the entirety of the membrane rather than a specific position.

The linearity of data points from the simulation has been evaluated with the R^2 score by MATLAB and the results show a $R^2 \approx 0.66$, which is a very poor performance [81] (see Appendix B). However, the membrane shows sensitivity and reacts towards different pressure levels. The non-linear behaviour is influenced by the mechanical elasticity of PDMS and the limited distance between PDMS and Al. With the argument that, once the membrane makes contact with the Al layer, its displacement rate slows down. In other words, the membrane displacement does not increase proportionally to the applied pressure. This characteristic is clearly illustrated in Figure 5.2a. Notably, the change in membrane displacement is much smaller between $P = 40\,\text{mmHg}$ and $P = 70\,\text{mmHg}$ compared to between $P = 2\,\text{mmHg}$ and

$P = 15\,\text{mmHg}$, despite the former situation having an absolute pressure magnitude difference approximately twice as high as the latter.

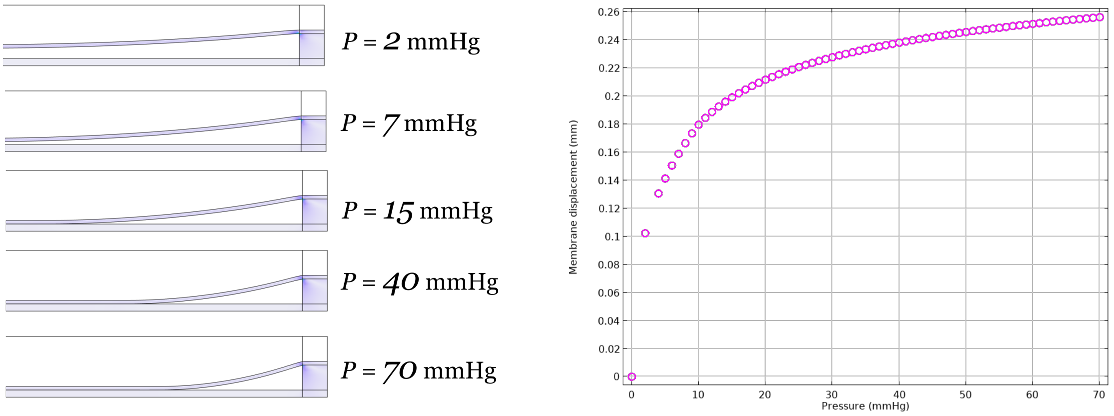

(a) *Membrane displacement versus different pressure level.*

(b) *Displacement behaviour of the membrane in response to applied pressure.*

Figure 5.2: *Deformation of the sensor's membrane by different pressure levels and the physical contact between the PDMS layer and Al (on the left side). The analytical graph illustrates the membrane displacement as the pressure increases (on the right side).*

5.2.1.2 Contact Surface Area Analysis: Results from the simulation show that, as the pressure increases on the top layer of the sensor the contact surface area starts to increase as well (see Figure 5.3). This analysis is important since the number of transferred charges on the surface is proportional to the contact surface area between the two tribes-layers [58]. The greater the contact surface area, the higher the amount of surface charges that accumulate due to the triboelectric effect. This argument can be further supported by equation (9) in Appendix A.

Figure 5.3a shows the contact surface area between the PDMS and Al layers. Even if the membrane reacts sensitively towards magnitudes as low as 2 mmHg, the contact between the tribo-layers does not take place until the pressure level reaches 10 mmHg. This indicates that the modelled sensing mechanism can transfer charges already within the normal range of ICP magnitudes *i.e.*, $7-15\,\text{mmHg}$ [17]. Based on this argument the modelled sensor retains the essential parameter, limit-of-detection, in order to detect ICP.

In Figure 5.3b the linear relationship between the pressure levels and the contact surface area has been evaluated with the help of the R^2 method. The results demonstrate a high linearity score of slightly $R^2 > 0.95$. However, Figure 5.3 reveals that the linearity diminishes as the pressure exceeds 40 mmHg. The linearity calculation for the contact surface area has neglected for pressure magnitudes below 10 mmHg, as contact surface area changes are primarily observed when the pressure magnitude exceeds this threshold.

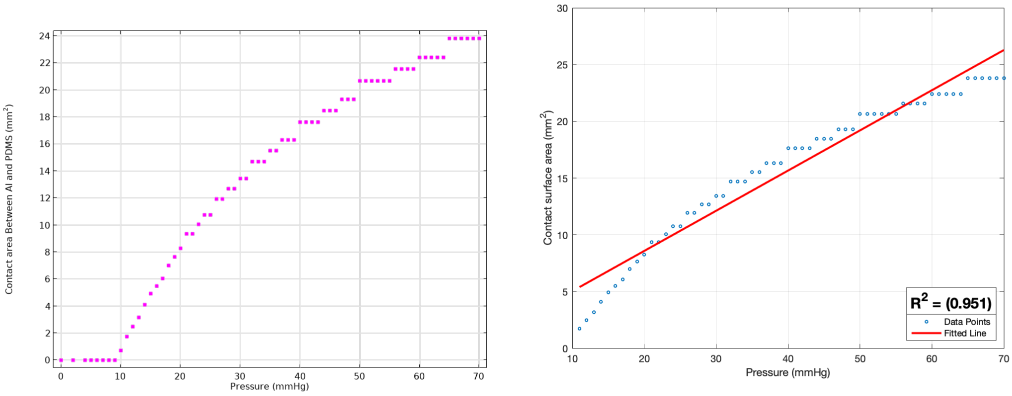

(a) *Surface contact area between PDMS and Al.* (b) *The linearity of surface contact area and pressure level.*

Figure 5.3: *The relationship between the applied pressure and the contacted surface area between PDMS and Al.*

The observations indicate that the modelled sensor exhibits optimal performance within a specific pressure range. The linear relationship between the contact surface area and applied pressure levels, as shown in Figure 5.3a, begins to deteriorate when the pressure exceeds 50 mmHg. In other words, the contact surface area remains relatively constant within the pressure range of 50−55 mmHg. However, the pressure range of TENG-based pressure sensors can be adjusted by various parameters [28, 74]. These parameters include the size of the sensor, the distance between the layers (spacer's height), the choice of different dielectric materials as tribo-pair, and the presence of nano- or micro-structures on the surface of the dielectric layer. Modifying these parameters can have an impact on the achievable pressure range. However, these modifications can also impact other parameters, for instance, limit-of-detection, sensitivity and even bio-compatibility [68]. The latter impact depends only on the material that would be selected for the fabrication of the sensor [8, 59].

5.2.1.3 Stress Analysis: Applying mechanical pressure on any material exposes the material to mechanical stress [84]. It is a logical approach to perform a stress evaluation on the components of the sensor's membrane. *i.e.*, PDMS and Au. When it comes to stress analysis of the material, it is required to be familiar with two important terms, the *yield strength* and the *tensile strength* of the material [100, 101]. The *yield strength* level: Shows the ability of a material to withstand a certain level of stress before plastically deformed (*permanently deformed*). *tensile strength*: Determines the resistance of a material to withstand a level of stress before tearing or breaking apart [101].

Figure 5.4 shows different stress levels that the PDMS layer is exposed to due to mechanical pressure applied from ICP. It is obvious that the most vulnerable areas to the stress, are at the surface boundaries where PDMS membrane attaches with the spacer. It is the point where the PDMS membrane bends the most once the pressure level increases. Figure 5.4a displays the stress level in the PDMS at maximum pressure magnitude *i.e.*, $P = 70\,\mathrm{mmHg}$. The colour legend on the right side of the figure indicates that the stress level in other parts of the sensor is around $0.1 - 0.4 \times 10^6\,\mathrm{N/m^2}$. However, for the PDMS layer it reaches up to $1.58 \times 10^6\,\mathrm{N/m^2}$ especially at the circumferences between the spacer and PDMS membrane, shown in the circular shape (zoomed version). Figure 5.4b illustrates the curve, how the stress level increases in the PDMS layer as the pressure magnitude approaches its maximum, curve in magenta colour. In contrast, the black-coloured dash-dot line declares the threshold of tensile stress for the PDMS. It is important to mention, that PDMS is highly elastic material and its *yield strength* is usually not reported by the litterateurs [100]. It is because the stress-strain curve of PDMS is linear until stresses over 2 MPa. However, with maximum pressure levels $1.58 \times 10^6\,\mathrm{N/m^2}$ stress is near to 2 MPa, which can be something that need to be considered for a long term application.

Observations indicate that the maximum stress level experienced by the PDMS layer does not cause it to tear or sustain damage. This is because the stress level in the material remains below its *tensile strength* threshold of $3.51 \times 10^6\,\mathrm{N/m^2}$ [100]. Simulation results further confirm that the stress level of the PDMS remains below its *tensile strength* limit (see Figure 5.4b), although it is not significantly distant from the threshold. Therefore, while there is not a substantial margin of safety to guarantee that the membrane will not tear, the simulation results indicate a low risk of tearing or damage. It is important to acknowledge that these simulations did not consider the uncertainty in dimensions. Specifically, the effect of stress on thinner or thicker membranes of PDMS was not simulated, which could have provided a more comprehensive understanding of the stress distribution. Including variations in membrane thickness in future simulations would offer a clearer insight into the impact of stress on the membrane.

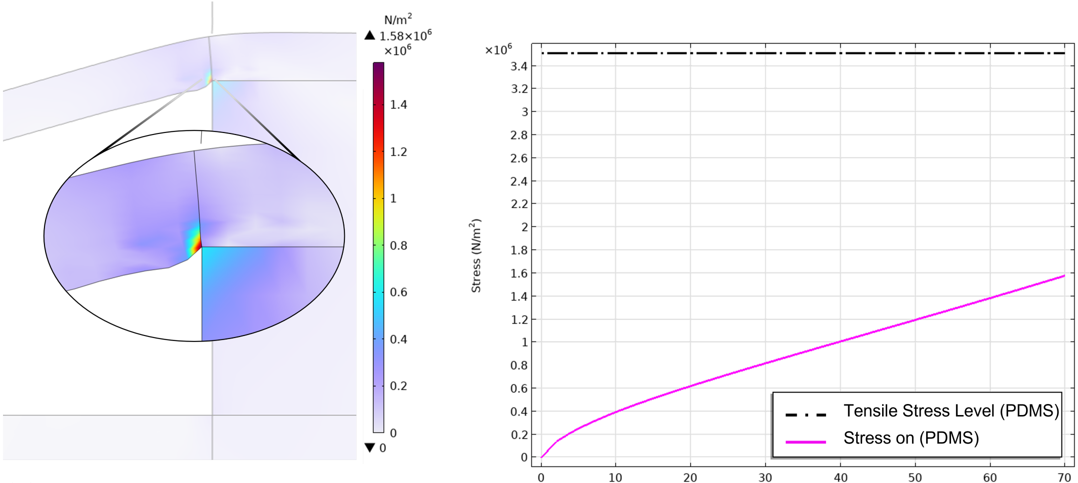

(a) *Most vulnerable area of PDMS layer while* $P = 70\,\text{mmHg}$.

(b) *Applied pressure versus stress in PDMS.*

Figure 5.4: *Stress level on the PDMS layer and other sensor parts with respect to the different pressure levels (on the left). Analytical graph of stress level on the PDMS layer and its tensile strength level (on the right).*

The stress levels from the applied pressure on Au layer is illustrated in Figure 5.5. The stress level increases in the middle of the Au layer when the pressure is between $P = 1-30\,\text{mmHg}$. However, the stress level gradually increases in the same areas as for the PDMS layer (see Figure 5.5a). In particular, the maximum stress takes place at the edge of the Au layer, where it bends the most when the pressure magnitude approaches its highest. This can be observed in the magnified part of Figure 5.5a where the pressure level reaches up to $P = 70\,\text{mmHg}$.

Figure 5.5b demonstrates the analytical curve of stress in Au as the pressure magnitude increases (magenta graph). The figure includes the level of *yield strength* for the Au nano-electrodes as a red-coloured (dash-dot) lines *i.e.*, $Au_{\text{yeild strength}} = 2 \times 10^9\,\text{N/m}^2$ [101]. The colour legend in Figure 5.5a and the curve in Figure

5.5b indicate that the maximum stress to which Au layer is exposed reaches $1.05 \times 10^9\,\mathrm{N/m^2}$. This argument indicates that with the maximum pressure level of $P = 70\,\mathrm{mmHg}$, there is a low risk that Au layer deform or break apart, as its *yield strength* is higher than the maximum stress applied.

It is important to note that these simulations did not account for the uncertainty in dimensions, including the effect of stress on thinner or thicker layers of Au. Considering these variations in layer thickness could have provided a more comprehensive understanding of the stress distribution within the material. Additionally, it should be acknowledged that continuous application of dynamic stress on a thin layer for an extended period can potentially lead to the formation of cracks or micro-fractures, which were not specifically addressed in these simulations [86, 101]. Appendix B shows a complete series of the membrane's behaviour toward different pressure magnitudes in 3D format.

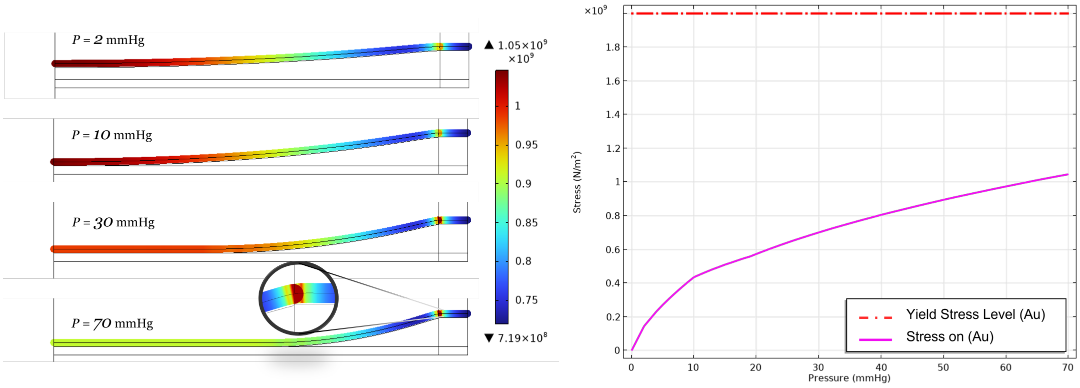

(a) *Stress level in Au layer under different pressure magnitudes.* (b) *Applied pressure versus stress level in Au.*

Figure 5.5: *Stress on the Au layer with respect to the different pressure levels(on the left). Analytical graph of stress level increment in the Au layer and its yield strength threshold (on the right).*

5.2.2 `Electrostatics` Analysis

Generating a charge difference between two materials with the help of the triboelectric effect causes an electrical potential difference between them, which results in the output voltage. `Electrostatics` interface from the COMSOL software has been used to evaluate the relationship between the membrane displacement and the potential variation generated between the layers. `Surface charge density` is used to declare the surface charge density value for the surface of PDMS, taken from Table II. `Potential floating` is used to declare the Al as the positive electrode, while the Au electrode has been assigned as `Ground` and to obtain the open circuit voltage V_{OC}, the differences in potentials between these two electrodes have been calculated by COMSOL simulations.

The maximum V_{OC} is reached when the tribo-pairs are separated after complete physical contact with each other and the potential between the layers decreases as the distance between them shrinks by the outside pressure [58, 66]. The maximum displacement of the membrane occurs once the pressure level reaches 70 mmHg and then the majority of the PDMS layer has come into contact with the Al layer. Pressure magnitudes $0 - 70\,\mathrm{mmHg}$ are applied as an input, with the help of `Solid Mechanics` interface on the sensor's membrane, which mimics magnitudes of ICP.

Simulations indicate that the maximum potential difference (voltage) between the electrodes reaches up to 121 V, while the negative voltage was as low as $-1.1\,\mathrm{V}$. These values are represented by the two ends of the colour bar shown in Figure 5.6. In Figure 5.6a, the open-circuit voltage and the potential difference between the electrodes are displayed, with a zoomed-in version inside the circle.

The open-circuit voltage (V_{OC}) calculated using equation (8) from Appendix A indicates that the simulated (V_{OC}) value is relatively close to the values obtained from analytical evaluations, as shown in the calculation below. It is important to note that the negative sign in front of the voltage (V_{OC}) arises from the PDMS surface charge density $\sigma_{PDMS} = -3.4\,\mu\mathrm{C/m^2}$. Furthermore, the permittivity of vacuum (ε_0) is assigned as $8.854 \times 10^{-12}\,\mathrm{C^2/Nm^2}$.

$$V_{OC} = \frac{\sigma_0 x(t)}{\varepsilon_0} = \frac{-3.4 \cdot 10^{-6} \cdot 350 \cdot 10^{-6}}{8.854 \cdot 10^{-12}} = -134.4\,\mathrm{V}$$

Figure 5.6b illustrates, how the electric potential between the layers changes and the voltage decreases as the pressure varies within the range of $0 - 70\,\mathrm{mmHg}$, causing the top layer to be pressed towards the Al layer. The decrease in the potential difference between the tribo-pairs when the layers come into contact confirms the underlying theory of triboelectric pressure sensors [58]. It also demonstrates that the designed TENG-based sensor is responsive to different pressure levels, resulting in variations in electric voltage between the electrodes.

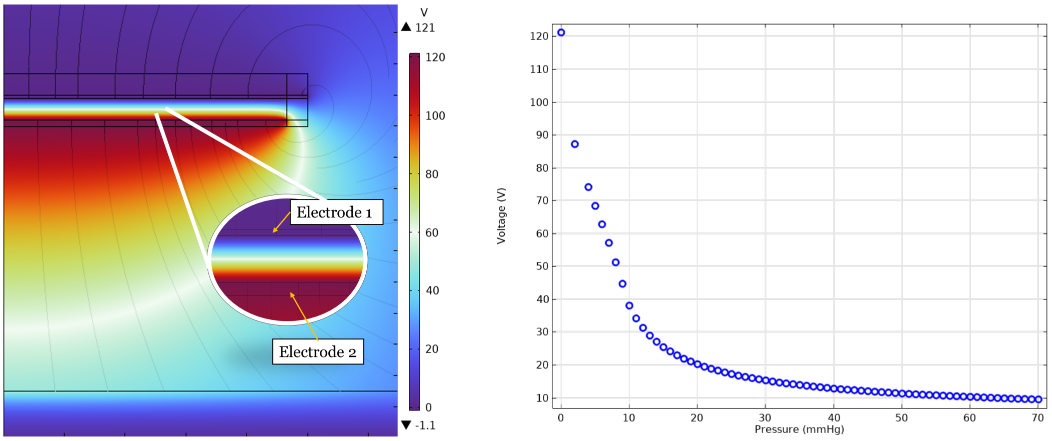

(a) *Potential distribution between the electrodes. ($P = 0\,\text{mmHg}$)*

(b) *Voltage decrement between the electrodes as pressure increases.*

Figure 5.6: *Electric potential between the PDMS membrane and Al layer (on the left). Output voltage decrement between the electrodes as the contact surface area between them increases (on the right).*

It is worth mentioning that despite the pressure level reaching its maximum, the potential difference between the layers did not approach zero, as depicted in Figure 5.6b. This phenomenon is primarily observed at the corners of the sensor, where there is a minor gap between the PDMS and Al layers, resulting in electrical potential difference, as shown in Figure 5.7a.

According to Figure 5.6b, the relationship between the voltage and the pressure levels shows a non-linear behaviour, which is an undesirable characteristic for the pressure sensors [1]. Calculations from MATLAB evaluated a linearity score for $R^2 \approx 0.52$ (see Figure 5.7). In addition, simulation results revealed that the designed sensor has two regions of sensitivity $\Delta V/\Delta P$ shown in Figure 5.8. The sensor acts more sensitively at the pressure region between $0 - 13\,\text{mmHg}$ *i.e.*, $-61.15\,\text{V/mmHg}$. While for the pressure range between $14 - 70\,\text{mmHg}$ the sensitivity decreases to approximately $-0.23\,\text{V/mmHg}$.

To obtain the electric potential on the Au electrode, the back of the Al electrode was selected as the reference ground (`Ground`). The results presented in Figure 5.9 illustrate that the maximum positive voltage reaches $10.8\,\text{V}$, while the maximum negative voltage on the Au electrode is $-115\,\text{V}$. A comparison between Figure 5.6a

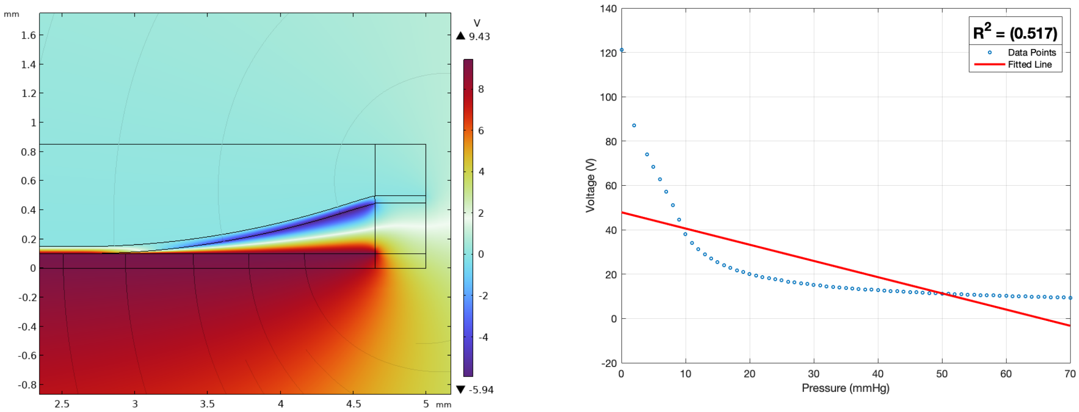

(a) *Edges that do not contact at maximum applied pressure i.e.,* $P = 70\,\text{mmHg}$.

(b) *Linear regression and the* R^2 *score for voltage variation with Au as* `Ground` *reference.*

Figure 5.7: *Edges of the sensor layers that do not contact each other despite the maximum pressure (on the left). Linearity of the electric voltage vs pressure data points evaluated by MATLAB (on the right).*

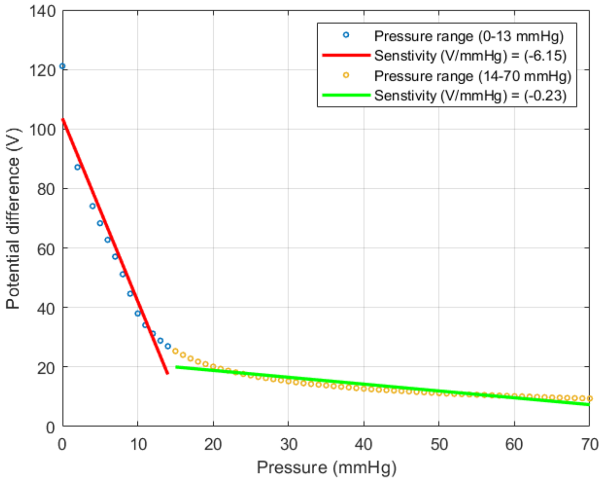

Figure 5.8: *Two different sensitivity regions of the sensor. Blue circles represent the data points for the pressure region between* $0-13\,\text{mmHg}$ *and its sensitivity (red line). Yellow circles represent the data points for the pressure region between* $14-70\,\text{mmHg}$ *and its sensitivity marked by the green line.*

and 5.9a reveals that the potential distribution is vertically mirrored.

Still, the colour bar in Figure 5.9a indicates higher maximum negative voltages compared to positive voltages. Additionally, when the Al electrode is grounded, the magnitudes of the positive voltages are lower than when the Au electrode is grounded. This difference can be attributed to the thickness of the PDMS layer, which contains negative charges, in contrast to the Al layer, which is twice as thick and contains positive charges.

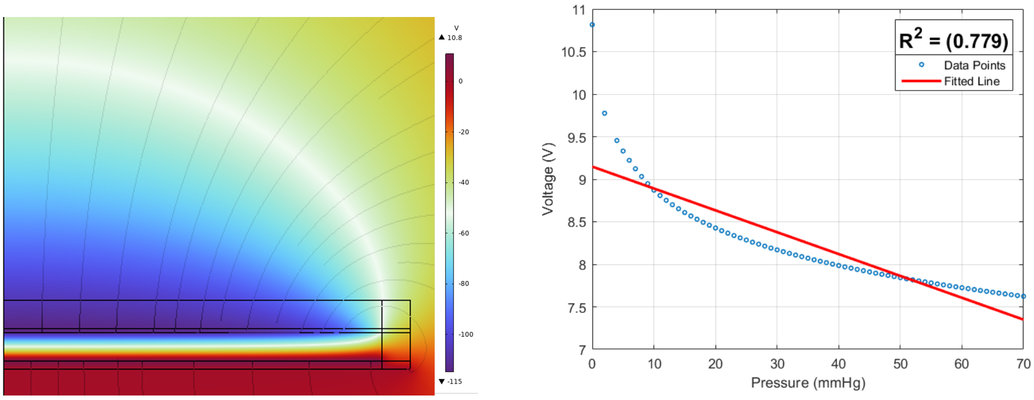

(a) *Electric potential at Au electrode in open circuit condition.* *($P = 0\,\text{mmHg}$)*

(b) *Linear regression and the R^2 score for electric voltage variation with Al as* `Ground` *reference.*

Figure 5.9: *Electric potential of Au layer with no pressure applied (open circuit voltage) (on the left). Voltage variation and its linearity (on the right).*

Another explanation for the dissimilarity between these two settings could be the difference in charge distribution on the surface of the electrodes. In the first attempt (with Au grounded), positive charges accumulate on the surface of the Al electrode, resulting in a very high positive potential difference between the layers. In the second attempt (with Al grounded), charges accumulate on the surface of the Au electrode, leading to a much lower positive potential difference between the layers. However, it is worth noting that the absolute value of the electrical potential between electrodes is approximately the same in both cases, around 122.1V and 125.8V, respectively (see calculations below).

- Au grounded: $121 + |-1.1| = 122.1$
- Al grounded: $10.8 + |-115| = 125.8$

Furthermore, the relationship between voltage decrement and applied pressure is illustrated in the curve graph in Figure 5.9b. When choosing the Al electrode as reference `Ground` we obtained better linearity and a score of $R^2 \approx 0.78$ compared to the former simulation (shown in Figure 5.7). The linear behaviour observed in Figure 5.7 (with Au grounded) appears to have a larger voltage range than that observed in Figure 5.9b (with Al grounded). This can be one reason that the linearity of the latter setting is better than the former.

5.2.3 Extended Spacer Size

To assess the impact of the distance between the tribo-pairs on the sensor's behaviour, the height of the spacer was varied from 350 µm to 500 µm. The results obtained from both the `Solid Mechanics` and `Electrostatics` modules are evaluated as follows.

5.2.3.1 `Solid Mechanics` Analysis with Extended Spacer Size: Figure 5.10 was obtained from the `Solid Mechanics` interface, illustrating the behaviour of the membrane under applied pressure and the stress level on the Au membrane. The graph of membrane displacement, shown in Figure 5.10a, exhibits improved linearity with respect to applied pressure levels. Additionally, the $R^2 \approx 0.8$ value is closer to 1 compared to the $R^2 \approx 0.6$ obtained in the previous simulation.

Figure 5.10b illustrates that the stress on the Au layer slightly increased from 1.05×10^9 N/m^2 to 1.35×10^9 N/m^2 as the height of the spacer extended from 350 µm to 500 µm. This value remains below the *yield strength* of Au, indicating a low risk of the stress causing plastic deformation in the Au layer. However, the margin between the *yield strength* threshold and the maximum stress in the material is even smaller than in the former case, which must be taken into account. Surprisingly, the stress level on the PDMS layer did not show significant changes, which may be attributed to its elastic behaviour [84].

5.2.3.2 `Electrostatics` Analysis with Extended Spacer Size: The sensor with a spacer height of 500 µm exhibited distinct results in the `Electrostatics` interface as well (see Figure 5.11). Figure 5.11a illustrates the relationship between the variation in electric potential and the contact surface area between the PDMS and Al layers, relative to the applied pressure levels.

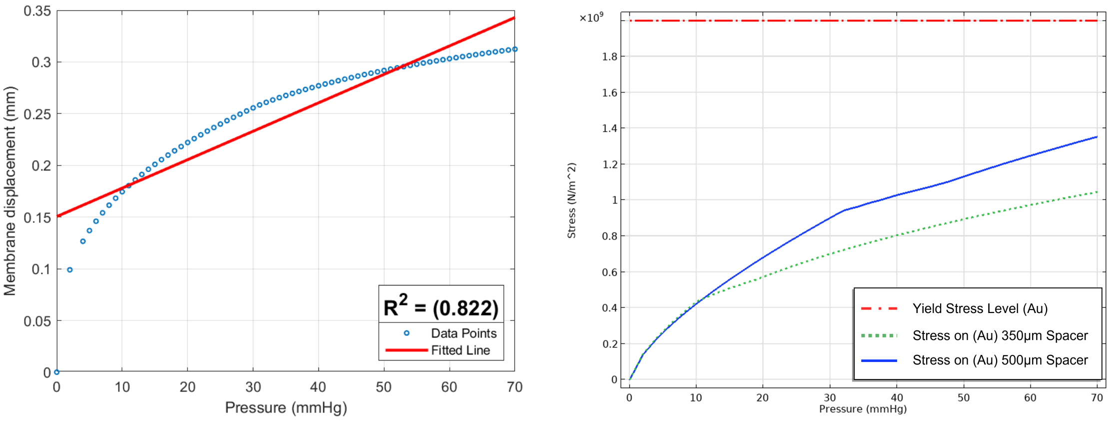

(a) *Membrane displacement and its linearity, spacer height* 500 µm.

(b) *Stress level on the Au layer for spacer height of* 350 µm *and* 500 µm *respectively.*

Figure 5.10: *Membrane displacement and its linearity of the sensor with a* 500 µm *spacer and* $P = 0 - 70$ mmHg *(on the left). Stress level on the Au layer of the sensor and its comparison with the former simulation results from the sensor with* 350 µm *spacer (on the right).*

Extending the spacer height resulted in a more linear relationship between the potential variation and applied pressure levels, compared to the previous results shown in Figure 5.6b. Furthermore, the linearity score depicted in Figure 5.11b increased to approximately $R \approx 0.9$. This represents a significant improvement compared to the linearity exhibited by the sensor with a 350 µm distance between the tribo-layers (see Figure 5.7b).

The blue circles in Figure 5.11a demonstrate that the magnitude of the maximum electric potential is greater than the values obtained in Figure 5.6b, specifically $169\,\text{V} > 121\,\text{V}$. Consequently, at a pressure level of $P = 70$ mmHg, the electric potential difference does not decrease below 20 V. A rough analytical calculation confirms that increasing the distance between layers by approximately 40% (from 350 µm to 500 µm) results in a corresponding increase of about 40% in the electric potential difference, from 121 V to 169 V.

However, the contact surface area between the PDMS and Al has decreased significantly compared to the results shown in Figure 5.3a, specifically from $24\,\text{mm}^2$ to $9\,\text{mm}^2$, even at $P = 70$ mmHg. Furthermore, observations from Figure 5.11a reveal that there was no contact between the PDMS and Al layers until the pressure level reached 30 mmHg. This indicates a poor limit of detection, meaning that in real-world applications, triboelectric sensors with these dimensions will not generate any electrical signal for pressure levels lower than 30 mmHg. This limitation disqualifies the sensor from effectively monitoring the ICP, since an ICP level over 20 mmHg is considered critical, it is essential for the sensor to generate an electrical output signal within the normal ICP range (7 – 15 mmHg) in order to detect critical ICP magnitudes.

It is important to note that in real-world applications, the accumulation of charges on the surface of the tribo-pair and the resulting electric potential between the layers only occur when physical contact is established [60]. However, in the COMSOL simulations, the electric potential is already established due to the inclusion of the `Surface Charge Density` module. This means that the electric potential between the layers exists even in the absence of contact between them earlier (according to COMSOL). It is important to acknowledge that this property deviates from the actual fundamentals of the triboelectric principles.

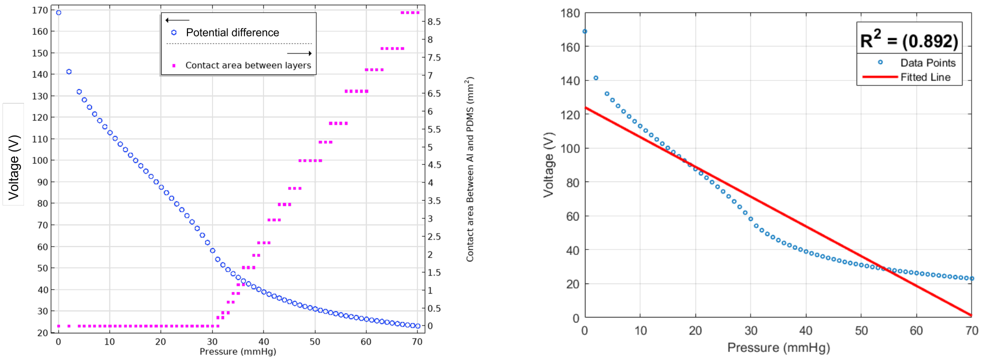

(a) *Electric potential difference and contact surface area between layers.*

(b) *Electric voltage variation and its linearity.*

Figure 5.11: *Effect of spacer's height extension on surface contact area and electric potential difference between PDMS & Al layers of the sensor (on the left). The evaluation of linear behaviour of the voltage variation cause by different pressure levels in the sensor (on the right).* (500 µm *spacer height)*

5.3 Test Rig Setup

This section has been divided into two parts. The first part discusses the results taken from the manufacturing process of the brain phantom, along with the risks and obstacles that the project has faced and conquered. The second part discusses the setup of instruments and the process of pressurising the brain phantom.

5.3.1 Brain Phantom Manufacturing Results

The manufactured prototypes of the brain phantom in this study have shown mechanical elasticity due to small pressure magnitudes applied from outside (pressed between two fingers). The capillary tubing, installed at both sides of the ventricle void, enabled to have a flow of pressurised liquid inside the brain phantom. However, there were challenges and risks that have been identified. For instance, mixing the two silicone components (base and catalyst) could introduce air bubbles. Air bubbles usually appeared on the flat surfaces of the cylindrical halves which made the structure vulnerable to pinholes. These pinholes allowed pressure to leak from the ventricle void.

To overcome the challenge of air bubbles on the flattened surface of the half cylinder, casting in a vacuum chamber has been suggested as a solution to eliminate the air bubbles. However, the process led to a deformation of the moulded brain phantom, since the air bubbles could not escape the silicone cast. This is due to the high viscosity of the silicone mixture and the cross-linking (hardening) process already started while air bubbles were on their way out, which deformed the flattened side of the half-cylinder.

In addition, the application of *POP* primer to the flattened surface of silicone and the capillary tubes, along with bonding them using glue, affected the elasticity of the material. Specifically, the areas treated with primer and glued exhibited brittle and hard properties once the glue dried out, altering the mechanical elasticity of the silicone rubber. Moreover, the brittleness introduced by the glue made the structure more susceptible to breakage and tearing when transferring pressurised fluid into the ventricles.

Further, the blockages of the capillary tubing were another risk induced by *POP* primer and adhesive glue. In order to ensure a tight seal between the tubes and the silicone body, caution must be exercised when applying primer and glue to avoid unintentionally blocking the capillary canal. Once the two halves were assembled together there was limited access inside the ventricle to eliminate the blockage.

In order to overcome the above-mentioned obstacles, and eliminate the risk of brittleness and tubing blockage caused by the glue, a new mould has been 3D-printed. This mould is designed to reduce the number of surfaces which need to be bonded or assembled using primer or glue. The *3rd-generation* mould contained two major parts, (see Figure 5.12).

- **Brain phantom body:** A complete cylindrical shape with the ventricle void and cast tube.
- **Ventricle lid/cork:** A ”V” shaped cork, is cast with its capillary tube, which seals the ventricle void.

The 3D-printed mould was specifically designed to facilitate casting of the capillary tubes into the void of the ventricles during the moulding process of the brain phantom (see Figure 5.12a). Similarly, in order to assemble the different parts of the brain phantom (cork and body), a silicone mixture was used as a bonding material instead of using primer and glue. The intention was to minimise the number of surfaces that required glueing. After the casting process for both parts was completed, the silicone mixture was applied to their surfaces to ensure proper bonding.

In Figure 5.12b dashed oranges lines represent the surfaces where the silicone mixture is applied as a bonding material, while the primer and glue were applied only to the corners of the tubes.

Results from the *3rd-generation* 3D-printed mould showed better elasticity, less susceptibility for pinholes, and fewer surfaces to glue than the former design. A small amount of primer and glue has been used at the circumferences of tubes, where it meets the silicone rubber. Because the tubes are made of polytetrafluoroethylene (PTFE) according to its datasheet from manufacturer [102]. It was not possible to completely bond them only by silicone mixture while casting. That is why a small amount of bonding primer and glue was necessary. Still, the system could maintain its elasticity with a leak-proof ability. The difference between the brain phantom (1st and 2nd generation brain phantom) assembled with the *cyanoacrylate* glue and the ”3rd generation” brain phantom assembled with silicone solution can be seen in Figure 5.13.

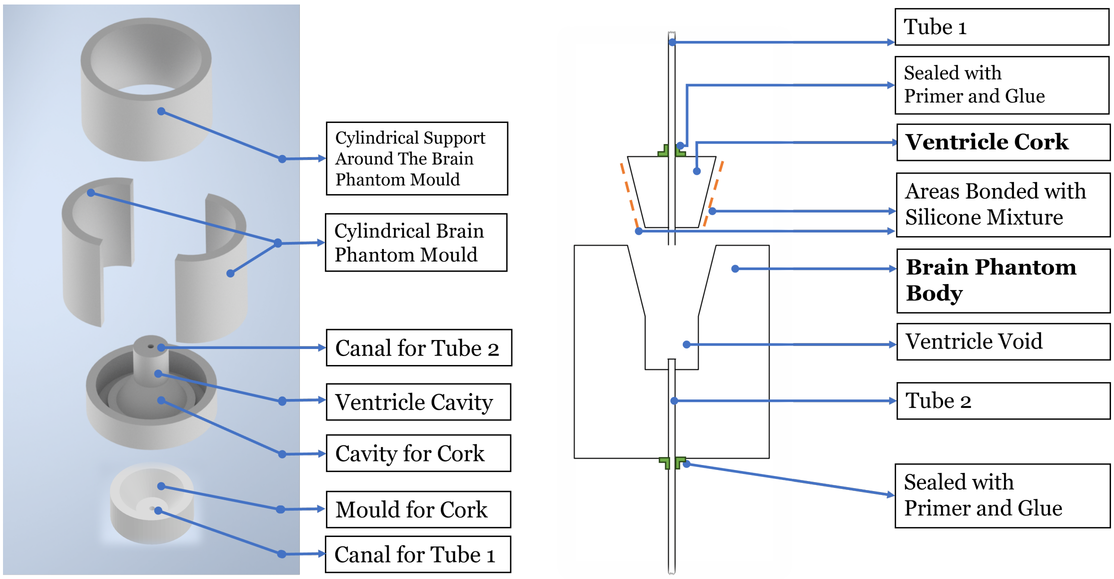

(a) *Complete cylindrical brain phantom mould.*

(b) *Cross-section of the 3rd-generation brain phantom and its two major parts.*

Figure 5.12: *The mould for complete cylindrical brain phantom and its cork (on the left side). The cross-section of moulded brain phantom (on the right side).*

(a) *1st & 2nd Gen. Brain phantom assembled with glue.*

(b) *3rd Gen. Brain phantom assembled with silicone.*

Figure 5.13: *1st & 2nd generation brain phantom, assembled the two halves of a cylinder with the POP and glue (cyanoacrylate) (on the left). The 3rd generation brain phantom is assembled with the silicone itself after casting (on the right).*

5.3.2 Experimental Process & Findings

Figure 3.3 provides an overview image of the experimental setup and instrumentation already in section 3. The experiments below have been performed under two circumstances: First, where *Tube 2* ”ventricle’s output” was intentionally blocked by the ON/OFF switch and pressure could only flow and oscillate from one direction into the ventricle *i.e.*, via *Tube 1*. Second, where the switch for *Tube 2* ”ventricle’s output” was open and the pressurised liquid could flow through the ventricle’s void and dropping inside the beaker (see right side of the setup in Figure 3.3). However, the results did not show any significant difference.

The brain phantom of the *3rd generation* was pressurised using oscillating pressure levels. Specifically, an oscillating pressure with an amplitude ranging from 0 to 50 mbar was applied, along with an offset value of 50 mbar. The oscillation was performed at frequencies of 0.2 Hz and 1 Hz. The results obtained from the OXygen software are presented as graphs in Figure 5.14. The pressurised liquid from the reservoir could flow throw the ventricles without any leakage successfully. However, in the pressurising process, the system did not react as expected. In particular, the pressure variation was not detectable on the surface of the brain phantom as pulsation. Furthermore, the incline pressure sensor (IPS) did not detect the expected pressure variations as depicted in Figure 5.14a. It is evident from the figure that there is a noticeable delay between the input pressure (red curve) and the monitored pressure by the IPS (green curve). Similarly, the pressure magnitudes measured by the IPS are approximately 25 times lower than the actual input pressure before the ventricles of the brain phantom.

Applied pressures with frequency of 1 Hz are displayed in Figure 5.14b. These variations are not detectable at all by IPS (see green curve in the figure). Likewise, no pulsation was detected by the eye observation and physical touch of the surface of the brain phantom. This indicates that the pressure variation inside the ventricle of the brain phantom does not behave as expected.

To test the limits of the brain phantom and the behaviour of IPS, an oscillating pressure magnitude with exaggerated amplitude has been applied as input pressure. The oscillation was at a frequency of 0.2 Hz, an amplitude of 200 mbar and offset over zero with value of 50 mbar. Graphical results gained from this test is depicted

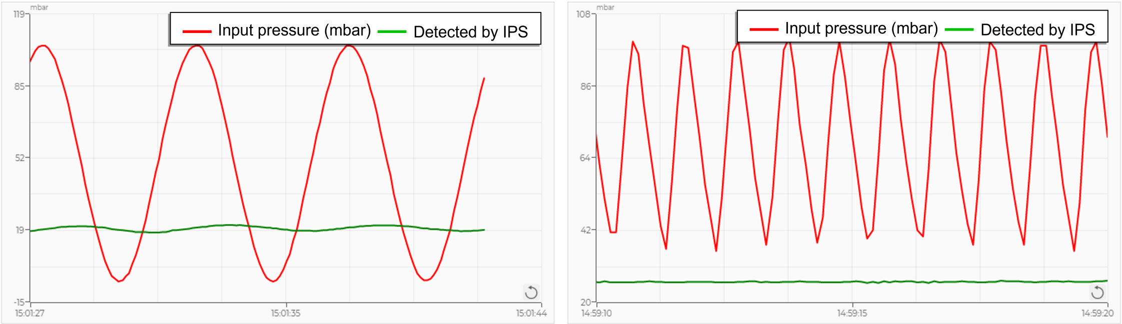

(a) 50 mbar *pressure with* 0.2 Hz

(b) 50 mbar *pressure with* 1 Hz

Figure 5.14: *Oscillation of the applied pressure, from the regulator (red curve) and pressure variation monitored by incline-pressure sensor after the brain phantom (green curve).*

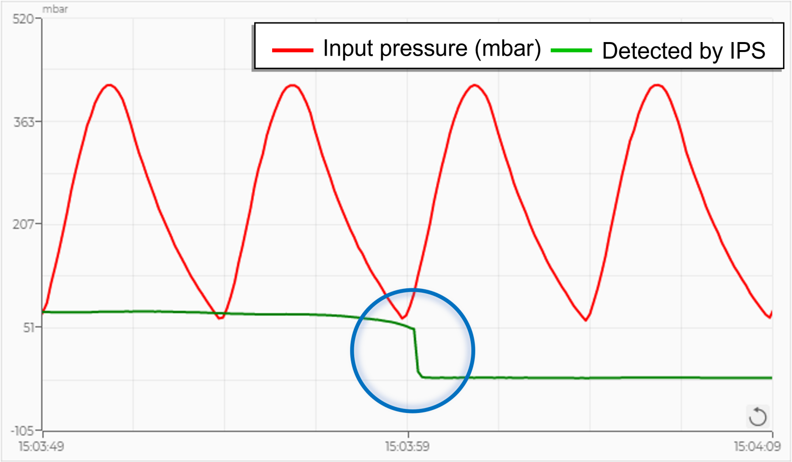

Figure 5.15: 200 mbar *pressure with* 0.5 Hz *frequency applied as test. The blue circle shows the pressure drop from the IPS sensor just after the brain phantom's fracture.*

in Figure 5.15. The test did not show any indication of pulsation in the brain phantom nor detectable amplitude variations by the IPS curve. However, the brain phantom started to expand slightly due to its elasticity and fractured where the cork was assembled. The rapture of the brain phantom entailed a lower pressure in the ventricle which was detected by the IPS and marked as a blue circle in Figure 5.15.

6

Discussion

This chapter will go through the key aspect of the master thesis, initiated with the results from the literature study in Section 6.1 which discusses the key parameters and requirements of pressure sensors for intracranial pressure (ICP) monitoring and continues with an exploration of results gathered from the COMSOL simulations in Section 6.2, where the quality and limitations of the simulated sensor will be evaluated. In Section 3.2 the work process of the experiment, results and error sources from the test bench setup will be discussed. The results obtained from this study provide insight into the feasibility and potential of the triboelectric nano-generator (TENG) based pressure sensors in the field of ICP monitoring. This chapter ends with Section 6.4 which identifies the areas that require further investigation in this field.

6.1 Literature Study

The literature study provided an overview of the available sensing mechanisms for ICP, along with their advantages and disadvantages. The attributes that TENG-based sensors have shown in previous studies as biosensors look promising for exploring their potential application in measuring ICP. For instance, essential requirements include a pressure sensing mechanism capable of measuring the required pressure range, operating in a self-powered manner, demonstrating mechanical flexibility, and being bio-compatible and durable.

Conventional ICP sensors based on piezoresistive or capacitive technology require an external power supply for long-term implantable sensors. They are limited by insufficient long-term durability and environmental vulnerability. Similarly, self-powered piezoelectric pressure sensors are limited by humidity intolerance and signal interference from vibrations, affecting their accuracy.

This is the first study assessing the potential of a TENG-based sensing mechanism for monitoring ICP. Previous researchers have only applied TENG-based sensors for blood pressure measurements or wearable tactile (pulse) sensors. This novelty in exploring new territory within the field adds to the significance of this thesis. Table VI presents a categorisation and comparison of each sensor technology, based on the literature study, using a simple methodology and assigning them scores.

However, the evaluation in Table VI provides a generalised assessment of sensor features. These features are not specific to the sensor designed in this study. For instance, there has been no research explicitly evaluating the drift or calibration issues of TENG-based sensors. Nevertheless, developed TENG-based sensors manufactured from polytetrafluoroethylene (PTFE) and aluminium (Al) have shown signal stability even after 10^8 cycles. It is worth mentioning that the chemical and physical properties of the dielectric material have an impact on such sensor features [58, 60, 103]. Simulations performed in this study did not include such chemical changes and their impact on the behaviour of the sensor, which is a critical aspect that must be taken into account. Similarly, the durability and the effect of a bio-compatible encapsulation on the designed sensor remains unanswered. Moreover, developed TENG-based pressure sensors have not reported the detection of negative pressure magnitudes which introduces a notable limitation to this technology. Ultimately, the data assembled in this study provides an overview of the pros and cons of different pressure sensors, along with the essential attributes for ICP monitoring.

6.2 Simulations

Results gathered from the simulations show that the membrane made from polydimethylsiloxane (PDMS) attached with nano-layer of gold (Au) could react in the form of *membrane displacement* under the applied pressure from ICP. The membrane was responsive toward the ICP pressure range $0 - 70\,\text{mmHg}$ with a resolution as low as $1\,\text{mmHg}$. Results indicated that the displacement was not proportional to the pressure change. In particular, the linearity of the membrane's displacement did not perform according to requirements.

However, the results obtained after extending the spacer height showed improved linearity in both the `Solid Mechanics` and `Electrostatics` analysis. However, it negatively affected the limit of detection, increasing it from $10\,\text{mmHg}$ to $30\,\text{mmHg}$, which is undesirable. There are several other factors that can influence the linearity of the sensor. These include the diameter size of the sensor, the thickness of the dielectric, the elasticity characteristics of the PDMS layer, and the stiffness of the Au layer. Due to time constraints, this project was unable to simulate and compare all these parameters.

Pressure levels as low as 10 mmHg could bring the PDMS membrane in contact with the Al layer. Hence, the simulated sensor accumulated electrical charges according to its fundamental principles. This ability to transfer charges already in 10 mmHg qualifies their limit-of-detection for sensing ICP. From the linearity perspective, the surface contact area showed better linearity with respect to different pressure levels in comparison to the results from the membrane's displacement. It could obtain an R^2 value near 1 which is desirable. It is important to realise that the linearity tends to decrease once the pressure level increases over 40 mmHg. However, an ICP magnitude greater than 20 mmHg is a critical situation for the patient. More specifically, if the designed sensor can generate charges linearly with applied pressure in the margin of $1 - 40$ mmHg it can be usable data to save the patient, with the reason that 40 mmHg is higher than the ICP critical magnitudes.

Both PDMS and Al have shown moderate stress resistance caused by the applied pressure levels. This indicates that PDMS can be an appropriate dielectric material to be used in manufacturing TENG-based sensors for monitoring ICP. However, data about the PDMS *yield strength* is not reported and Young's modulus for PDMS varies between 800 kPa to 2.6 MPa [100]. This means that PDMS used in this design have been specified with its Young's modulus over 2 MPa. Likewise, bulk gold has a *yield strength* around 900 $\mathrm{kN/m^2}$ [86] but studies have developed nano-wires specific for electrodes that have a *yield strength* up to $2 \times 10^9\,\mathrm{N/m^2}$. Even if Au is a metal which is available in nature but with this specific *yield strength* it can be difficult to access or even costly to manufacture.

Simulation results from the `Electrostatics` module verified that mechanical pressure can modulate the potential between the electrodes. Obtained results indicated an open-circuit voltage around 121 V. None of the previous studies has simulated TENG-based pressure sensors for such low-pressure magnitudes as ICP nor with these small dimensions [64, 103, 104]. Likewise, former studies mostly simulated TENG as an energy harvesting generator rather than a pressure sensor. The modelled sensor in this study is a very simplified version. For instance, no encapsulation layer has been included in the simulations. Also, pressure levels were directly applied on the surface of the Au layer and how the sensor would react against pressures from actual brain tissue has not been simulated.

In real-world applications, the amount of charges accumulated on the surface of tribo-pairs occurs due to physical contact. While in COMSOL simulations those amounts have been added manually in `surface charge density` and `potential floating` modules, TENG is a new technology and COMSOL software has not developed a built-in multi-physics like mechanics, piezoelectric, capacitive and piezoresistive modules. A multi-physics interface that could cover all boundary conditions, and fundamental physics for TENG automatically, could provide better results which are closer to real-world applications.

The values for the open-circuit voltage (V_{OC}) obtained from the `Electrostatics` interface closely align with the (V_{OC}) values calculated by the mathematical model presented in equation (8) from Appendix A. However, it is worth noting that the obtained values appear higher compared to the sensors designed in previous studies [28, 64, 105] that had mostly the same specifications as the one designed in this study. This discrepancy can be attributed to the high surface charge density value implemented in the simulation of this study. Meanwhile, it demonstrated poor linearity between the applied pressure levels and the sensor's output voltage variation. The results provide an overview of how the TENG-based sensor designed in this study would behave with respect to pressure magnitudes. However, the magnitude of the output signal differs from the real world.

It is important to acknowledge that simulations cannot fully capture real-world complexities and dynamics, such as the effect of vibrations on the sensor. Additionally, certain surface treatments like *inductive coupling plasma* treatment or corona discharge treatment may be challenging to replicate accurately within a simulation environment. From an ethical perspective, it is very difficult to evaluate the safety of the designed sensor based on the simulation results too. It is also challenging to evaluate the selectivity in the output signal from the designed sensor just by results from the simulations. Since the influence of noise, temperature and signal from other devices on the sensor's output signal is challenging to perform in a simulation module.

Moreover, this investigation highlights the impact of various parameters on the pressure range, sensitivity, linearity, durability and environmental robustness. Factors such as sensor size, choice of materials for the tribo-pair and the existence of nano- or micro-structures on the dielectric layer surface can impact the required attributes.

6.3 Test Rig Setup

Results from the manufacturing process of the brain phantom showed that the intrusion of air bubbles in the silicone mixture happens easily and applying glue affects the mechanical properties of the brain phantom. Furthermore, having two halves of a symmetric shape increases the surface area that needs to be glued. Likewise, the risk of pressure leakage from the pinhole caused by air bubbles increases. Casting a pressure-tight ventricle void inside the brain phantom was the major obstacle. However, this obstacle can be overcome by reducing the surface area that needs to be glued by adhesive material and primer *POP*. Meanwhile using a silicone mixture instead of glue to assemble the parts showed more efficiency and retained elasticity.

The brain phantom manufactured in this study was a simplified imitation of the actual brain. In comparison with former studies in this field, the phantom brain could only mimic the elasticity of the brain tissue and it was based on the mechanical properties of the silicone rubber. One possible reason why the brain phantom did not exhibit any mechanical displacement, despite having a pressure-tight ventricle and applying high-pressure levels, could be attributed to a lack of understanding regarding the underlying mechanisms of pressure variation within the ventricle, and the difference between the elasticity of the actual brain tissue and the silicone used as brain phantom *i.e.*, 2.9 kPa and 4.6 kPa respectively. Another possible reason why the pressure did not cause mechanical pulsation in the brain phantom could be the distance between the ventricle void and the surface. In other words, the ventricle should have been larger to observe such pulsations. Additionally, a potential reason could be a limited understanding of the fundamental principles governing fluid pressure dynamics, which requires more time to fully comprehend the theory and its mechanisms. The absence of curvature in the brain phantom, along with other simplifications, could be another reason for the lack of pulsation. Curvature plays a crucial role in allowing the structure to bend or deform more easily, as opposed to a flat and uniform shape like a cylinder. By neglecting curvature, the brain phantom loses the natural variations and complexities that are present in real brain tissue, which may affect its ability to exhibit pulsation.

However, the major obstacle of having a pressure-tight ventricle and reducing the application of glue has been overcome successfully by this study. The same methodology can be utilised for future experiments in the field of phantom brain test rigs.

6.4 Future Outlook

This paper can serve as an initial step towards exploring the potential of triboelectric sensors for implantable ICP monitoring. It provides a foundation for further investigation in this field. In order to obtain reliable results and enhance the performance of self-powered pressure sensors based on TENG for ICP monitoring, the following areas are recommended for future exploration.

The primary area to investigate is the influence of materials on the performance of TENG-based pressure sensors for monitoring ICP. Given the wide range of materials available for triboelectric sensors, it is worthwhile to explore which material combinations as tribo-pairs can fulfil the necessary requirements for an ICP sensor. Furthermore, exploring alternative configurations of TENG-based sensors for ICP monitoring, such as single electrode configuration, could yield valuable insights.

The secondary domain worth exploring includes the impact of a bio-compatible encapsulation layer on the sensor's vital characteristics. Additionally, investigation of the capability of TENG-based pressure sensors to detect negative relative pressure magnitudes. Moreover, the issue of calibration and drift in TENG-based pressure sensors remains an unexplored territory.

The tertiary area that needs to be investigated, is a simulation module or specific interface which could cover fundamental principles of triboelectric technology, in consideration to provide more accurate and realistic results. Also, in the aspect of circuit integration, it is valuable to explore the opportunities for integration of TENG-based pressure sensors with wireless and real-time transmitters, while fulfilling the requirements of minimal size and robust encapsulation.

When considering the fabrication of a brain phantom for a test rig, it is important to investigate the manufacturing process of a brain phantom that accurately represents the fundamentals of fluid pressure dynamics. Specifically, the research should focus on developing a brain phantom that minimises pressure loss within the ventricle when pressurised via external tubes. This will ensure a more realistic simulation of fluid pressure dynamics within the brain phantom.

These proposals to be investigated in the field of TENG-based pressure sensors for monitoring ICP can further promote and contribute to improved diagnosis, treatment, and management of neurological conditions.

7

Conclusion

In the pursuit of a self-powered intracranial pressure (ICP) sensor, this is the first study that has explored the potential of triboelectric nano-generator (TENG)-based pressure sensors for surveillance of ICP. Moreover, this study has constructed a simplified test rig for brain phantom examination.

The designed sensor based on triboelectric technology, proposes several advantages over conventional ICP transducers, such as power-supply independency, mechanical flexibility, simplified fabrication and bio-capability for long-term implantation.

Through the literature study and COMSOL simulations, the performance of a TENG-based pressure sensor has been evaluated. The obtained results verify the sensor's ability to accurately detect and quantify variations in ICP within the desired pressure range. The sensor's membrane showed desirable responsiveness toward the applied pressure level, indicating its suitability for the future monitoring of ICP.

However, it should be noted that there are still areas for further improvement and research. A proper simulation module, specified for TENG-sensors that allow demonstration of more realistic scenarios, the sensor's long-term stability, and extended durability testing *in vivo*. Additionally, research into alternative material combinations or sensor configurations, the impact of different geometries, and encapsulation techniques for the sensor can help to optimise the performance of these sensors, while addressing specific requirements for clinical applications.

In general, this thesis initiates the foundation for developing and applying TENG-based pressure sensors for ICP monitoring. The findings provide advancement of less invasive and self-powered sensing technologies in neurology and healthcare. Further investigation and improvements are encouraged to enhance the performance, reliability and integration into clinical practice of the sensor.

References

[1] L. Yu, B. J. Kim, and E. Meng. “Chronically implanted pressure sensors: challenges and state of the field”. In: *Sensors (Basel)* 14.11 (Nov. 2014), pp. 20620–20644. ISSN: 1424-8220. DOI: `https://doi.org/10.3390/s141120620`.

[2] K. B. Evensen and P. K. Eide. “Measuring intracranial pressure by invasive, less invasive or non-invasive means: limitations and avenues for improvement.” In: *Fluids and Barriers of the CNS volume.* 17.34 (May 2020). DOI: `https://doi.org/10.1186/s12987-020-00195-3`.

[3] N. Canac et al. “Review: Pathophysiology of intracranial hypertension and noninvasive intracranial pressure monitoring”. In: *Fluids Barriers CNS* 17.40 (June 2020). DOI: `https://doi.org/10.1186/s12987-020-00201-8`.

[4] K. W. in collaboration with the Child and F. I. Group. ”External ventricular drainage”. *NHS.* 2019. [Online].Available: `https://media.gosh.nhs.uk/documents/External_ventricular_drainage_F0778_FINAL_Sep19.pdf`. (Accessed:2023-03-30).

[5] M. Czosnyka and J. D. Pickard. “Monitoring and interpretation of intracranial pressure.” In: *Neuroscience for neurologists.* 75.6 (Jan. 2004), pp. 813–821. DOI: `https://doi.org/10.1136/jnnp.2003.033126`.

[6] P. K. Eide and A. Bakken. “The baseline pressure of intracranial pressure (ICP) sensors can be altered by electrostatic discharges.” In: *BioMed Eng OnLine* 10.75 (Aug. 2011). DOI: `https://doi.org/10.1186/1475-925X-10-75`.

[7] Q. Wei et al. “Wireless Passive Intracranial Pressure Sensor Based on a Microfabricated Flexible Capacitor”. In: *IEEE journal* 65.6 (June 2018). DOI: `https://doi.org/10.1109/TED.2018.2825247`.

[8] J. Anderson. “9.19 - Biocompatibility.” In: *Polymer Science: A Comprehensive Reference.* 9 (June 2012), pp. 363–383. DOI: `https://doi.org/10.1016/B978-0-444-53349-4.00229-6`.

[9] J. M. Das and C. A. Mount. *Cerebral Perfusion Pressure.* Ed. by StatPearls. Internet. Treasure Island (FL): StatPerals Publishing, 2023. [Online].Available: `https://www.ncbi.nlm.nih.gov/books/NBK537271`. (Accessed:2023-04-11).

[10] D. DeMers and D. Wachs. *Physiology, Mean Arterial Pressure.* Ed. by StatPearls. Internet. Treasure Island (FL): StatPerals Publishing, 2022. [Online].Available: `https://www.ncbi.nlm.nih.gov/books/NBK537271`. (Accessed:2023-04-11).

[11] J. Oertel and S. Antes. “Intracranial Pressure Monitoring”. In: *Pediatric Hydrocephalus*. Ed. by G. Cinalli, M. M. Ozek, and C. Sainte-Rose. Cham: Springer International Publishing, 2018, pp. 1–27. ISBN: 978-3-319-31889-9. DOI: `https://doi.org/10.1007/978-3-319-31889-9_71-1`.

[12] A. Tameem. “Cerebral physiology.” In: *Continuing Education in Anaesthesia Critical Care & Pain* 13.4 (Aug. 2013), pp. 113–118. DOI: `https://doi.org/10.1093/bjaceaccp/mkt001`.

[13] D. Frahmand. (Neurosurgeon) Interviewee, and S. Afshar, C.E. Dahlberg (Msc. students) Interviewer. *Weekly meetings at Chalmers university*: Gothenbug, Sweden. 2023-02-15.

[14] Y. Honjol et al. “Current view and prospect: Implantable pressure sensors for health and surgical care”. In: *Medical devices & sensors* 3.3 (Mar. 2020). DOI: `https://doi.org/10.1002/mds3.10068`.

[15] E. Grace. Online. ”Effects of Aerobic Exercise on Intracranial Pressure in Humans”. Califronia USA: Uni. Califronia San Diego, 2019. [Online].Available: `https://escholarship.org/uc/item/30j897h8`. (Accessed: 2023-04-17).

[16] A. P. Zakrzewska et al. “Intracranial pulse pressure waveform analysis using the higher harmonics centroid.” In: *Acta neurochirurgica.* 163.12 (Aug. 2021), pp. 3249–3258. DOI: `https://doi.org/10.1007/s00701-021-04958-1`.

[17] M. Harary, R. G. F. Dolmans, and W. B. Gormley. “Intracranial Pressure Monitoring—Review and Avenues for Development”. In: *Sensors* 18.2 (Feb. 2018). ISSN: 465. DOI: `https://doi.org/10.3390/s18020465`.

[18] M. Czosnyka, Z. Czosnyka, and P. Smielewski. “Pressure reactivity index: journey through the past 20 years”. In: *Acta Neurochirurgica* 159.10 (Aug. 2017), pages2063–2065. ISSN: 1941-0107. DOI: `http://doi.org/10.1007/s00701-017-3310-1`. [Online].Available: `https://cppopt.org/prx/`.

[19] A. Vyas. *On-Chip electrochemical capacitors and piezoelectric energy harvesters for self-powering sensor nodes.* Ed. by A. Vyas. Gothenburg, Sweden: Chalmers University of Technolgy., 2022, pp. 1–18. ISBN: 978-91-7905-646-9. [Online].Available: `https://research.chalmers.se/publication/529273/file/529273_Fulltext.pdf`. (Accessed:2020-12-1).

[20] NI. ”Sensor Terminology”. *www.ni.com.* 2023. [Online].Available: `https://www.ni.com/sv-se/shop/data-acquisition/sensor-fundamentals/sensor-terminology.html`. (Accessed:2023-03-22).

[21] RV magnets. Website. ”Active vs Passive sensing: Is one better than the other?” *Defining active and passive sensors*, Nov. 2021. [Online].Available: `https://www.rvmagnetics.com/active-vs-passive-sensing-is-one-better-than-the-other-116`. (Accessed: 2023-04-19).

[22] C. Svensson, S. Andersson, and P. Bogner. “On the power consumption of analog to digital converters”. In: *IEEE, 2006 NORCHIP.* Linköping, Sweden, 2006, pp. 49–52. DOI: `https://doi.org/10.1109/NORCHP.2006.329242`. [Online].Available: `https://ieeexplore.ieee.org/document/4126945`.

[23] A. E. Kateeb, A. Ramesh, and L. Azzawi. “Wireless Sensor Nodes Processor Architecture and Design.” In: *Proceedings - International Conference on Advanced Information Networking and Applications.* Electrical and Computer Engineering Department University of Michigan –Dearborn USA., 2008, pp. 892–897. DOI: `https://doi.org/10.1109/WAINA.2008.177`. [Online].Available: `https://www.researchgate.net/publication/221192469_Wireless_Sensor_Nodes_Processor_Architecture_and_Design`.

[24] WufanChen and XinYan. “Progress in achieving high-performance piezoresistive and capacitive flexible pressure sensors: A review”. In: *Journal*

of Materials Science & Technology, 43 (Apr. 2020), pp. 175–188. ISSN: 1005-0302. DOI: `https://doi.org/10.1016/j.jmst.2019.11.010`.

[25] H. Lei et al. “Advances in self-powered triboelectric pressure sensors”. In: *Journal of Materials Chemistry.* 36.9 (June 2021), pp. 20100–20130. DOI: `https://doi.org/10.1039/D1TA03505C`.

[26] R. Puers. “Capacitive sensors: When and how to use them”. In: *Sensors and Actuators A: Physical* 37-38 (1993). Proceedings of Eurosensors VI, pp. 93–105. ISSN: 0924-4247. DOI: `https://doi.org/10.1016/0924-4247(93)80019-D`. [Online].Available: `https://www.sciencedirect.com/science/article/pii/092442479380019D`.

[27] N. J. Cleven et al. “A Novel Fully Implantable Wireless Sensor System for Monitoring Hypertension Patients.” In: *IEEE Transactions on Biomedical Engineering.* 59.11 (Nov. 2012), pp. 3124–3130. DOI: `https://doi.org/10.1109/TBME.2012.2216262`.

[28] Z. Liu et al. “Transcatheter Self-Powered Ultrasensitive Endocardial Pressure Sensor.” In: *Advanced Functional Materials* 29.3 (Jan. 2019). DOI: `https://doi.org/10.1002/adfm.201807560`.

[29] C. E. Dahlberg. Master thesis. ”Powering intracranial pressure sensor implants by harvesting energy from the human brain”. *Chalmers University of technology.* [Online].Available: `overleaf.com`. (Accessed: August 9, 2023).

[30] Y. Zang et al. “Advances of flexible pressure sensors toward artificial intelligence and health care applications”. In: *Materials Horizons* 2015.2 (Oct. 2015). DOI: `https://doi.org/10.1039/C4MH00147H`.

[31] Avnet Abacus. Pressure sensor: The designed engineer’s guide. ”Avnet Abacus: ” *Absolute vs gauge vs differential pressure sensors.* [Online].Available: `https://www.avnet.com/wps/portal/abacus/solutions/technologies/sensors/pressure-sensors/measurement-types/`. (Accessed: 2023-04-11).

[32] R. Tang et al. “Flexible pressure sensors with microstructures”. In: *Nano Select* 2.10 (Mar. 2021), pp. 1874–1901. ISSN: 1874-1901. DOI: `https://doi.org/10.1002/nano.202100003`.

[33] G. Schwartz et al. “Flexible polymer transistors with high pressure sensitivity for application in electronic skin and health monitoring”. In: *NATURE COMMUNICATIONS* 4.1859 (May 2013). DOI: `https://doi.org/10.1038/ncomms2832`.

[34] U. P. Claver and G. Zhao. “Recent Progress in Flexible Pressure Sensors Based Electronic Skin”. In: *Advanced Engineering Material* 23.5 (Feb. 2021). DOI: `https://doi.org/10.1002/adem.202001187`.

[35] S. O. M. I. Products. ”Pressure Sensor Accuracy Specifications”. *Sensors ONE.* 2023. [Online].Available: `https://www.sensorsone.com/pressure-sensor-you%20accuracy-specifications/`. (Accessed:2023-04-28).

[36] J. Yang et al. “Highly stretchable pressure sensors with wrinkled fibrous geometry for selective pressure sensing with minimal lateral strain-induced interference.” In: *Composites Part B: Engineering* 217.2021 (Apr. 2021), p. 108899. ISSN: 1359-8368. DOI: `https://doi.org/10.1016/j.compositesb.2021.108899`.

[37] X. Wang et al. “All-silicon dual-cavity fiber-optic pressure sensor with ultralow pressure-temperature cross-sensitivity and wide working temperature range”. In: *Photonics Research* 9.4 (Nov. 2021), pp. 521–529. ISSN: 1359-8368. DOI: `https://doi.org/10.1364/PRJ.414121`.

[38] M. T. Todaro et al. “Biocompatible, Flexible, and Compliant Energy Harvesters Based on Piezoelectric Thin Films”. In: *IEEE Transactions on Nanotechnology* 17.2 (2018), pp. 220–230. DOI: `https://doi.org/10.1109/TNANO.2017.2789300`.

[39] N. Sezer and M. Koç. “A comprehensive review on the state-of-the-art of piezoelectric energy harvesting”. In: *Nano Energy* 80.105567 (2021). ISSN: 2211-2855. DOI: `https://doi.org/10.1016/j.nanoen.2020.105567`.

[40] CCPS Glossary. Website. ”CCPS Process Safety Glossary”. *Center for chemical process safety.* [Online].Available: `https://www.aiche.org/ccps/resources/glossary`. (Accessed: 2023-04-11).

[41] S. Gong et al. “A wearable and highly sensitive pressure sensor with ultrathin gold nanowires”. In: *Nature Communications volume* 5.3132 (Feb. 2014). DOI: `https://doi.org/10.1038/ncomms4132`.

[42] T. Zhao et al. “Highly Sensitive Flexible Piezoresistive Pressure Sensor Developed Using Biomimetically Textured Porous Materials”. In: *ACS Applied Materials & Interfaces* 11.32 (2019), pp. 29466–29473. DOI: `https://doi.org/10.1021/acsami.9b09265`.

[43] H.-J. Qiu et al. “A calibration-free self-powered sensor for vital sign monitoring and finger tap communication based on wearable triboelectric nanogenerator.” In: *Nano Energy* 58 (Jan. 2019), pp. 536–542. ISSN: 2211-2855. DOI: `https://doi.org/10.1016/j.nanoen.2019.01.069`.

[44] P. sensor finder. ”Pressure Sensor Finder”. *www.pressuresensorfinder.com.* 2021. [Online].Available: `https://www.pressuresensorfinder.com/piezoresistive-pressure-sensors-vs-capacitive-pressure-sensors/`. (Accessed:2023-04-12).

[45] G. Yao et al. “Bioinspired Triboelectric Nanogenerators as Self-Powered Electronic Skin for Robotic Tactile Sensing”. In: *Advanced functional materials.* 3.6 (Nov. 2019). DOI: `https://doi.org/10.1002/adfm.201907312`.

[46] J. Sosa et al. “Design and Optimization of a Low Power Pressure Sensor for Wireless Biomedical Applications”. In: *Hidawi* 2015.352036 (Mar. 2015). DOI: `https://doi.org/10.1155/2015/352036`.

[47] A. M. Almassri et al. “Pressure Sensor: State of the Art, Design, and Application for Robotic Hand”. In: *Hindawi Publishing Corporation Journal of Sensors* 2015 (July 2015), p. 12. DOI: `https://doi.org/10.1155/2015/846487`.

[48] H. Shi et al. “Soft capacitive sensors for measurement of both positive and negative pressures”. In: *IEEE transactions on biomedical circuits and systems* 13.5 (Mar. 2019), p. 1011. DOI: `https://doi.org/10.1109/tbcas.2019.2930651`.

[49] M. Zhang et al. “Flexible Wearable Capacitive Sensors Based on Ionic Gel with Full-Pressure Ranges”. In: *ACS Appl. Mater. Interfaces* 15.12 (Mar. 2023), pp. 15884–15892. DOI: `https://doi.org/10.1021/acsami.3c00916`.

[50] S. Renard et al. “Miniature pressure acquisition microsystem for wireless in vivo measurements”. In: *1st Annual International IEEE-EMBS Special Topic Conference on Microtechnologies in Medicine and Biology. Proceedings (Cat. No.00EX451).* 2000, pp. 175–179. DOI: `https://doi.org/10.1109/MMB.2000.893765`.

[51] K. Uchino. *1 - The development of piezoelectric materials and the new perspective.* Ed. by K. Uchino. In Woodhead Publishing Series in Electronic and Optical Materials. Vol. 1. The Pennsylvania State University, USA.: Advanced Piezoelectric Materials, Woodhead Publishing., 2010, pp. 1–85. [Online].Available: `https://www.sciencedirect.com/science/article/pii/B9781845695347500017`. (Accessed:2023-3-22).

[52] S. R. Platt, S. Farritor, and H. Haider. “On Low-Frequency Electric Power Generation With PZT Ceramics.” In: *IEEE/ASME Transactions on Mechatronics.* 10.2 (Apr. 2005), pp. 240–252. DOI: `https://doi.org/10.1109/TMECH.2005.844704`.

[53] ECSTUFF4U for Electronics Engineer. Website. ”Advantages and disadvantages of piezoelectric transducer”. *ECSTUFF4U*, 2017. [Online].Available: `https://www.ecstuff4u.com/2019/07/advantages-and-disadvantages-of-piezoelectric-transducer.html`. (Accessed: 2023-04-19).

[54] Avnet Abacus. Pressure sensor: The designed engineer’s guide. ”Avnet Abacus: ” *Piezoelectric pressure sensors.* [Online].Available: `https://www.avnet.com/wps/portal/abacus/solutions/technologies/sensors/pressure-sensors/core-technologies/piezoelectric/`. (Accessed: 2023-04-19).

[55] S. Roy et al. “Powering Solutions for Biomedical Sensors and Implants Inside the Human Body: A Comprehensive Review on Energy Harvesting Units, Energy Storage, and Wireless Power Transfer Techniques.” In: *IEEE Transactions on Power Electronics* 37.10 (Oct. 2022), pp. 12237–12263. ISSN: 1941-0107. DOI: `https://doi.org/10.1109/TPEL.2022.3164890`.

[56] G. Citerio et al. “Bench test assessment of the new Raumedic Neurovent-P ICP sensor: a technical report by the BrainIT group.” In: *Acta Neurochir* 146

(Aug. 2004), pp. 1221–1226. DOI: `https://doi.org/10.1007/s00701-004-0351-z`.

[57] S. Platt, S. Farritor, and H. Haider. “On low-frequency electric power generation with PZT ceramics”. In: *IEEE/ASME Transactions on Mechatronics* 10.2 (2005), pp. 240–252. DOI: `https://doi.org/10.1109/TMECH.2005.844704`.

[58] C. Wu et al. “Triboelectric Nanogenerator: A Foundation of the Energy for the New Era.” In: *Advance energy materials.* 9.1 (Nov. 2018). ISSN: 1614-6832. DOI: `https://doi.org/10.1002/aenm.201802906`.

[59] R. Zhang and H. Olin. “Material choices for triboelectric nanogenerators: A critical review.” In: *EcoMat, J. Wiley & Sons* 2.4 (Oct. 2020), pp. 1–13. DOI: `https://doi.org/10.1002/eom2.12062`.

[60] H. Zou et al. “Quantifying the triboelectric series.” In: *Nature Communications.* 10.1427 (Mar. 2019). DOI: `https://doi.org/10.1038/s41467-019-09461-x`.

[61] Y. Wang et al. “Efficient Triboelectric Nanogenerator (TENG) Output Management for Improving Charge Density and Reducing Charge Loss.” In: *ACS, Appl. Electron. Mater.* 2021.3 (Jan. 2021), pp. 532–549. DOI: `https://doi.org/10.1021/acsaelm.0c00890`.

[62] S. Wang et al. “Maximum Surface Charge Density for Triboelectric Nanogenerators Achieved by Ionized-Air Injection:Methodology and Theoretical Understanding.” In: *Advanced materials.* 26.39 (Aug. 2014), pp. 6720–6728. DOI: `https://doi.org/10.1002/adma.201402491`.

[63] Q. Zheng et al. “Robust Multilayered Encapsulation for High-Performance Triboelectric Nanogenerator in Harsh Environment”. In: 8.40 (Sept. 2016), pp. 26697–26703. DOI: `https://doi.org/10.1021/acsami.6b06866`.

[64] K. Venugopal and V. Shanmugasundaram. “Effective Modeling and Numerical Simulation of Triboelectric Nanogenerator for Blood Pressure Measurement Based on Wrist Pulse Signal Using Comsol Multiphysics Software.” In: *ACS Omega.* 7.2022 (July 2022), 26863—26870. DOI: `https://doi.org/10.1021/acsomega.2c03281`.

[65] W. I. for Nanotechnology. ”Youtube”. *Youtube.* 2018. [Online].Available: `https://www.youtube.com/watch?v=UUdBLbyexGc`. (Accessed:2023-03-13).

[66] S. Niu and Z. L. Wang. “Theoretical systems of triboelectric nanogenerators.” In: *Nano Energy.* 14.2015 (Nov. 2014), pp. 161–192. ISSN: 2211-2855. DOI: `http://dx.doi.org/10.1016/j.nanoen.2014.11.034`.

[67] D. W. Kim et al. “Material aspects of triboelectric energy generation and sensors.” In: *NGP Asia Materials* 12.6 (Jan. 2020), pp. 1–17. DOI: `https://doi.org/10.1038/s41427-019-0176-0`.

[68] J. Wang et al. “A stretchable self-powered triboelectric tactile sensor with EGaIn alloy electrode for ultra-low-pressure detection.” In: *Nano Energy* 89.Part A (July 2021). ISSN: 2211-2855. DOI: `https://doi.org/10.1016/j.nanoen.2021.106320`.

[69] L. Yao et al. “Review:Recent Progress in Sensing Technology Based on Triboelectric Nanogenerators in Dynamic Behaviors.” In: *Sensors* 22.13 (June 2022). DOI: `https://doi.org/10.3390/s22134837`.

[70] L. Lin et al. “Triboelectric Active Sensor Array for Self-Powered Static and Dynamic Pressure Detection and Tactile Imaging”. In: *ACS nano* 7.9 (Aug. 2013), pp. 8266–8274. DOI: `https://doi.org/10.1021/nn4037514`.

[71] D. Zhao et al. “Universal equivalent circuit model and verification of current source for triboelectric nanogenerator.” In: *Elsevier: Nano Energy* 89 (Nov. 2021). ISSN: 2211-2855. DOI: `https://doi.org/10.1016/j.nanoen.2021.106335`.

[72] D. Liu et al. “Standardized measurement of dielectric materials’ intrinsic triboelectric charge density through the suppression of air breakdown”. In: *Nature Communications* 13.6019 (Oct. 2022). DOI: `https://doi.org/10.1038/s41467-022-33766-z`.

[73] S. Hasan et al. “Comparative study on the contact-separation mode triboelectric nanogenerator”. In: *Journal of Electrostatics* 116.103685 (Feb. 2022). DOI: `https://doi.org/10.1016/j.elstat.2022.103685`.

[74] R. Hinchet et al. "Understanding and modeling of triboelectric-electret nanogenerator". In: *Nano Energy* 47.2018 (May 2018), pp. 440–446. DOI: `https://doi.org/10.1016/j.nanoen.2018.02.030`.

[75] L. Guo et al. "Advances in triboelectric pressure sensors". In: *Sensors and Actuators A: Physical* 355.2023 (Feb. 2023). DOI: `https://doi.org/10.1016/j.sna.2023.114331`.

[76] J. Hu et al. "A flexible triboelectric pressure sensor with high durability for healthcare monitoring". In: *Nano Scale Advances* 2023 (Feb. 2023). DOI: `https://doi.org/10.1039/D2NA00866A`.

[77] A. Schella, S. Herminghaus, and M. Schröter. "Influence of humidity on tribo-electric charging and segregation in shaken granular media". In: *Soft Matter* 13.2017 (Feb. 2017), pp. 394–401. DOI: `https://doi.org/10.1039/C6SM02041K`.

[78] V. Nguyen and R. Yang. "Effect of humidity and pressure on the triboelectric nanogenerator". In: *Nano Energy* 2.5 (Aug. 2013), pp. 604–608. DOI: `https://doi.org/10.1016/j.nanoen.2013.07.012`.

[79] T. Materia. "Corrosion of Aluminum and Its Alloys: Forms of Corrosion". *Totalmatiera.com.* 2008. [Online].Available: `https://www.totalmateria.com/page.aspx?ID=CheckArticle&site=ktn&NM=187`. (Accessed:2021-05-18).

[80] M. H. center. Online: helping documents. "Linear Regression". *MATLAB HELP CENTER.* [Online].Available: `https://se.mathworks.com/help/matlab/data_analysis/linear-regression.html`. (Accessed: 2021-05-24).

[81] M. H. center. Online: helping documents. "Coefficient of Determination (R-Squared)". *MATLAB HELP CENTER.* [Online].Available: `https://se.mathworks.com/help/stats/coefficient-of-determination-r-squared.html`. (Accessed: 2021-05-24).

[82] A. Attaran et al. "Circuit Model of Fano Resonance on Tetramers, Pentamers, and Broken Symmetry Pentamers". In: *Plasmonics* 9.2014 (Dec. 2014), pp. 1303–1313. DOI: `https://doi.org/10.1007/s11468-014-9743-y`.

[83] E. edge. www.ngineersedge.com. ”Pission’s Ratio Metals Materials Chart”. *ENGINEERS EDGE*. [Online].Available: `https://www.engineersedge.com/materials/poissons_ratio_metals_materials_chart_13160.htm`. (Accessed: 2023-05-15).

[84] I. D. Johnston et al. “Mechanical characterization of bulk Sylgard 184 for microfluidics and microengineering”. In: *Micromechanics and Microengineering* 24.035017 (Feb. 2014). DOI: `https://doi.org/10.1088/0960-1317/24/3/035017`.

[85] MatWeb. ”Overview of materials for Ethylene Vinyl Acetate Copolymer (EVA), Adhesive/Sealant Grade”. *matweb.com*. 2023. [Online].Available: `https://www.matweb.com/search/datasheet_print.aspx?matguid=0eeb0c7bf44349e39580d1d1ff302764`. (Accessed:2021-05-18).

[86] C. Martín-Sánchez et al. “On the Stiffness of Gold at the Nanoscale”. In: *ACS Publication* 15.12 (Oct. 2021), pp. 19128–19137. DOI: `https://doi.org/10.1021/acsnano.1c06947`.

[87] R. B. e Dias et al. “Systematic Study of Ethylene-Vinyl Acetate (EVA) in the Manufacturing of Protector Devices for the Orofacial System.” In: *Biomaterials in Regenerative Medicine*. Ed. by L. A. Dobrzański. Poland: InTech, 2018. DOI: `https://doi.org/10.5772/intechopen.69969`. [Online].Available: `https://www.intechopen.com/chapters/56614`.

[88] MIT. ”Aluminum”. *www.mit.edu*. 2023. [Online].Available: `https://www.mit.edu/~6.777/matprops/aluminum.htm`. (Accessed:2023-04-14).

[89] U. University. uu.edu. ”How much does a gallon of gold weigh?” *UNION UNIVERSITY PHYSICS*. [Online].Available: `https://www.uu.edu/dept/physics/scienceguys/2000Aug.cfm`. (Accessed: 2023-05-15).

[90] MIT. ”Material: PDMS (polydimethylsiloxane)”. *www.mit.edu*. 2023. [Online].Available: `https://www.mit.edu/~6.777/matprops/pdms.htm`. (Accessed:2023-04-14).

[91] H. Zhang and L. Quan. “Theoretical Prediction and Optimization Approach to Triboelectric Nanogenerator”. In: *Electrostatic Discharge - From Electrical breakdown in Micro-gaps to Nano-generators. IntechOpen,* 02 (Sept. 2019). DOI: `https://doi.org/10.5772/intechopen.86992`.

[92] L. Ģērmane et al. "Surface engineering of PDMS for improved triboelectrification". In: *Material Advances* 02.4 (Jan. 2023), pp. 875–880. DOI: `https://doi.org/10.1039/D2MA01015A`.

[93] SilikonFabrik. "SF00 - RTV2 silicone (silicone rubber)". *SILIKONFABRIK.DE.* 2023. [Online].Available: `https://www-silikonfabrik-de.translate.goog/silikone/sf-silikon/sf00-rtv2-silikon-silikonkautschuk.html?_x_tr_sl=auto%5C&_x_tr_tl=en%5C&_x_tr_hl=sv`. (Accessed:2023-05-17).

[94] S. S. Basati, T. J. Harris, and A. A. Linninger. "Dynamic Brain Phantom for Intracranial Volume Measurements". In: *IEEE Transactions on Biomedical Engineering* 58.5 (2011), pp. 1450–1455. DOI: `https://doi.org/10.1109/TBME.2010.2050065`.

[95] C. C. Wembers et al. "A mechatronic test-bench to investigate the impact of ventricular pulsation in hydrocephalus." In: *Biomedical Signal Processing and Control.* 75.103579 (May 2022). ISSN: 1746-8094. DOI: `https://doi.org/10.1016/j.bspc.2022.103579`.

[96] S. Bottan, D. Poulikakos, and V. Kurtcuoglu. "Phantom Model of Physiologic Intracranial Pressure and Cerebrospinal Fluid Dynamics". In: *IEEE Transactions on Biomedical Engineering* 59.6 (2012), pp. 1532–1538. DOI: `https://doi.org/10.1109/TBME.2012.2187448`.

[97] E. B. Wu. "The ethics of implantable devices". In: *Journal of Medical Ethics* 33.9 (Jan. 2007), pp. 532–533. DOI: `https://doi.org/10.1136/jme.2006.019000.`.

[98] S. O. Hansson. "The ethics of explantation". In: *BMC Medical Ethics* 22.121 (Aug. 2021), pp. 532–533. DOI: `https://doi.org/10.1186/s12910-021-00690-8`.

[99] G. Zhu et al. "Self-Powered, Ultrasensitive, Flexible Tactile Sensors Based on Contact Electrification". In: *Nano Letters* 14.6 (May 2014), 3208—3213. ISSN: 2211-2855. DOI: `https://doi.org/10.1021/nl5005652`.

[100] R. Ariati et al. "Polydimethylsiloxane Composites Characterization and Its Applications: A Review". In: *Polymers* 13.23 (Dec. 2021). ISSN: 4258. DOI: `https://doi.org/10.3390/polym13234258`.

[101] Z. Fang et al. “Mechanical properties of gold nanowires prepared by nanoskiving approach”. In: *Nano scale* 15.2020 (Mar. 2020), pp. 8194–8199. DOI: `https://doi.org/10.1039/D0NR01049A`.

[102] Fluigent. Online: helping documents. ”Fluigent Smart microfluids”. *Fluigent accessory.* [Online].Available: `https://store.fluigent.com/product-category/accessories/`. (Accessed: 2021-05-24).

[103] A. A. Mathew and S. Vivekanandan. “Design and Simulation of Single-Electrode Mode Triboelectric Nanogenerator-Based Pulse Sensor for Healthcare Applications Using COMSOL Multiphysics”. In: *Energy technology* 10.5 (Feb. 2022). DOI: `https://doi.org/10.1002/ente.202101130`.

[104] Y. Jiang et al. “Stretchable, Washable, and Ultrathin Triboelectric Nanogenerators as Skin-Like Highly Sensitive Self-Powered Haptic Sensors”. In: *Advanced Functional Materials* 31 (Jan. 2021). DOI: `https://doi.org/10.1002/adfm.202005584`.

[105] Z. Zhao et al. “Smart Eutectic Gallium–Indium: From Properties to Applications.” In: *Advanced Material* 35.1 (Aug. 2022). DOI: `https://doi.org/10.1002/adma.202203391`.

A

Appendix A

1

Calculations

The calculations below derive the relationship between pressure P and generated output voltage V in a triboelectric pressure sensor.

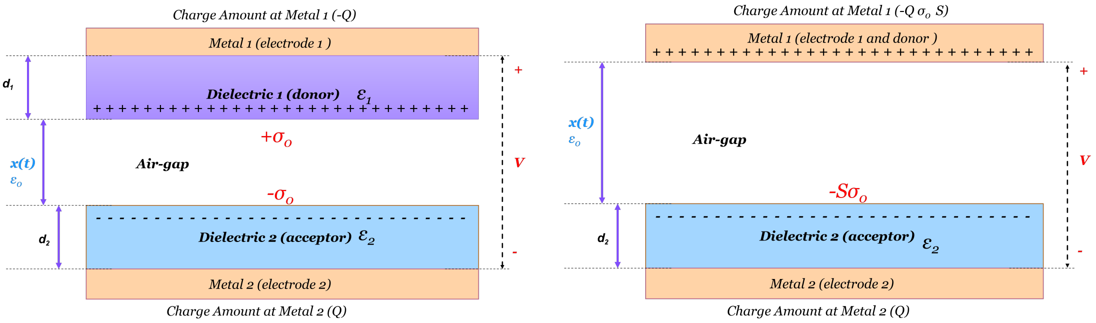

(a) *Dielectric-to-dielectric construction.* (b) *Conductor-to-dielectric construction.*

Figure 1.1: *Two different mode of CS-TENG.*

According to the fundamental illustration in Figure1.1 the electric field strength in the air-gap E_{air} based on *Gauss theorem* can be expressed as equation (1).

$$E_{air} = \frac{\sigma_0 - \frac{Q}{S}}{\varepsilon_0} \tag{1}$$

And for the respective two dielectric layers can be expressed as equations (2) and (3).

$$E_1 = \frac{-Q}{\varepsilon_0 \varepsilon_1 S} \tag{2}$$

$$E_2 = \frac{-Q}{\varepsilon_0 \varepsilon_2 S} \tag{3}$$

Where σ_0 is triboelectric charge density, ε_0 represents permittivity in a vacuum, and Q is the amount of the transferred charges, meanwhile S represents the area size. ε_1 and ε_2 represent the dielectric constant of the respective dielectric layer.

The voltage between the electrodes is defined in equation (4), where $x(t)$ is the distance of air-gap between the two layers. d_1 and d_2 represent the thickness of each dielectric layer.

$$V = E_{air} \cdot x(t) + E_1 \cdot d_1 + E_2 \cdot d_2 \tag{4}$$

To establish the relationship between voltage V, transferred charges Q, and air-gap distance $x(t)$, we analyse the so-called $V - Q - x(t)$ relationship. This involves making substitutions and simplifications as follows. By substituting equations (1) and (2) into equation (4), we derive the $V - Q - x(t)$ relationship, which can be expressed as equation (5).

$$V = -\frac{Q}{\varepsilon_0 \cdot S}\left(\frac{d_1}{\varepsilon_1} + \frac{d_2}{\varepsilon_2} + x(t)\right) + \frac{\sigma_0 x(t)}{\varepsilon_0} \tag{5}$$

The calculation for *conductor-to-dielectric* mode is similar but slightly simpler.Hence terms $E_1 \cdot d_1$ and $\frac{d_1}{\varepsilon_1}$ will be eliminated from equations (4) and (5) respectively. To simplify equations further, the dielectric constant d_{die} can be calculated as a summation according to equation (6) and injected into equation (5).

$$d_{die} = \frac{d_1}{\varepsilon_1} + \frac{d_2}{\varepsilon_2} \tag{6}$$

With the help substitutions and simplifications presented above, the important relationship of $V - Q - x(t)$ could be determined according to equation (7).

$$V = -\frac{Q}{\varepsilon_0 \cdot S}\left(d_{die} + x(t)\right) + \frac{\sigma_0 x(t)}{\varepsilon_0} \tag{7}$$

At the open-circuit condition, no charges are transferred which is why $Q = 0\,\mathrm{C}$ in equation (5) which entails the open circuit voltage as presented in equation (8).

$$V_{OC} = \frac{\sigma_0 x(t)}{\varepsilon_0} \tag{8}$$

At the short-circuit condition, the voltage $V = 0\,\mathrm{V}$ which is why the transferred charges can be calculated by equation (9), (see calculation steps below for deriving equation (9)).

$$0 = -\frac{Q_{SC}}{\varepsilon_0 \cdot S}\left(d_{die} + x(t)\right) + \frac{\sigma_0 x(t)}{\varepsilon_0}$$

$$\Rightarrow \frac{Q_{SC}}{\varepsilon_0 \cdot S}\left(d_{die} + x(t)\right) = \frac{\sigma_0 x(t)}{\varepsilon_0}$$

$$\Rightarrow Q_{SC} = \frac{\sigma_0 x(t)}{\varepsilon_0} \cdot \frac{\varepsilon_0 \cdot S}{\left(d_{die} + x(t)\right)}$$

$$Q_{SC} = \frac{\sigma_0 S x(t)}{d_{die} + x(t)} \tag{9}$$

To calculate the current at the short circuit condition of the TENG, it's convenient to take the derivative of transferred charges with respect to time, (see equation (10)). Where $v(t)$ is the derivative of length $x(t)$ with respect to time t which represent the speed of contraction and expansion of the layers ($x'(t) = v(t)$). Derivation steps of equation (10) are described below. Using the division rule of derivation.

$$\left(\frac{f(x)}{g(x)}\right)' = \frac{f'(x)g(x) - f(x)g'(x)}{g(x)^2}$$

$$\Rightarrow I_{SC} = \frac{\partial Q}{\partial t} = \frac{\partial}{\partial t}\left[\frac{\sigma_0 S x(t)}{d_{die} + x(t)}\right] = \sigma_0 S \cdot \left[\frac{\frac{\mathrm{d}}{\mathrm{d}t}[x(t)]\,(x(t) + d_{die}) - x(t)\,\frac{\mathrm{d}}{\mathrm{d}t}[(x(t) + d_{die})]}{((x(t) + d_{die})^2}\right]$$

$$= \sigma_0 S \cdot \left[\frac{x'(t)(x(t) + d_{die}) - x(t)(x'(t) + 0)}{((x(t) + d_{die})^2}\right] = \sigma_0 S \cdot \left[\frac{x'(t)(x(t) + d_{die}) - x(t)x'(t)}{((x(t) + d_{die})^2}\right]$$

$$I_{SC} = \sigma_0 S \cdot \left[\frac{x'(t)x(t) + x'(t)d_{die} - x(t)x'(t)}{((x(t) + d_{die})^2}\right] = \frac{\sigma_0 S\, x'(t)\, d_{die}}{((x(t) + d_{die})^2}$$

$$I_{SC} = \frac{\sigma_0 \cdot S \cdot d_{die} \cdot v(t)}{\left(d_{die} + x(t)\right)^2} \tag{10}$$

The mechanical pressure from outside entails the open circuit voltage in the TENG, and that is why the relationship between pressure P and open circuit voltage V_{OC} can depend on the distance between the two layers based on equation (11).

$$V_{(p)} = \frac{\sigma_0 x(t_p)}{\varepsilon_0} \tag{11}$$

Variation in the distanced $x(t_p)$ under the pressure P is obtained with equation (12).

$$x(t_p) = x_0 - \Delta x \tag{12}$$

Furthermore, Young's modulus Y of the gap layer can be expressed as the equation (13).

$$Y = \frac{P}{\frac{\Delta x}{x_0}} \tag{13}$$

In order to achieve the relationship between the pressure P in equation (13) and open circuit voltage in equation (11). We substitute equation (13) into equation (12) as follows.

$$x(t_p) = x_0 - \frac{x_0}{Y} \cdot P \tag{14}$$

The substitution of equation (14) into equation (11) can provide us with the relationship between the mechanical pressure P and open circuit voltage in the pressure sensor, derived in equation (15). Where σ_0 represents triboelectric charge density; ε_0 represents permittivity in a vacuum; x_0 represents the initial distance between the layers (size of spacer between the two layers).

$$V_{(p)} = \frac{\sigma_0}{\varepsilon_0}\left(x_0 - \frac{x_0}{Y}P\right) \tag{15}$$

B

Appendix B

1

Gold Layer's Stress Analysis

Figure 1.3 shows the behaviour and the stress level of the Gold electrode as the pressure magnitude increases from intracranial pressure.

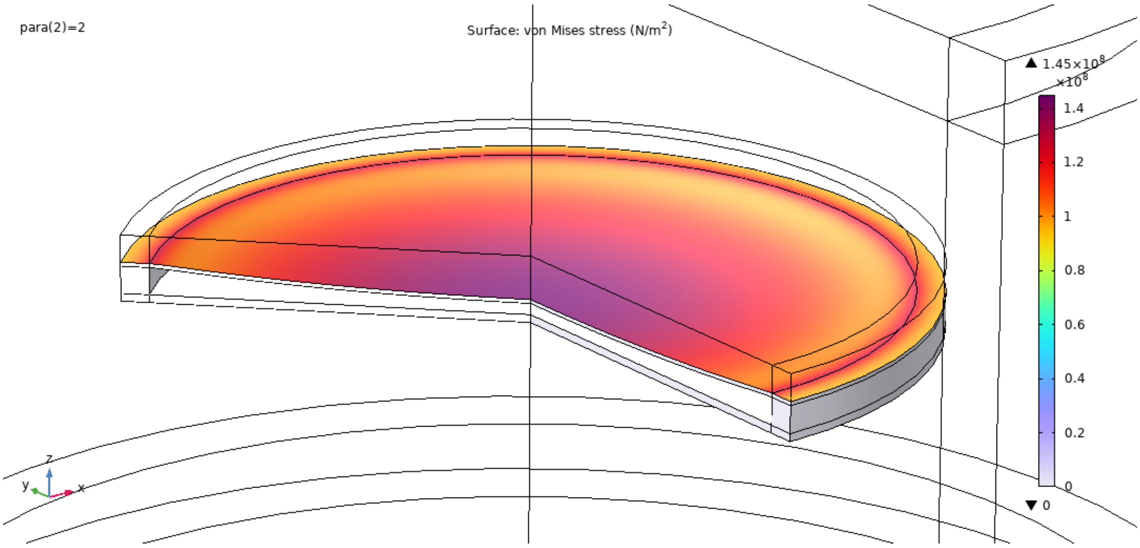

(a) $P = 2\,\text{mmHg}$

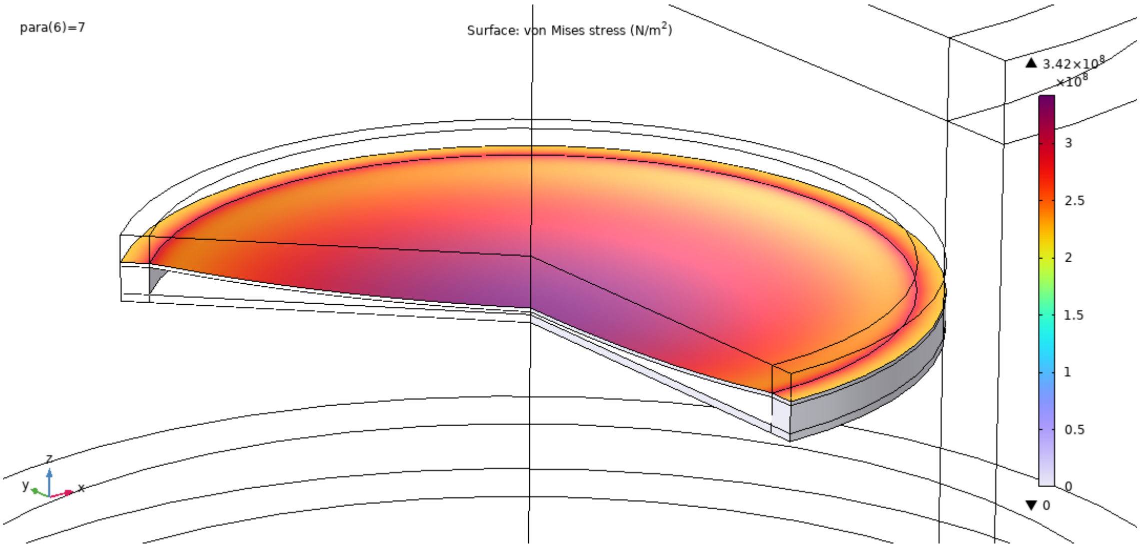

(b) $P = 7\,\text{mmHg}$

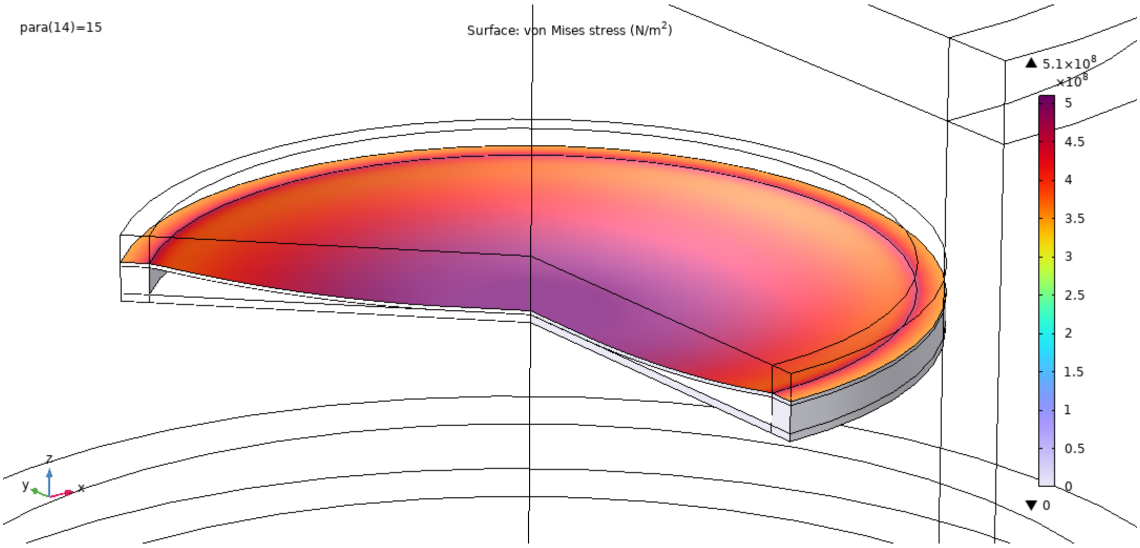

(a) $P = 15\,\mathrm{mmHg}$

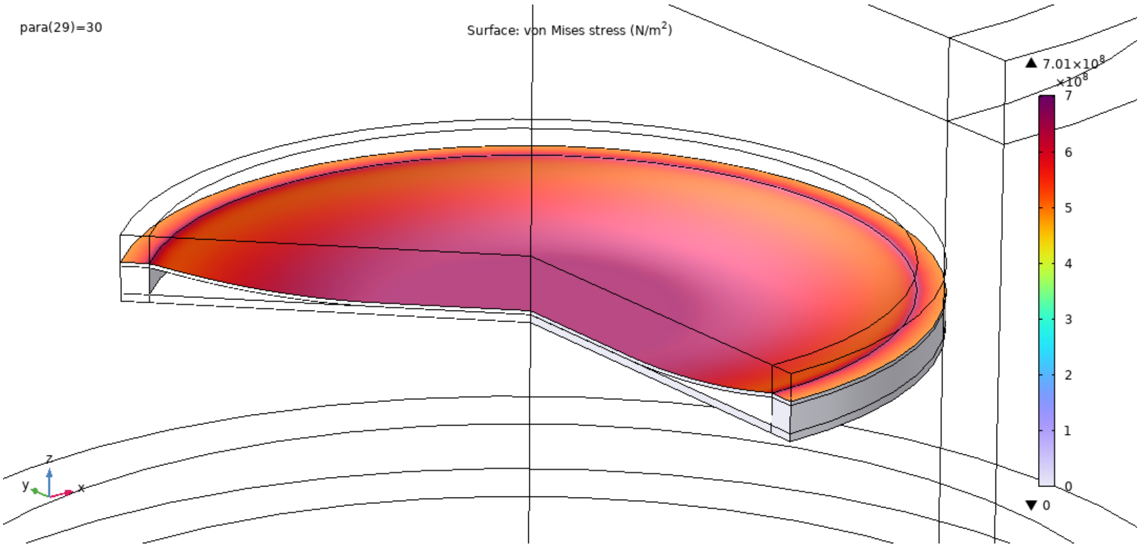

(b) $P = 30\,\mathrm{mmHg}$

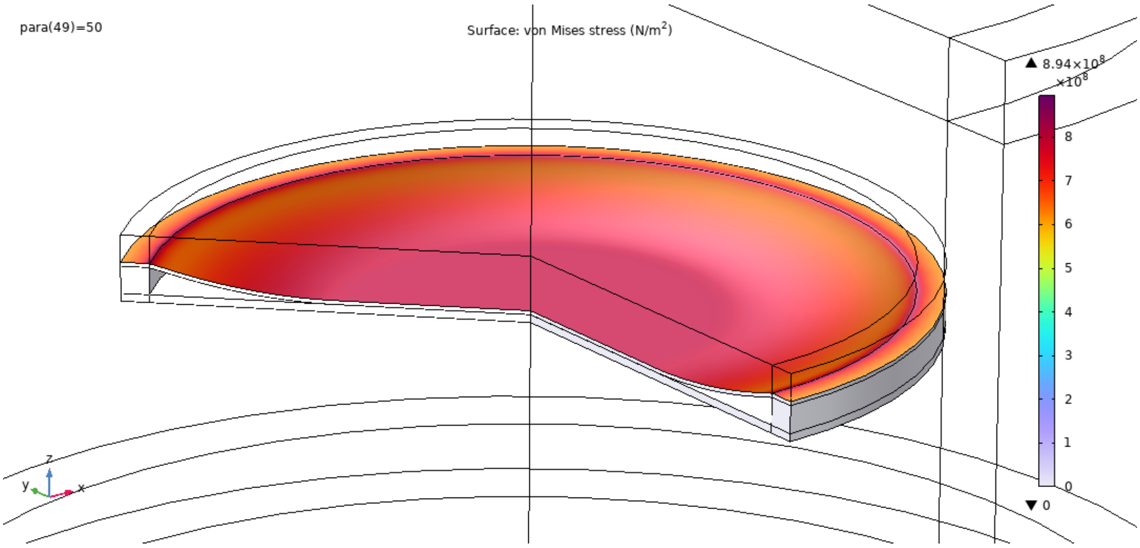

(a) $P = 50\,\text{mmHg}$

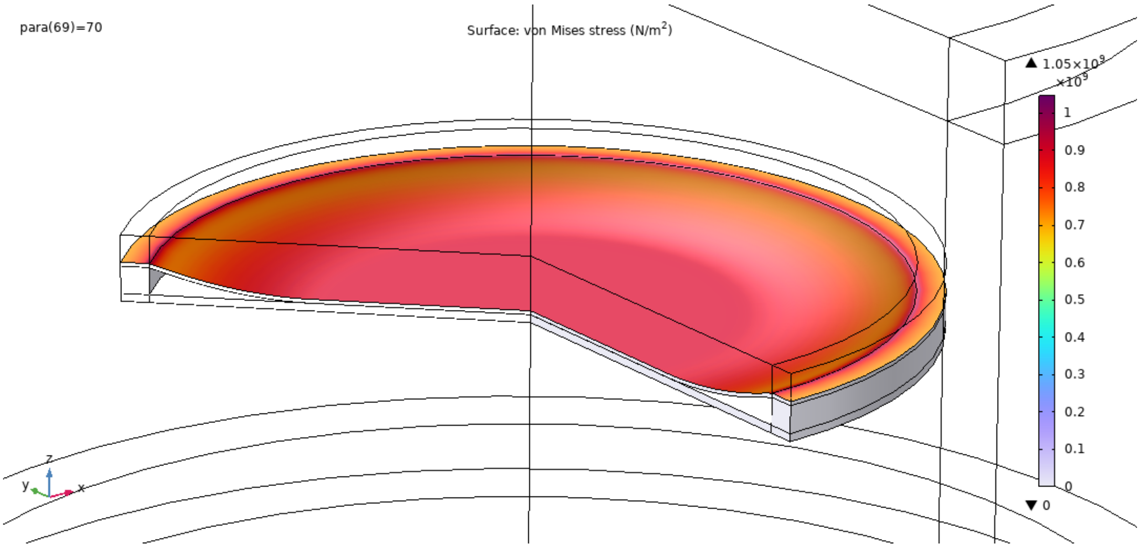

(b) $P = 70\,\text{mmHg}$

Figure 1.3: *The stress levels on the surface of the membrane caused by different applied pressure magnitudes*

2

Calculated R-square Value by MATLAB

This section will provide Figures and R-squared values for the data set collected from `Solid Mechanics` and `Electrostatics` simulations performed by COMSOL software. Also, in this section, the MATLAB script has been provided which defines the step and calculation methods used to obtain the results.

2.1 MATLAB SCRIPT

```
% Model dataset
data_displacement = load("memdisp.txt");
%data_displacement = load("contactarea.txt");
%data_displacement = load("potential.txt");

data = data_displacement;
x = data(1:69,1); y = data(1:69,2);

% Linear regression
coefficients = polyfit(x, y, 1); % Fit a first-degree polynomial (
    linear regression)
y_fit = polyval(coefficients, x); % Generate the fitted values

% Calculate R-squared
y_mean = mean(y);
SSR = sum((y_fit - y_mean).^2); % Regression sum of squares
SST = sum((y - y_mean).^2); % Total sum of squares
R_squared = SSR / SST; % R-squared value

% Display R-squared
disp([’R-squared: ’, num2str(R_squared)]);

% Plot the data and fitted line
plot(x, y, ’o’, ’MarkerSize’, 3, ’LineWidth’, 1);grid on; % Data
    points
hold on;
plot(x, y_fit, ’r-’, ’LineWidth’, 2); % Fitted line
hold off;

% Add labels and title
xlabel(’Pressure (mmHg)’);
ylabel(’Y axis name’);
%title(’Linear Regression’);

% Add legend
lgd=legend(’Data Points’, ’Fitted Line’,’Location’,’southeast’);
title(lgd,sprintf(’R^2 = (%f)’,R_squared),’FontSize’,15)
```

List of Figures:

List of Tables: